

# UC San Diego

## UC San Diego Electronic Theses and Dissertations

### Title

Interface Characterization & Materials Designs for High Performance All-Solid-State Batteries

### Permalink

<https://escholarship.org/uc/item/4xb9q296>

### Author

Tan, Darren Huan Shen

### Publication Date

2021

Peer reviewed|Thesis/dissertation

UNIVERSITY OF CALIFORNIA SAN DIEGO

Interface Characterization & Materials Designs for High Performance All-Solid-State Batteries

A dissertation submitted in partial satisfaction of the  
requirements for the degree Doctor of Philosophy

in

Chemical Engineering

by

Darren Huan Shen Tan

Committee in charge:

Professor Ping Liu, Chair  
Professor Zheng Chen  
Professor Andrew Kummel  
Professor Ying Shirley Meng  
Professor Michael Sailor

2021

Copyright

Darren Huan Shen Tan, 2021

All rights reserved.

The dissertation of Darren Huan Shen Tan is approved, and it is acceptable in quality and form for publication on microfilm and electronically.

University of California San Diego

2021

## **DEDICATION**

To my family, for their unwavering support and encouragement.

## TABLE OF CONTENTS

Dissertation Approval Page.....	iii
Dedication.....	iv
Table of Contents.....	v
List of Abbreviations .....	viii
List of Figures .....	xi
List of Tables .....	xvi
Acknowledgements.....	xvii
Vita .....	xx
Abstract of the Dissertation .....	xxii
Chapter 1. Introduction.....	1
1.1 Energy Storage – Its Role in the 21 <sup>st</sup> Century .....	1
1.2 All Solid-State Batteries .....	3
1.2.1 Solid State Electrolyte Chemistry .....	4
1.2.2 Cathode Interfacial Reactions .....	6
1.2.3 Anode Interfacial Reactions. ....	7
1.2.4 SSE Electrochemical Decomposition .....	10
1.3 Characterization Challenges.....	12
1.3.1 Characterizing Bulk ASSBs.....	13
1.3.2. Characterizing Meso to Nano-scale Interfaces .....	14
1.3.3. Spectroscopy Techniques .....	16
1.4 Scalable Design – Organic/Inorganic Composites.....	17
1.4.1. Role of Polymers in Scalable Fabrication .....	17
1.4.2. Resistive Effects of Polymers.....	19
1.5 Battery Recycling & Sustainability.....	20
1.5.1. Battery Recycling Challenges.....	20

1.5.2. Fully Recyclable ASSB Model .....	22
1.5.3. Direct Regeneration of SSEs and Cathodes.....	23
1.6 Conclusions .....	25
Chapter 2. Elucidating Reversible Redox of Sulfide $\text{Li}_6\text{PS}_5\text{Cl}$ .....	27
2.1 Introduction .....	27
2.2 Methods .....	30
2.2.1 Materials Preparation of SSE-Carbon & Counter Electrodes.....	30
2.2.2 Materials Characterization of Pristine and Cycles SSE-Carbon.....	30
2.2.3 Electrochemical Evaluation of SSE & Half Cells .....	31
2.3 Results and Discussion .....	32
2.3.1 Electrochemical Redox of $\text{Li}_6\text{PS}_5\text{Cl}$ .....	32
2.3.2 XPS of $\text{Li}_6\text{PS}_5\text{Cl}$ at various potentials .....	34
2.3.3 XRD & Raman of $\text{Li}_6\text{PS}_5\text{Cl}$ at various potentials .....	36
2.3.4 Solid-state nuclear magnetic resonance (NMR) at mid-discharged state.....	38
2.3.5 EIS of $\text{Li}_6\text{PS}_5\text{Cl}$ half-cell at various potentials .....	39
2.4 Conclusion.....	45
Chapter 3. Scalable Solution Processing for ASSBs Manufacturing.....	46
3.1 Introduction.....	46
3.2 Methods.....	48
3.2.1 Glass Ceramic Synthesis .....	48
3.2.2 Experimental Characterization & Electrochemical Testing.....	49
3.3 Results and Discussion .....	51
3.2.1 $\text{Li}_7\text{P}_3\text{S}_{11}$ –Solvent Compatibility .....	52
3.2.2 Computational DFT Calculations of Molecular Interactions .....	56
3.2.3 $\text{Li}_7\text{P}_3\text{S}_{11}$ –Polymer Compatibility.....	58
3.2.4 Electrochemical Evaluation of $\text{Li}_7\text{P}_3\text{S}_{11}$ – Polymer Composite .....	59
3.2.5 Air / Moisture Stability Test .....	61
3.4 Conclusion.....	62
Chapter 4. Enabling Carbon Free Silicon Anodes for Robust ASSBs.....	64
4.1 Introduction.....	64
4.2 Methods .....	68
4.2.1 Materials Preparation .....	68
4.2.2 Materials Characterization.....	69
4.2.3 Electrochemical Characterization .....	70
4.3 Results and Discussion .....	71

4.3.1 Interface Characterization .....	71
4.3.2 Quantification of SEI Components .....	73
4.3.3 Morphological Evolution .....	77
4.3.4 Electrochemical Performance.....	81
4.4 Conclusion .....	85
Chapter 5. Sustainable design of fully recyclable all solid-state batteries .....	87
5.1 Introduction.....	87
5.2 Methods .....	89
5.2.1 Materials Preparation .....	89
5.2.2 Materials & Electrochemical Characterization .....	89
5.2.3 Recycling Methods & Everbatt Model.....	90
5.2 Results and Discussion .....	91
5.2.1 All Solid-State Battery Recycling Model .....	91
5.2.2 Economical & Environmental Impact Analysis.....	94
5.2.3 Experimental Validation of ASSB Recycling.....	99
5.2.4 Electrochemical Performance.....	102
5.3 Conclusion.....	104
Chapter 6. Perspectives & Summary .....	105
6.1 Bringing Discoveries into the Market.....	106
References .....	110



## LIST OF ABBREVIATIONS

AAO: Anodized Aluminum oxide  
ACN: Acetonitrile  
ASSB: All-Solid-State Battery  
a.u.: Arbitrary Units  
C: Carbon  
CB: Carbon Black  
CE: Coulombic Efficiency  
CEI: Cathode-Electrolyte Interphase  
CO<sub>2</sub>: Carbon Dioxide  
CMC: Carboxymethyl Cellulose  
CT: Computed Tomography  
CV: Cyclic Voltammetry  
CVD: Chemical Vapor Deposition  
DFT: Density Functional Theory  
DMC: Dimethyl Carbonate  
EDS: Energy Dispersive Spectroscopy  
EELS: Electron Energy Loss Spectroscopy  
EIS: Electrochemical Impedance Spectroscopy  
EOL: End Of Life  
EV: Electric Vehicle  
FIB: Focused Ion Beam  
GHG: Greenhouse Gas Emissions  
ICP-MS: Inductively Coupled Plasma Mass Spectrometry  
LATP:  $\text{Li}_{1+x}\text{Al}_x\text{Ti}_{2-x}(\text{PO}_4)_3$   
LCO: Lithium Cobalt Oxide  
LFP:  $\text{LiFePO}_4$   
LGPS:  $\text{Li}_{10}\text{GeP}_2\text{S}_{12}$   
LIB: Lithium Ion Battery  
Li-In: Lithium-Indium Alloy

LiPON: Lithium Phosphorous Oxynitride

LLZO:  $\text{Li}_7\text{La}_3\text{Zr}_2\text{O}_{12}$

LNO: Lithium Niobate

LPS:  $\text{Li}_3\text{PS}_4$

LPSCI:  $\text{Li}_6\text{PS}_5\text{Cl}$

LTO: Lithium Titanate

MAS: Magic Angle Spinning

MEK: Methyl Ethyl Ketone

GPa: Gigapascal

MPa: Megapascal

NASICON: Na Superionic Conductor

NBR: Poly(acrylonitrile-co-butadiene)

NCA:  $\text{Li}(\text{Ni}_x\text{Co}_y\text{Al}_z)\text{O}_2$

NCM811:  $\text{LiNi}_{0.8}\text{Co}_{0.1}\text{Mn}_{0.1}\text{O}_2$

NMC532:  $\text{LiNi}_{0.5}\text{Mn}_{0.3}\text{Co}_{0.2}\text{O}_2$

NDP: Neutron Depth Profiling

NMP: N-methyl-2-pyrrolidone

NMR: Nuclear Magnetic Resonance

OCV: Open Circuit Voltage

PEEK: Polyether Ether Ketone

PEO: Polyethylene Oxide

PLD: Pulsed Laser Deposition

PTFE: Polytetrafluoroethylene

PVD: Physical Vapor Deposition

PVDF: Polyvinylidene Fluoride

PVDF-HFP: Polyvinylidene Fluoride-co-hexafluoropropylene

PVP: Polyvinylpyrrolidone

S: Sulfur

SBS: Polystyrene-block-polybutadiene

SEBS: Styrene-ethylene-butylene-styrene

SEM: Scanning Electron Microscopy

SSE: Solid-State Electrolyte

SEI: Solid-Electrolyte Interphase

SEM: Scanning Electron Microscopy

Si: Silicon

SIL: Solvate Ionic Liquid

STEM: Scanning Transmission Electron Microscopy

TEM: Transmission Electron Microscopy

TGC: Titration Gas Chromatography

THF: Tetrahydrofuran

TOL: Toluene

VGCF: Vapor-grown carbon fiber

XAS: X-ray Absorption Spectroscopy

XPS: X-ray Photoelectron Spectroscopy

XRD: X-ray Diffraction

XYL: Xylene

## LIST OF FIGURES

Figure 1.1	a) Projected global annual passenger vehicle sales, showing increasing fraction of EVs. b) Projected annual distribution of electricity generation, showing increasing proportion of energy generation from renewables that would translate into need for storage. ....1	1
Figure 1.2	(a) Global distribution of reserves and (b) evaluation of supply risk of critical materials for LIBs based on current trends in LIB growth. ....2	2
Figure 1.3	Summary of major scientific and engineering challenges for all solid-state battery development. ....4	4
Figure 1.4	Electrochemical stability of various solid electrolytes and their effects on cell performance. a) Illustration of solid electrolytes stability windows vs common electrodes typical operating potential. b) Methods to improve thermodynamic stabilities of solid electrolytes.....5	5
Figure 1.5	Anode Interfacial Types: (a) SSEs that are not stable and do not form stable interfaces, as a result of reaction products that are both ionically and electronically conductive. (b) SSEs that are not stable but form a stable and passivating interface, and (c) reaction products formed are stable with metallic Li. ....8	8
Figure 1.6	Summary of current effective methods to characterize all solid-state batteries. a) Nano-computed Tomography gives elemental contrast within buried solid electrolytes. b) $\text{Li}^7$ Nuclear Magnetic Resonance chemical shift imaging observed lithium deposits within SSEs. <sup>1</sup> (Marbella, Zekoll et al. 2019) <sup>1</sup> ..... 13	13
Figure 1.7	Manufacturing considerations for ASSBs and the role of polymeric binders. a) Schematic of large-scale manufacturing of ASSBs. Polymer & solid electrolyte composites allow for good mechanical processability as well as decreased separator thickness layers to increase cell-level energy density..... 19	19
Figure 1.8	a) Illustration of various recycling methods. b) Schematic of potential closed loop all solid-state battery recycling process.....22	22
Figure 2.1	(a) Reported 1 <sup>st</sup> cycle discharge capacities of representative solid-state Li-S batteries in literature. Dotted lines represent theoretical capacity of $\text{Li}_2\text{S}$ and S respectively. (b) Illustration of electrochemical operating windows for $\text{Li}_6\text{PS}_5\text{Cl}$ , Li-S and Li-ion chemistries.....29	29
Figure 2.2	(a) Cyclic voltammograms for the first two cycles, voltage was swept between 0 - 4.2 V (vs $\text{Li}/\text{Li}^+$ ) at $100 \mu\text{V s}^{-1}$ starting from OCV. (b) 1 <sup>st</sup> and 2 <sup>nd</sup> voltage profiles of $\text{Li-In}   \text{Li}_6\text{PS}_5\text{Cl}   \text{Li}_6\text{PS}_5\text{Cl-C}$ half cell. Cycling was done between 0 to 4.2 V (vs $\text{Li}/\text{Li}^+$ ) at room temperature and a current density of $0.25 \text{ mA cm}^{-2}$ .....33	33
Figure 2.3	XPS spectra showing the binding energies of $\text{Li}_6\text{PS}_5\text{Cl}$ at different cycling potentials. (a) Sulfur 2p region. (b) Phosphorus 2p region. (c) Cycling voltage	

	profile for reference. (d) XRD patterns at different cycling potentials. $\text{Li}_2\text{S}$ can be identified as reduced product.....	35
Figure 2.4	(a) Redox reaction pathway of $\text{Li}_6\text{PS}_5\text{Cl}$ for the 1 <sup>st</sup> charge and subsequent cycles. (b) (Top) $^{31}\text{P}$ MAS NMR spectra of pristine and mid-discharged $\text{Li}_6\text{PS}_5\text{Cl}$ . (Bottom) $^{31}\text{P}$ MAS NMR spectrum of reference $\text{Li}_3\text{PS}_4$ containing both $\gamma$ and $\beta$ phases.....	37
Figure 2.5	Nyquist plots at different cycling potentials showing the impedance changes of Li-In   LPSCI   LPSCI-C cell (left). Normalized capacity vs Voltage profiles are displayed for reference (middle). Bar graph shows relative differences in cell impedance at different oxidation or reduction states of $\text{Li}_6\text{PS}_5\text{Cl}$ -C (right). .....	40
Figure 2.6	EIS measurements of impedance growth before and after: (a) 1 <sup>st</sup> Discharge of anode with 60wt% Graphite. (b) 1 <sup>st</sup> Charge of cathode NCM811 with 1wt% Carbon additive. Showing large impedance growth at cathode despite small amounts of carbon additive. ....	42
Figure 2.7	EIS measurements of pure interfacial products: (a) reduced species of $\text{LiCl}$ , $\text{Li}_3\text{P}$ and $\text{Li}_2\text{S}$ . (b) oxidized species of $\text{LiCl}$ , $\text{P}_2\text{S}_5$ and $\text{S}$ . ....	42
Figure 2.8	SEM images of: (a) carbon black (b) vapor grown carbon fibre showing differences in morphology and size. (c) Charge voltage profiles of Li-In   $\text{Li}_6\text{PS}_5\text{Cl}$   $\text{Li}_6\text{PS}_5\text{Cl}$ -C cells using 30 wt% carbon black (surface area: $\sim 80 \text{ m}^2/\text{g}$ ) vs vapor grown carbon fibre (surface area: $\sim 24 \text{ m}^2/\text{g}$ ) .....	44
Figure 3.1	Different solvent color changes after addition of $\text{Li}_7\text{P}_3\text{S}_{11}$ . ....	53
Figure 3.2	(a) Rietveld refinement of pristine $\text{Li}_7\text{P}_3\text{S}_{11}$ , the refinement model was adapted from literature. (b) XRD patterns of $\text{Li}_7\text{P}_3\text{S}_{11}$ after dispersion in: ACN, DMC, TOL, XYL.....	54
Figure 3.3	(a) Deconvoluted Raman spectra of $\text{Li}_7\text{P}_3\text{S}_{11}$ after dispersion in different solvents. (b) Visualizations of detected lithium thiophosphates present. (c) XPS spectra of 2p regions of sulfur and phosphorus showing the combined binding energies of $\text{Li}_7\text{P}_3\text{S}_{11}$ after dispersion. ....	55
Figure 3.4	$\text{Li}_7\text{P}_3\text{S}_{11}$ – Solvent degradation mechanism vs solvent polarity / dielectric constant: (a) $\text{P}_2\text{S}_7^{4-}$ dissolution energies. (b) $\text{P}_2\text{S}_7^{4-}$ reaction A energies forming $\text{P}_2\text{S}_6^{4-}$ and $\text{S}^{2-}$ . (c) $\text{P}_2\text{S}_7^{4-}$ and $\text{S}^{2-}$ reaction B energies forming $\text{PS}_4^{3-}$ . Calculation details can be found in the methods section.....	57
Figure 3.5	Nyquist plots of $\text{Li}_7\text{P}_3\text{S}_{11}$ EIS measurements after dispersion in different solvents, showing large charge transfer resistances from ACN and DMC dispersions, the high frequency inset shows TOL and XYL dispersions.....	58
Figure 3.6	(a) Cross-section SEM image of composite electrolyte film fabricated with 95 wt.% $\text{Li}_7\text{P}_3\text{S}_{11}$ and 5 wt.% SEBS. (b) Digital photograph of a 20 cm * 6 cm casted electrolyte film and a rolled-up film (inset). (c) Nyquist plot of the composite electrolyte film. ....	60

Figure 3.7	(a) Setup used for H <sub>2</sub> S gas measurements from 100 mg of Li <sub>7</sub> P <sub>3</sub> S <sub>11</sub> hydrolysis in air. (b) H <sub>2</sub> S amount released vs time for fixed volume air exposed to 100 mg bare Li <sub>7</sub> P <sub>3</sub> S <sub>11</sub> , 100 mg composite with hydrophobic SEBS polymer. (c) & (d) Bare Li <sub>7</sub> P <sub>3</sub> S <sub>11</sub> before and after flooding in water .....62
Figure 4.1	Literature summary on Si anodes classified by μSi, nano-Si and sputtered-Si. (a) Plot of Si ratio in anode vs maximum capacity for full cells, inset shows the number of Si publications per year in the past decade, with a vast majority presenting only half-cell studies. (b) Plot of capacity retention. ....65
Figure 4.2	Schematic of 99.9 wt% μSi electrode in an all solid-state full cell. 1) During lithiation, a passivating SEI is formed between the μSi electrode and the SSE, followed by lithiation of μSi particles near the interface. 2) The highly reactive Li-Si then reacts with Si particles within its vicinity .....67
Figure 4.3	Carbon effects on SSE decomposition. (a) Voltage profiles of μSi    SSE    NCM811 cells with and without carbon additives (20 wt.%), inset shows a lower initial plateau indicating SSE decomposition to form SEI. (b) XRD patterns, and (c-e) XPS spectra of the (c) S 2p, (d) Li 1s and (e) Si 2p core regions ..... 72
Figure 4.4	(a) Scanning electron microscopy image of μSi cast used in this work. Inset shows digital image of the 99.9 wt% μSi cast. (b) DC polarization of bulk μSi electrode, showing electronic conductivity of 3 x 10 <sup>-5</sup> S cm <sup>-1</sup> . ....73
Figure 4.5	(a) Voltage profiles of full cells used in titration gas chromatography (TGC) experiments. (b) Quantified Li-Si and SEI amounts relative to cell capacity. (c) Voltage profile of full cell used for EIS, and (d) Nyquist plots for different cycle numbers showing limited impedance growth..... 75
Figure 4.6	μSi – SSE - NCM811 full cells voltage profiles at room temperature and 55°C using (a) liquid electrolyte at room temperature, (b) liquid electrolyte at 55°C, (c) solid electrolyte at room temperature, (d) solid electrolyte at 55°C. ....75
Figure 4.7	μSi - NCM811 full cells voltage profiles at room temperature and 55°C using (a) liquid electrolyte at room temperature, (b) liquid electrolyte at 55°C, (c) solid electrolyte at room temperature, (d) solid electrolyte at 55°C. .... 77
Figure 4.8	Visualizing lithiation and delithiation mechanism of 99.9 wt% Si anodes using focused ion beam (FIB) and energy-dispersive X-ray spectroscopy (EDS) imaging. (a) Pristine porous microstructure of μSi electrode. (b) Charged state with densified interconnected Li-Si structure .....78
Figure 4.9	SEM cross section images of 99.9% μSi electrodes at the pristine and lithiated states using a solid and liquid electrolyte. A lower loading of about 2 mAh cm <sup>-2</sup> is used to image the entire electrode due to the limited milling depth achievable with the FIB tool. .... 78
Figure 4.10	SEM cross section images of μSi anode electrode with ~3.8 mg cm <sup>-2</sup> mass loading. (a) Pristine electrode of 27 μm in thickness, with a porosity of 40%. (b) Charged state showing dense Li-Si layer formation of 55 μm in thickness. (b) Discharged state of 40 μm in thickness.....79

Figure 4.11	$\mu\text{Si}  \text{SSE}  \text{NCM811}$ full cell performance: (a) High current densities at room temperature, (b) Wide operating temperature ranges under $0.3 \text{ mA cm}^{-2}$ , (c) High areal capacities, (d) Extended cycle life at room temperature, demonstrating overall robustness of ASSB using 99.9 wt% $\mu\text{Si}$ anodes.....	83
Figure 4.12	Dry electrode processing for cathode to achieve high loading. Cathode composition: 80 (NCM) : 20 (SSE) : 3(VGCF): 0.5 (PTFE) in weight. (a) Digital images of hot rolling and folding process. Sequence is repeated until target thicknesses are achieved.....	85
Figure 5.1	Schematic of the proposed ASSB recycling procedure at an industrial scale, based on the principles of direct recycling. Cell packaging of the ASSB is first removed before the entire cell stack is processed in a solution without further component separation .....	93
Figure 5.2	Energy and environmental impact analysis from upstream processing to the fully recycled state. (a) Total energy consumption and (b) greenhouse gas emission (GHG) comparisons from direct methods, conventional hydrometallurgy, and pyrometallurgy for $\text{LiCoO}_2$ recycling .....	95
Figure 5.3	$\text{Li}_6\text{PS}_5\text{Cl}$ particles at the (a) pristine state and (b) recycled state. The average particle size of $\text{Li}_6\text{PS}_5\text{Cl}$ decreased after the solution process. Characterizing $\text{Li}_6\text{PS}_5\text{Cl}$ solid electrolyte at the pristine and regenerated state. (c) X-ray diffraction patterns showing the retention of the bulk structure.....	100
Figure 5.4	(a) Schematic of the $\text{LiCoO}_2$ cathode surface treatment and regeneration process. (b) Voltage profile of the $\text{Li}   \text{Li}_6\text{PS}_5\text{Cl}   \text{LiCoO}_2$ cell in the pristine and recycled state, with the schematic of the cell setup in inset. (c) Cycle performance of the $\text{Li}   \text{Li}_6\text{PS}_5\text{Cl}   \text{LiCoO}_2$ cell.....	102
Figure 6.1	Illustration and descriptions of cell and manufacturing protocols used in (a) laboratory scale research typically done using gloveboxes and coin cells, (b) pilot scale testing typically done with multi-layer pouch type cells in dry rooms and (c) industrial scale manufacturing.....	107

## LIST OF TABLES

Table 3.1	Common solvents used in battery materials and its polarities and dielectric constants. ....	53
Table 3.2	Conductivity measurements of $\text{Li}_7\text{P}_3\text{S}_{11}$ after dispersion in different solvents. ....	58
Table 4.1	Expected electrode layer thickness vs relative density at the pristine, charged and discharged states. Thick electrodes were used in the calculations to reduce measurement error. Asterisks* indicate approximate observed thicknesses measured with SEM imaging.....	80
Table 5.1	Materials requirements to recycle 1 kg of spent batteries via different recycling technologies.....	97
Table 5.2	Total emissions and breakdown of greenhouse gases (GHGs) to recycle 1 kg of spent batteries via different recycling technologies. ....	97
Table 5.3	Ionic conductivity of the $\text{Li}_6\text{PS}_5\text{Cl}$ solid electrolyte and ICP results of the $\text{LiCoO}_2$ cathode materials at the pristine, cycled, and regenerated states. Ionic conductivity was measured via electrochemical impedance spectroscopy measurements. ....	102



## ACKNOWLEDGEMENTS

I would like to thank my advisors Professor Ying Shirley Meng and Professor Zheng Chen for all the opportunities and guidance in my research training and professional development, as well as building upon our common goals toward commercializing our discoveries. I would also like to recognize my committee Chair, Professor Ping Liu for his support, committee members Professor Andrew Kummel and Professor Michael Sailor for their valuable feedback.

I am extremely grateful toward my past and present team members in the solid-state team, Dr. Han Nguyen, Dr. Erik A. Wu, Dr. Abhik Banerjee, Dr. Jean-Marie Doux, Grayson Deysher, Yu-Ting Chen, Phillip Ridley, So-yeon Ham, Jerry Yang and Chiho Jo, for the years of enjoyable and highly productive work culture. Their intellectual and passionate contributions were essential toward the discoveries made, and I feel extremely fortunate to have worked with such wonderful colleagues.

I would also like to thank the past and present members in the Chen research group, Dr. Panpan xu, Dr. Yang Shi and Mingqian Lee, for their collaborative efforts and contributions in the work. It was a pleasure to work with everyone on the project.

I would also like to thank my collaborators: Dr. Shyue Ping Ong's Materials VirtualLab (Dr. Iek-Heng Chu, Dr. Maxwell Marple (LLNL), Dr. Ryan Stephens (Shell), Dr. Hoe Jin Hah (LG Chem), Han Hyea Eun (LG Chem) and Hyeri Jeong (LG Chem) for their hard work and invaluable inputs toward the solid-state battery research. Specifically, Dr. Shyue Ping Ong and his team for their computational modelling expertise, Dr. Maxwell Marple for NMR support, Dr. Ryan Stephens for the insightful discussions on all solid-state battery commercialization and Dr. Hoe Jin Hah, Han Hyea Eun and Hyeri Jeong for their regular discussions on all solid-state battery interfacial behavior and performance improvements.

I would like to thank my family and friends for giving me their support during my time at UCSD. My peers, Rory Runser and Yixuan Li for their unwavering advice and encouragement during challenging periods, as well as motivating me to remain healthy physically and mentally.

I would like to thank my other colleagues in Professor Shirley Meng's group: Dr. Thomas Wynn, Dr. Hyeseung Chung, Dr. Han Nguyen for their wise advice and assistance throughout my research in the lab.

I acknowledge the financial support from LG Chem through the Battery Innovation Contest (BIC) program. I would like to also acknowledge the UCSD Crystallography Facility, as well as the San Diego Nanotechnology Infrastructure (SDNI) of UCSD, a member of the National Nanotechnology Coordinated Infrastructure, which is supported by the National Science Foundation (GrantECCS-1542148). Characterization work was performed in part at the UC Irvine Materials Research Institute (IMRI) using instrumentation funded in part by the National Science Foundation Major Research Instrumentation Program under Grant No. CHE-1338173, as well as Lawrence Livermore National Laboratory under Contract DE-AC52-07NA27344, release number LLNL-JRNL-786041.

I acknowledge the assistance from the UCSD Crystallography Department, Dr. Milan Gembicky, Dr. Han Nguyen and Baharak Sayahpour, for their assistance on air-sensitive capillary XRD measurements and their willingness to discuss data and experiments at all times.

The thesis abstract & Chapter 1, in part, is a reprint of the material "From nanoscale interface characterization to sustainable energy storage using all-solid-state batteries" as it appears in Nature Nanotechnology. Tan, D. H. S.; Banerjee, A.; Chen, Z.; Meng, Y. S. 2020, 15 (3), 170-180. The dissertation author was the first author of this paper, all authors contributed to this work.

Chapter 2, in full, is a reprint of the material "Elucidating Reversible Electrochemical Redox of  $\text{Li}_6\text{PS}_5\text{Cl}$  Solid Electrolyte" as it appears in ACS Energy Letters. Tan, D. H. S.; Wu, E. A.; Nguyen, H.; Chen, Z.; Marple, M. A. T.; Doux, J.-M.; Wang, X.; Yang, H.; Banerjee, A.; Meng, Y. S. 2019, 2418-2427. The dissertation author was the first author of this paper, all authors contributed to this work.

Chapter 3, in full, is a reprint of the material “Enabling Thin and Flexible Solid-State Composite Electrolytes by the Scalable Solution Process.” as it appears in ACS Applied Energy Materials. Tan, D. H. S.; Banerjee, A.; Deng, Z.; Wu, E. A.; Nguyen, H.; Doux, J.-M.; Wang, X.; Cheng, J.-h.; Ong, S. P.; Meng, Y. S.; Chen, Z. 2019, 2, 6542–6550. The dissertation author was the first author of this paper, all authors contributed to this work.

Chapter 4, in full, has been submitted for publication as “Carbon Free High Loading Silicon Anodes Enabled by Sulfide Solid Electrolytes for Robust All Solid-State Batteries” as a research article in Science. Tan, D. H. S.; Chen, Y.-T.; Yang, H.; Bao, W.; Sreenarayanan, B.; Doux, J.-M.; Li, W.; Lu, B.; Ham, S.-Y.; Sayahpour, B.; Scharf, J.; Wu, E. A.; Deysheer, G.; Han, H. E.; Hah, H. J.; Jeong, H.; Chen, Z.; Meng, Y. S. The dissertation author was the first author of this paper, all authors contributed to this work.

Chapter 5, in full, is a reprint of the material “Sustainable design of fully recyclable all solid-state batteries” as it appears in MRS Energy & Sustainability. Tan, D. H. S.; Xu, P.; Yang, H.; Kim, M.-c.; Nguyen, H.; Wu, E. A.; Doux, J.-M.; Banerjee, A.; Meng, Y. S.; Chen, Z. The dissertation author was the first author in both papers, all authors contributed to this work.

## VITA

2015	Bachelor of Engineering, Chemical Engineering, National University of Singapore
2018	Master of Science, Chemical Engineering, University of California San Diego
2021	Doctor of Philosophy, Chemical Engineering, University of California San Diego

## PUBLICATIONS

(\* = authors contributed equally to the work)

1. Shi, Y.; Tan, D.; Li, M.; Chen, Z., Nanohybrid electrolytes for high-energy lithium-ion batteries: recent advances and future challenges. *Nanotechnology* **2019**, *30* (30), 302002.
2. Tan, D. H. S.; Banerjee, A.; Deng, Z.; Wu, E. A.; Nguyen, H.; Doux, J.-M.; Wang, X.; Cheng, J.-h.; Ong, S. P.; Meng, Y. S.; Chen, Z., Enabling Thin and Flexible Solid-State Composite Electrolytes by the Scalable Solution Process. *ACS Appl. Energy Mater.* **2019**, *2*, 6542–6550.
3. Tan, D. H. S.; Wu, E. A.; Nguyen, H.; Chen, Z.; Marple, M. A. T.; Doux, J.-M.; Wang, X.; Yang, H.; Banerjee, A.; Meng, Y. S., Elucidating Reversible Electrochemical Redox of  $\text{Li}_6\text{PS}_5\text{Cl}$  Solid Electrolyte. *ACS Energy Lett.* **2019**, 2418-2427.
4. Nguyen, H.; Banerjee, A.; Wang, X.; Tan, D.; Wu, E. A.; Doux, J.-M.; Stephens, R.; Verbist, G.; Meng, Y. S., Single-step synthesis of highly conductive  $\text{Na}_3\text{PS}_4$  solid electrolyte for sodium all solid-state batteries. *J. Power Sources* **2019**, *435*, 126623.
5. Banerjee, A.; Tang, H.; Wang, X.; Cheng, J. H.; Nguyen, H.; Zhang, M.; Tan, D. H. S.; Wynn, T. A.; Wu, E. A.; Doux, J. M.; Wu, T.; Ma, L.; Sterbinsky, G. E.; D'Souza, M. S.; Ong, S. P.; Meng, Y. S., Revealing Nanoscale Solid-Solid Interfacial Phenomena for Long-Life and High-Energy All-Solid-State Batteries. *ACS Appl Mater Interfaces* **2019**, *11* (46), 43138-43145.
6. Doux, J.-M.; Yang, Y.; Tan, D. H. S.; Nguyen, H.; Wu, E. A.; Wang, X.; Banerjee, A.; Meng, Y. S., Pressure effects on sulfide electrolytes for all solid-state batteries. *Journal of Materials Chemistry A* **2020**, *8* (10), 5049-5055.
7. Doux, J. M.; Nguyen, H.; Tan, D. H. S.; Banerjee, A.; Wang, X.; Wu, E. A.; Jo, C.; Yang, H.; Meng, Y. S., Stack Pressure Considerations for Room-Temperature All-Solid-State Lithium Metal Batteries. *Adv. Energy Mater.* **2019**, 1903253.
8. Tan, D. H. S.\*; Xu, P.\*; Yang, H.; Kim, M.-c.; Nguyen, H.; Wu, E. A.; Doux, J.-M.; Banerjee, A.; Meng, Y. S.; Chen, Z., Sustainable design of fully recyclable all solid-state batteries. *MRS Energy & Sustainability* **2020**, *7*.

9. Wang, X.; Yang, Y.; Lai, C.; Li, R.; Xu, H.; Tan, D. H. S.; Zhang, K.; Yu, W.; Fjeldberg, O.; Lin, M.; Tang, W.; Meng, Y. S.; Loh, K. P., Dense-stacking porous conjugated polymer as reactive-type host for high performance lithium sulfur batteries. *Angew. Chem., Int. Ed.* **2021**.
10. Tan, D. H. S.\*; Xu, P.\*; Chen, Z., Enabling sustainable critical materials for battery storage through efficient recycling and improved design: A perspective. *MRS Energy & Sustainability* **2020**, *7*.
11. Tan, D. H. S.; Banerjee, A.; Chen, Z.; Meng, Y. S., From nanoscale interface characterization to sustainable energy storage using all-solid-state batteries. *Nat Nanotechnol* **2020**, *15* (3), 170-180.
12. Hirsh, H. S.; Li, Y.; Tan, D. H. S.; Zhang, M.; Zhao, E.; Meng, Y. S., Sodium-Ion Batteries Paving the Way for Grid Energy Storage. *Advanced Energy Materials* **2020**, 2001274.
13. Wu, E. A.; Jo, C.; Tan, D. H. S.; Zhang, M.; Doux, J.-M.; Chen, Y.-T.; Deysher, G.; Meng, Y. S., A Facile, Dry-Processed Lithium Borate-Based Cathode Coating for Improved All-Solid-State Battery Performance. *Journal of The Electrochemical Society* **2020**, *167* (13), 130516.
14. Tan, D. H. S.; Chen, Y.-T.; Yang, H.; Bao, W.; Sreenarayanan, B.; Doux, J.-M.; Li, W.; Lu, B.; Ham, S.-Y.; Sayahpour, B.; Scharf, J.; Wu, E. A.; Deysher, G.; Han, H. E.; Hah, H. J.; Jeong, H.; Chen, Z.; Meng, Y. S. Carbon Free High Loading Silicon Anodes Enabled by Sulfide Solid Electrolytes for Robust All Solid-State Batteries. *Science*. In Review.
15. Xu, P.\*; Tan, D. H. S.\*; Chen, Z.; Emerging Trends in Sustainable Battery Chemistries. *Trends in Chemistry*. In Review.
16. Chen, Y.-T.; Duquesnoy, M.; Tan, D. H. S.; Doux, J.-M.; Yang, H.; Deysher, G.; Ridley, P.; Franco, A. A.; Meng, Y. S.; Chen, Z. Fabricating High-Quality Thin Solid-State Electrolytes Films Assisted by Machine Learning. *ACS Energy Lett*. In Review.
17. Kim, M-C.; Ahn, N.; Cheng, D.; Xu, M.; Pan, X.; Kim, S. J.; Luo, Y.; Fenning, D. P.; Tan, D. H. S.; Zhang, M.; Ham, S-Y.; Jeong, K.; Choi, M.; Meng, Y. S. Imaging real-time amorphization of hybrid perovskite solar cells under electrical biasing. *Adv. Energy Mater*. In Review.

ABSTRACT OF THE DISSERTATION

Interface Characterization & Materials Designs for High Performance All-Solid-State Batteries

by

Darren Huan Shen Tan

Doctor of Philosophy in Chemical Engineering

University of California San Diego, 2021

Professor Ping Liu, Chair

All solid-state batteries (ASSBs) show great promise toward becoming the dominant next-generation energy storage technology. Compared to conventional liquid electrolyte-based lithium ion batteries, ASSBs utilize nonflammable inorganic solid-state electrolytes (SSEs), which

translate to improved safety and the ability to operate over a wider temperature range. Although the recent discoveries of highly conductive SSEs led to tremendous progress in ASSB's development, they still face barriers that limit their practical application, such as poor interfacial stability, scalability challenges and limited performance at high current densities. Additionally, efforts to develop sustainable manufacturing of lithium ion batteries are still lacking, with no prevailing strategy developed yet to handle recyclability of ASSBs.

Recognizing this, this dissertation seeks to evaluate SSEs beyond conventional factors and offer a perspective on various bulk/interface and chemical/electrochemical phenomena that are of interest to both the scientific community and the industry. Beginning from an introduction to the current state-of-the-art, rational solutions to overcome some major fundamental obstacles faced by the ASSBs will be discussed, strategies toward enabling scalability as well as potential designs for sustainable ASSB recycling models will be discussed.

Specifically, lithium solid-state battery systems were studied using sulfide based SSEs. The electrochemical reactivity of the argyrodite  $\text{Li}_6\text{PS}_5\text{Cl}$  system was studied, to gain insight into its reaction mechanisms, products, and reversible redox behavior. In terms of scalability, binder-solvent-sulfide compatibility was evaluated, in order to enable scalable roll to roll processability of thin and flexible sulfide SSEs. To overcome performance limitations at the anode, carbon free alloys electrodes were enabled, achieving high critical current densities and low temperature operation of ASSB full cells, addressing a key bottleneck in ASSB development. Finally, a fully recyclable ASSB model was designed, incorporating direct recycling approaches that reduce energy and greenhouse gas emissions compared to conventional recycling technologies.

Overall, this dissertation offers a deepened understanding of interfacial phenomena, and improved design strategies that translates into better material selection for high performance and sustainable ASSBs.

## Chapter 1. Introduction

### 1.1 Energy Storage – Its Role in the 21<sup>st</sup> Century

The past several decades has seen conventional lithium ion batteries (LIBs) dominate the portable devices and consumer electronics market. Today, LIBs are gradually penetrating other technologies including electric vehicles (EVs) and grid storage. Figure 1.1a shows the projected trends in global annual passenger vehicle sales. While total vehicle sales are not expected to increase significantly, the fraction of EVs that make up total sales are expected to match that of internal combustion engine cars by 2040. The success of LIB stems from the rapidly growing efforts in battery research and development, leading to vast improvements in materials performance and decrease in production costs. However, the justification for a more widespread adoption of LIB entails overcoming fundamental obstacles such as safety hazards from battery fires and explosions, meeting the demand for higher energy density, and achieving satisfactory performance in a wider temperature ranges for application in various climate conditions.

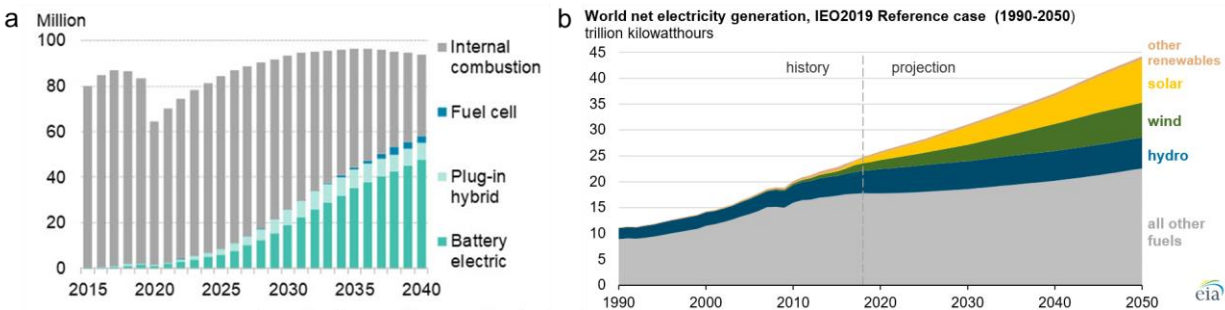


**Figure 1.1** a) Projected global annual passenger vehicle sales, showing increasing fraction of EVs.<sup>2</sup> b) Projected annual distribution of electricity generation, showing increasing proportion of energy generation from renewables that would translate into need for storage.<sup>3</sup>

Such demands are especially important where grid storage applications are considered, where renewables generated need to be stored in large quantities to serve electrical grids, where safety and robustness become key consideration factors for batteries. Figure 1.1b illustrates the growth in renewable energy penetration in world electricity generation over the next two decades, where solar, wind and hydro energy generation is expected to exceed energy generated from



traditional fossil fuels by the middle of the 21<sup>st</sup> century. Due to intermittency challenges in renewable energy supply and the inability to meet peak demand fluctuations typical of urban grids, renewable energy growth would inevitably translate into demand for battery energy storage. While other forms of energy storage including pumped hydroelectric and compressed air are currently being used, their shortcomings in flexible form factors as well as poor energy efficiencies prevent widespread adoption in developed societies.<sup>4</sup> As such, batteries will remain to be the dominant technology for large scale energy storage capable of serving our homes, cities, and off-grid communities.

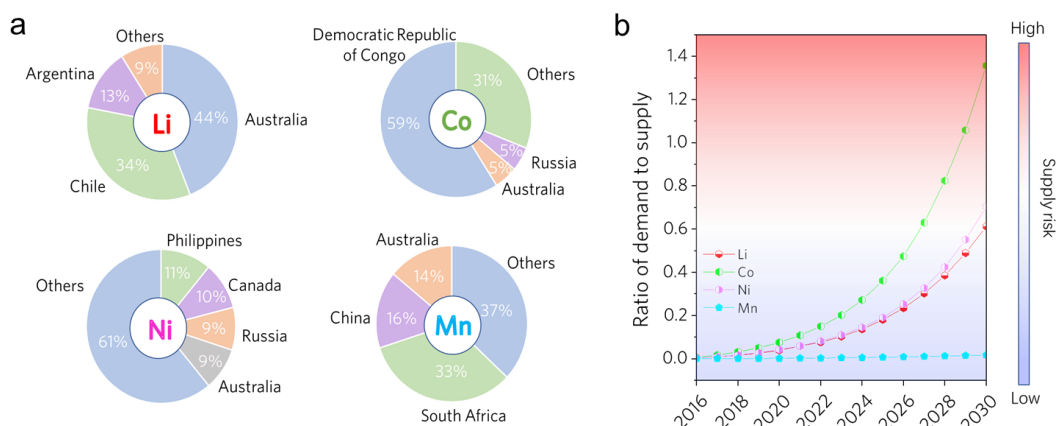


**Figure 1.2** (a) Global distribution of reserves and (b) evaluation of supply risk of critical materials for LIBs based on current trends in LIB growth.<sup>5</sup>

While promising trends in carbon footprint reductions and reduced reliance on fossil fuels are expected especially with the advent of next generation LIB technologies, developments in battery waste management and sustainable recycling are also lacking. This presents us with a growing and potentially dangerous battery waste accumulation problem<sup>6</sup>, especially as increasing number of EVs approach their end of life (EOL) and exit the roads. Compared to Pb-acid or other battery chemistries, supply of critical metals is a unique and urgent problem faced by LIBs. These critical metals include Li, Co, and other transition metals of significant economic value both due to their relative abundance within the earth's crust, as well as their disparate geographical availabilities.<sup>7</sup> For instance, as shown in Figure 1.2a, Australia, Chile and Argentina collectively

holds more than 80% of the world's Li reserves.<sup>8-9</sup> Similarly, 59% of the world's Co supply comes from the Democratic Republic of Congo (Figure 1.2a).<sup>9-11</sup> Such realities places significant material supply risks on critical metals especially for parts of the world without sufficient reserves as shown in Figure 1.2b. The major challenge faced in LIB sustainability lies with the fact that the current LIBs are not designed for recycling, making it difficult for existing LIB manufacturers and waste handlers to modify designs that favor efficient recycling.<sup>12</sup> Thus, it is prudent to explore new approaches to both fabricate and recycle next-generation batteries before they enter the market. The following chapters discusses the developments in next generation ASSBs to address our energy challenges as well as the potential for improved battery sustainability.

## **1.2 All Solid-State Batteries**

ASSBs are regarded as one of the future energy storage technologies that can compete with the state-of-the-art LIBs. Owing to the use of non-flammable solid-state electrolytes, ASSBs are well-placed to effectively eliminate battery safety concerns in electric vehicles, airline industry and grid storage applications in urban environments. Their wide operating temperature range also drastically reduces cooling power requirements with immediate benefits on costs and energy efficiency. While energy densities of ASSBs are virtually identical to those of LIBs at the materials level, they can be potentially increased by 50% or greater at the pack and system level from utilizing stackable formats without the need for individual cell packaging, reinforced metallic casings, or allocated space for coolants.<sup>13</sup>

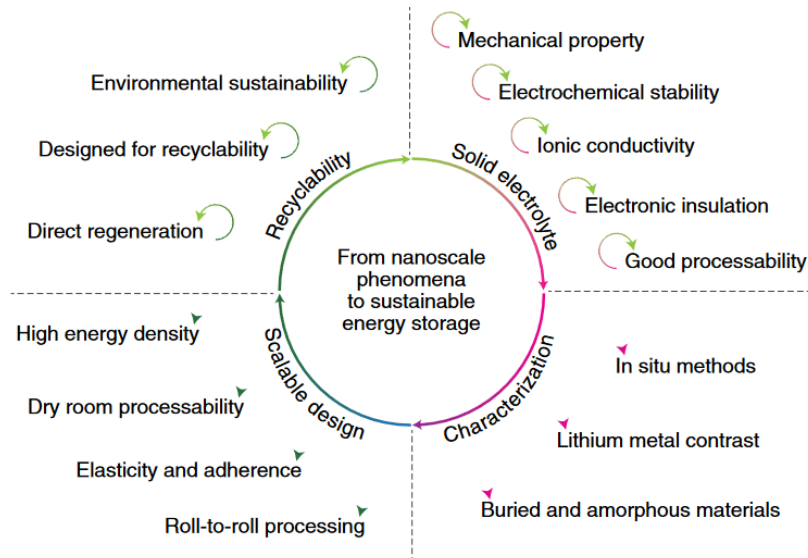


**Figure 1.3.** Summary of major scientific and engineering challenges for ASSB development.<sup>13</sup>

Despite their many promising benefits, ASSBs still face a multitude of barriers before they can be transferred from the laboratory to commercial manufacturing lines (Figure 1.3). In our view, the most pressing challenges are: (1) SSE and its interfacial stability: to date, no single SSE can meet the combination of properties necessary for commercialization: high ionic conductivity, ease of processability, wide electrochemical stability among others. (2) Characterization challenges: ASSBs are inherently difficult to characterize given the buried and heterogenous nature of their interfaces, leading to difficulties in understanding its electrochemical behaviors. (3) Scalable design: despite recent advances,<sup>14-15</sup> air sensitivity and poor mechanical properties of SSEs still pose challenges in implementing roll-to-roll processability for scalable ASSB fabrication. (4) Sustainability: no ASSB recycling models exist yet; any sustainable ASSB model would require cell level recycling strategies beyond electrodes recovery.

### 1.2.1 Solid State Electrolyte Chemistry

Scientists have recently discovered a plethora of SSE materials with ionic conductivities greater than  $10^{-2}$  S  $\text{cm}^{-1}$  at  $25^{\circ}\text{C}$ , comparable to that of liquid electrolytes.<sup>16</sup> However, high ionic conductivity alone is not sufficient to make cells practical. Recent reports on highly conductive

oxide- or sulfide-based SSEs show that poor interfacial stability makes them impractical.<sup>16</sup> Such instability arises from two types of reactions: (1) Interfacial reactions between the electrode and SSE, which occur spontaneously upon physical contact. (2) Electrochemical decomposition of the SSE itself during cell cycling at high voltage. Although some oxide-based electrolytes such as those from the garnet and NASICON class can be stable in a wide range of voltage,<sup>17</sup> this voltage window is still not satisfactory. Figure 1.4a illustrates the electrochemical stability windows of some SSEs compared to common electrode materials. Although polymer composite-based SSEs represent an important class of materials for solid-state batteries, these materials have already been extensively covered in the literature.<sup>18-20</sup> Thus, we will focus on inorganic solid electrolytes, which are comparatively novel and not as well understood. In this section, we discuss the fundamentals of each type of interfacial reaction and evaluate the methods to prevent them.

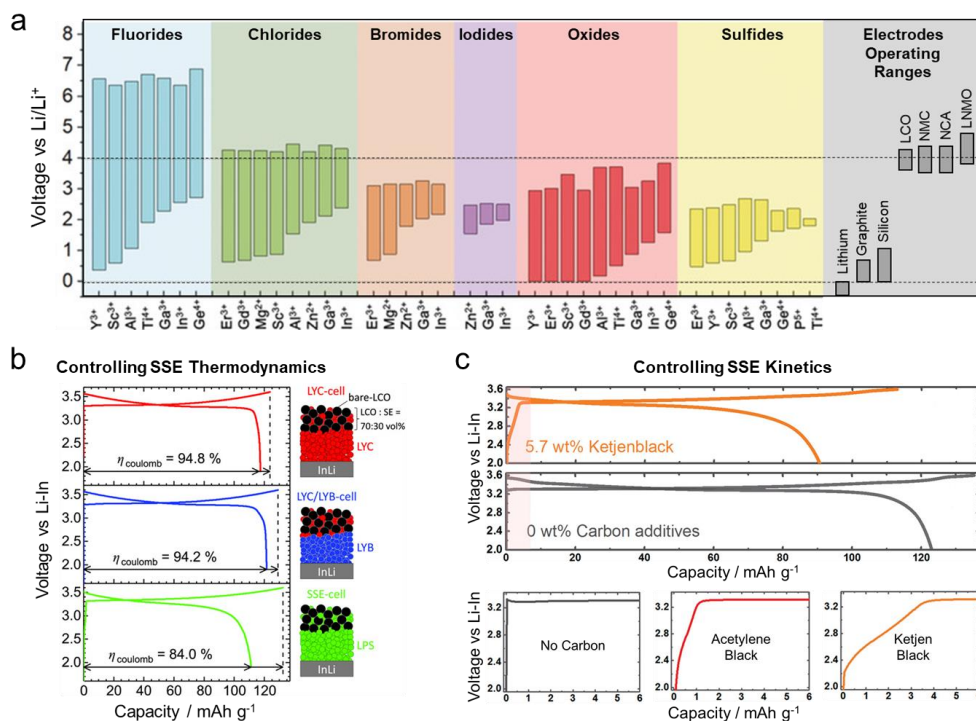


**Figure 1.4.** Electrochemical stability of various solid electrolytes and their effects on cell performance. a) Illustration of solid electrolytes stability windows vs common electrodes typical operating potential.<sup>21</sup> b) Methods to improve thermodynamic stabilities of solid electrolytes, by using solid electrolyte of higher oxidation stability.<sup>22</sup> c) Methods to control decomposition kinetics of solid electrolytes, by using carbon with lower specific area.<sup>23</sup>

### 1.2.2 Cathode Interfacial Reactions

The first type of interfacial chemical reactions stems from intrinsic chemical reactivity between the high-voltage cathodes and SSEs.<sup>24-25</sup> These spontaneous reactions result in the formation of transition metal oxides, sulfides, phosphates and other undesirable products on the cathode-SSE interface that increase cell polarization and limit rate capability. Oxide anions from the layered transition metal oxides form stronger electrostatic attractions with lithium ions ( $\text{Li}^+$ ) than sulfide anions due to the hard-soft acid base principle. Thus, transfer of  $\text{Li}^+$  from sulfides to oxides occurs until equilibrium is reached, thickening the resistive layer and suppressing any ionic conduction across the interface. As the transfer of  $\text{Li}^+$  from sulfide to oxide anions is charge-balanced by the electronic conductive network of the cathode material, the most natural approach to prevent this effect is to adopt an electronically insulating but ionically conductive coating layer at the SSE-cathode interface. Protective coating materials such as  $\text{Li}_2\text{SiO}_3$ ,  $\text{Li}_4\text{Ti}_5\text{O}_{12}$  (LTO),  $\text{LiTaO}_3$ ,  $\text{LiAlO}_2$ ,  $\text{Li}_2\text{O-ZrO}_2$ , and  $\text{LiNbO}_3$  (LNO) have been proposed.<sup>26</sup> For example, a 20-nm-thick LTO coating on  $\text{LiCoO}_2$  (LCO) can reduce cathode interfacial resistance by an order of magnitude compared to the uncoated cathode.<sup>27</sup> In addition, coating thickness as low as 5 nm of LNO is also adequate to prevent interfacial reactions.<sup>28</sup>

Protective coatings on the cathode can also alleviate cation interdiffusion problems along the SSE-cathode interface. Cation interdiffusion occurs from exchange between the transition metal ions and SSE cations. Interdiffusion can occur over spatial scales of up to 100 nm, forming a highly resistive layer that blocks  $\text{Li}^+$  from crossing the interface. Interdiffusion energies at the LCO (110) and  $\beta\text{-Li}_3\text{PS}_4$  (010) interface have been calculated and it has been found that Co and P ion diffusion exchange is highly thermodynamically favourable.<sup>29</sup> Adopting a protective layer such as LNO can prevent the Co and P interdiffusion, as Nb and P interdiffusion are slow due to the strong bonds between Nb and O anions. The effects of such a protective layer were later

experimentally validated with transmission electron microscopy (TEM) where long range Co distribution was tracked at the interface protected by a  $\text{Li}_2\text{SiO}_3$  coating.<sup>30</sup>

Despite these results, there is still a lack of consensus on how to select protective coating materials. For example, incorporation of charge carrier (such as in  $\text{LiAlO}_2$ ) in  $\text{Al}_2\text{O}_3$  improves cell efficiency,<sup>31-32</sup> most likely because of the energetically favorable activation of  $\text{Al}_2\text{O}_3$  with  $\text{Li}^+$  from the cathode during cell cycling. This hypothesis was experimentally supported by the effectiveness of  $\text{Li}_2\text{SiO}_3$  coating compared to  $\text{SiO}_2$  on LCO in improving the cell rate performance.<sup>30</sup> Regardless of the material, any coating must be sufficiently thin to avoid negative impacts on cell impedance, as oxides often exhibit low ionic conductivities (e.g.,  $10^{-8} \text{ S cm}^{-1}$  for LTO). Therefore, more conductive ( $\sim 10^{-6} \text{ S cm}^{-1}$ ) phosphate-based coating materials have been proposed; these exhibit both high theoretical oxidative stability and low ion migration barriers.<sup>33</sup> As experimentally shown for the NCM811/LPS interface, oxide cathodes tend to react with  $\text{PS}_4^{3-}$  groups in sulfide-based SSEs due to the exchange of O and S atoms between the SSE and the cathode to form  $\text{PO}_4^{3-}$  units.<sup>34</sup> Because the bond dissociation energy of a P-O bond (597 kJ/mol) is larger than that of a P-S bonds (346 kJ/mol), O-S exchange is highly favorable. Thus, the reactivity of phosphate-based coating materials in which P atoms are already bonded to O atoms is expected to be low.

### 1.2.3 Anode Interfacial Reactions.

In general, there are two kinds of interfaces formed between SSEs and lithium metal: ionically conductive and mixed conductive ones. For example,  $\text{Li}_{10}\text{GeP}_2\text{S}_{12}$  (LGPS) has an ionic conductivity greater than  $10^{-2} \text{ S cm}^{-1}$  and decomposes upon contact with lithium metal,<sup>17</sup> forming  $\text{Li}_2\text{S}$  (an insulator),  $\text{Li}_3\text{P}$  (an ionic conductor) and Li-Ge alloy (an electronic conductor); collectively making the interface a mixed conductor, such as that seen in Figure 1.5a.<sup>35</sup> Because of the presence of a conductive component, as the interface grows, the anode impedance increases until cell failure. The same principles apply for Si-, Sb-, Sn- and As-containing SSEs, as they also

form electronically conductive alloys with lithium. As such, despite their high ionic conductivity, these electrolytes are not suitable for lithium metal ASSBs. On the other hand, LPS-based glasses or glass ceramics ( $x\text{Li}_2\text{S}\cdot y\text{P}_2\text{S}_5$ ), along with argyrodite-based SSEs ( $\text{Li}_6\text{PS}_5\text{X}$ ,  $\text{X} = \text{Cl}, \text{Br}, \text{I}$ ) are more stable (Figure 1.5b). When these SSEs meet lithium metal, their decomposed products include  $\text{Li}_2\text{S}$ ,  $\text{Li}_3\text{P}$ , and  $\text{LiX}$  ( $\text{X} = \text{Cl}, \text{Br}, \text{I}$ ), which are all electronically insulating,<sup>17</sup> thus passivating the SSE interface.

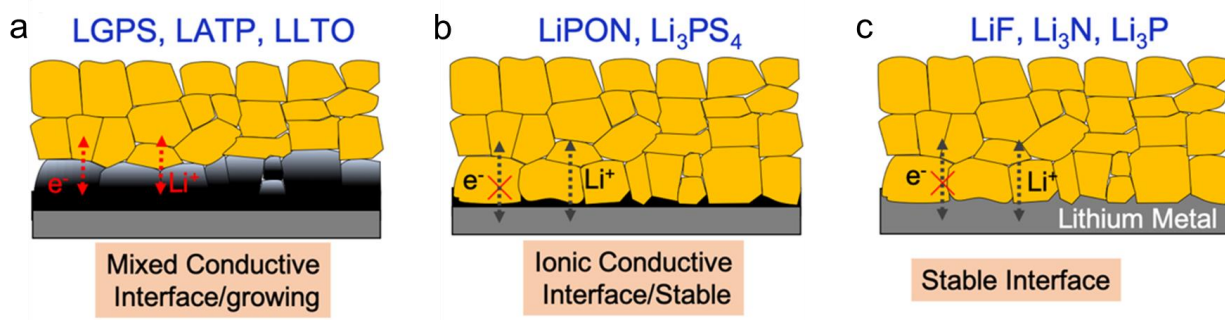


**Figure 1.5.** Anode Interfacial Types: (a) SSEs that are not stable and do not form stable interfaces, as a result of reaction products that are both ionically and electronically conductive. (b) SSEs that are not stable but form a stable and passivating interface, and (c) reaction products formed are stable with metallic Li.<sup>36</sup>

Room temperature long cycle performance of lithium metal ASSBs still remains challenging. One reason is the difficulty of maintaining good wettability at the lithium-SSE interface during cell cycling in order to achieve homogenous and dense lithium plating. In an effort to overcome this problem, conformal alumina coating on lithium has been shown to reduce interfacial resistance by almost two orders of magnitude in oxide-based SSEs.<sup>37</sup> However, such treatments are only feasible with garnet and other oxide-based SSEs due to their better chemical stabilities against lithium. For sulfide-based SSEs, any high temperature treatment would promote unwanted reactions and form a thick solid electrolyte interface (SEI) that renders cells unusable. While some studies demonstrated good lithium-SSE contact by simple cold pressing,<sup>38-39</sup> the effectiveness of this methodology in lowering interfacial resistance and allowing uniform lithium plating especially in long term cell cycling is still unclear. Another solution could be the use of a

thin Li<sup>+</sup> conductive polymer layer between the lithium anode and the SSE. This strategy was previously shown to enable extended cell cycling in Li|polyethylene oxide (PEO)|Li<sub>7</sub>La<sub>3</sub>Zr<sub>2</sub>O<sub>12</sub> (LLZO) and Li|PEO|β-LPS configurations.<sup>40-41</sup> However, using conductive polymers often requires cells to be cycled at elevated temperatures. The good cyclability of these cells is often attributed to PEO's ability to either protect lithium or achieve good wettability. Even though there have also been reports of bare Li|SSE cell configurations showing good cell cyclability at elevated temperatures,<sup>42-43</sup> practical devices must be operated at room temperature. Prevailing theories suggest that lithium dendrites propagate as a result of deposition within pores near the lithium-SSE interface<sup>44</sup>, with experimental reports observing lithium deposits originating from pores at the interface that propagate along grain boundaries due to inhomogeneous current distribution.<sup>45</sup> However, studies using grain-free single crystal Li<sub>6</sub>La<sub>3</sub>ZrTaO<sub>12</sub> also reported lithium penetration through the SSE.<sup>46</sup> Interestingly, only lithium phosphorous oxynitride (LiPON) appear to be able to effectively prevent lithium dendrite formation and enable cell cyclability beyond 10,000 cycles (Figure 1.5c).<sup>47-48</sup> It is probably the amorphous, conformal and virtually defect free nature of the material that is responsible for such performances.

In spite of the challenges faced at the anode interface, metallic lithium is still indispensable to increase energy densities of ASSBs. Moreover, lithium metal ASSBs can potentially be used in an anode-free configuration. Such ASSBs have been demonstrated in thin film formats nearly two decades ago in a LiPON|LCO battery.<sup>47</sup> Here, surface passivation in solid electrolytes prevents side reactions from continuously forming, allowing retention of the lithium reservoir within the cell after the first charge cycle. This situation differs fundamentally from that in liquid electrolytes where continuous formation of new SEI and dead lithium at each cycle requires sacrificial lithium replenishment<sup>49</sup>. Adoption of anode-free cell configurations would immensely simplify large scale ASSB processing and lower its cost, because it would eliminate sophisticated lithium metal lamination and interface treatment steps, especially when lithiophobic SSEs are



used.<sup>50</sup> However, the same challenges encountered in other lithium metal ASSBs, such as dendritic cell shorting, also apply in anode-free cell configurations.

#### 1.2.4 SSE Electrochemical Decomposition

Despite the fact that protective coating layers can effectively reduce interfacial reactions, they cannot prevent interfacial electrochemical decomposition. Electrochemical decomposition during cell charging is an unavoidable intrinsic thermodynamic phenomenon of the SSE. The SSE at each electrode experiences a strong oxidative or reductive environment that leads to the formation of unwanted interfacial products, resulting in poor first cycle coulombic efficiencies and high impedance growth. To reduce the effects of electrochemical decomposition, SSE thermodynamics can be altered through compositional changes. For instance, introducing oxygen dopants stabilizes the electrolyte, because oxides are more thermodynamically stable than sulfides due to their lower anion polarization. In one study,  $P_2O_5$  was introduced in place of  $P_2S_5$  during SSE synthesis, forming oxygenated units within the bulk  $Li_3PS_4$  glass ceramic oxysulfide system.<sup>51</sup> The electrochemical stability window of oxysulfides with the composition  $Li_{10}GeP_2S_{12-x}O_x$  (LGPS) is wider than that of the oxygen-free counterpart, with only a small tradeoff in bulk ionic conductivity.<sup>52</sup> Alternatively, SSE thermodynamics can be controlled by using different SSEs with suitable redox stability at each electrode. Figure 1.4b compares the improvements in first cycle coulombic efficiency by using SSEs with higher oxidative stability. For example, halide-based  $Li_3YCl_6$  resulted in reduced SSE decomposition and an improved first cycle coulombic efficiency of 94%, from 84% when sulfide-based  $Li_3PS_4$  was used.<sup>22</sup>

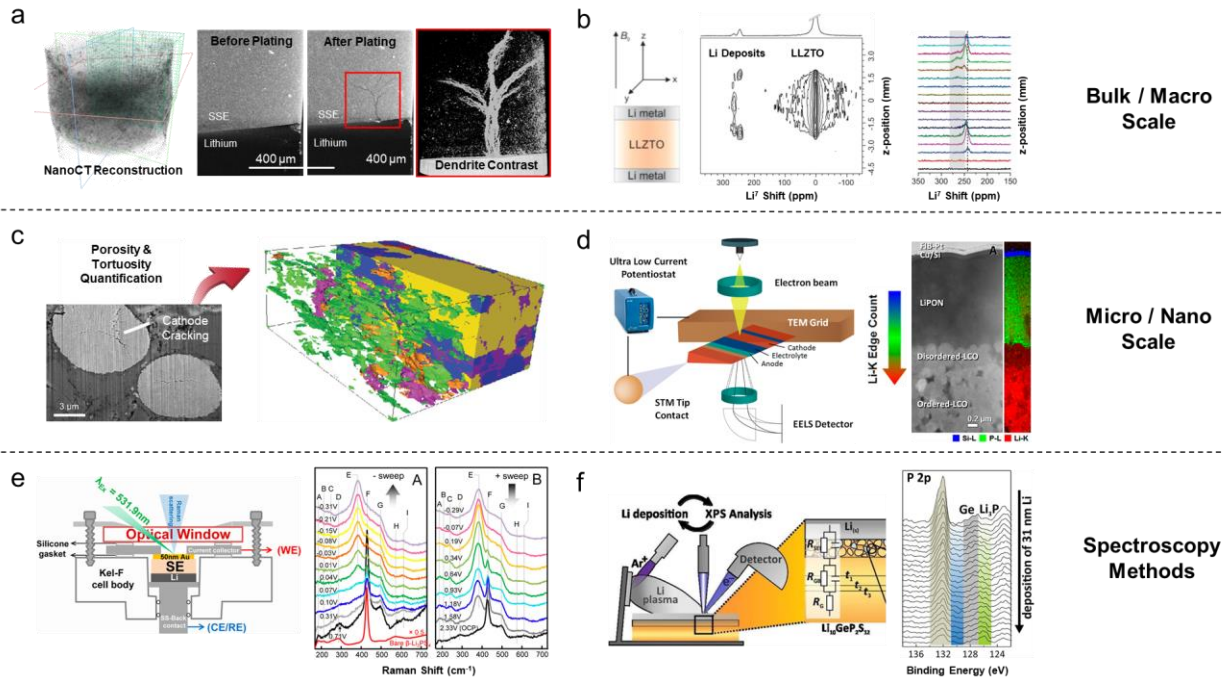
Although studies using conventional cyclic voltammetry (CV) measurements have claimed SSE electrochemical stabilities up to 5 V or higher, recent reports using both modified CV measurements and first principles calculations have shown a narrower electrochemical voltage window. For example, LGPS, previously claimed to be stable up to 5 V with lithium metal,<sup>53</sup> was found to decompose at 2.2 V vs  $Li/Li^+$ .<sup>54-55</sup> These inconsistencies in stability were also found in

oxide-based SSEs such as  $\text{Li}_7\text{La}_3\text{Zr}_2\text{O}_{12}$  (LLZO) and  $\text{Li}_{1+x}\text{Al}_x\text{Ti}_{2-x}(\text{PO}_4)_3$  (LATP), where oxidative decomposition was reported to be higher ( $>5\text{V}$ ) than their predicted values ( $<3.7\text{V}$ ).<sup>56-57</sup> These contradictory reports can be explained by the fact that experimental methods are sometimes unable to account for the sluggish redox kinetics of SSEs. In one example, instead of the common CV with metal current collectors, a modified process where SSE was mixed with carbon and applied on the cathode was consistent with the electrochemical stability windows derived from first principles calculations.<sup>55</sup> The use of carbon provides electronic pathways that facilitate redox of the SSE, allowing oxidation to be detected at its intrinsic thermodynamic potentials.

However, poor redox kinetics can in turn be applied to tune SSE oxidation. As decomposition products tend to deposit around the carbon additives or the surface of cathode particles, an ideal approach would involve minimizing SSE exposure to conductive surfaces, while providing long range electronic pathways between electrode materials and the current collector. As seen in Figure 1.4c, the kinetics of SSE decomposition can be reduced by selecting a specific surface area of the carbon additives.<sup>23</sup> Carbon materials with low surface area ( $<100\text{ m}^2\text{ g}^{-1}$ ) and long range conductive capability, such as carbon nanotubes or vapor grown carbon fiber are ideal additives for ASSBs, because they reduce SSE decomposition and maintain high capacity utilization.<sup>23, 41</sup> A detailed experimental validation of SSE reversible redox kinetics along with analysis of its reaction products are discussed in chapter 2.

### 1.3 Characterization Challenges

Challenges to characterize ASSBs often relate to the difficulty of probing buried and/or beam sensitive interfaces. Even though a wide spectrum of available tools exists, they are limited in characterizing only specific chemistries within solid-solid interfaces. These include metallic lithium dendrites formation and growth of amorphous interfacial products within SSEs at both bulk and localized sites. Only in few cases it is possible to characterize the true dynamic states within ASSBs with *in-situ* and *operando* techniques. As such, recent literature reviews covering broad characterization topics have called for novel techniques to address this gap in knowledge.<sup>58-60</sup> In this section, we cover the state-of-the-art developments in experimental design for the characterization of ASSBs and offer possible solutions to address some of the most urgent problems.



voids within the SSE. Thus, CT methods can be more effective when applied to cathodic interfaces where there is a larger X-ray contrast between cathode particles and SSEs. Several studies have quantified voids or cracks within the cathode composite using CT.<sup>66-67</sup>

To probe buried interfaces, neutron-based techniques are especially useful. Neutron depth profiling (NDP) is effective to study lithium dendritic growth, as it is nondestructive and lithium-sensitive. In one example, cell shorting was diagnosed using NDP, where time-resolved lithium concentrations at the SSE-lithium interface were obtained as lithium was plated and stripped. It was found that increased accumulation of metallic lithium within the buried SSEs under high current densities was the likely cause for poor stripping reversibility and eventual cell shorting.<sup>68</sup> Another study used NDP to compare the dynamic evolution of lithium concentration in lithium-SSEs interfaces of LiPON, LLZO and Li<sub>3</sub>PS<sub>4</sub> during Li plating. It was observed that lithium plating in LiPON remained uniform and unchanged throughout the process, in agreement with previous literature on lithium-LiPON interfaces. Microstructural lithium dendrite formation within buried SSEs can also be characterized using <sup>7</sup>Li nuclear magnetic resonance (NMR). Making use of non-destructive probes along with its high sensitivity toward Li<sup>+</sup> in bulk SSEs, <sup>7</sup>Li NMR chemical shift imaging was used to track lithium growth in Li<sub>6.5</sub>La<sub>3</sub>Zr<sub>1.5</sub>Ta<sub>0.5</sub>O<sub>12</sub> (Figure 1.6b). The increase in microstructural growths were subsequently correlated with symmetric cell plating and stripping voltage profiles, and it was found that voltage spikes often seen in ASSBs before cell failure can be attributed to dendrites that fuse (break) due to lithium melting during localized cell shorting.<sup>1</sup> However, the limited spatial resolution in such imaging techniques restricts detection to the micron-range (~100 μm). More sensitive techniques are needed to observe the initial onset of lithium nucleation, as these formations are likely to be nanometer-sized deposits within the SSEs.

### 1.3.2. Characterizing Meso to Nano-scale Interfaces

To explore ASSB mesoscale properties, we need to revert to cryogenic-focused ion beam (FIB) techniques (Figure 1.6c). These methods can help quantify porosity and volume changes

within the ASSBs at spatial resolutions under 1nm without damaging the SSE or SEI. By keeping the sample temperatures low enough, local heating during exposure to Ga<sup>+</sup> ion beams can be prevented, allowing imaging of lithium metal at 100 K.<sup>69</sup> Considering the heterogeneous nature of the SEI layers, especially for thick electrodes, Xe<sup>+</sup> plasma FIB can be applied for large volume serial section tomography as the ion milling rates are at least 60 times greater than conventional Ga<sup>+</sup> FIB. Large volume tomography combined with window-less energy dispersive spectroscopy (EDS) can be used to monitor the SEI formation or cracking, electrode porosity and tortuosity evolution, and SEI layer elemental distribution changes in the 3D meso-structure. An example is illustrated in Figure 1.6c where 3D reconstruction was used to quantify porosity as well as pores interconnectivity within an ASSB.<sup>61</sup> However, any reconstruction method using the FIB would be limited by the spatial resolutions of its detector - a scanning electron microscope (SEM) in this case. Additionally, the secondary electron signal intensities at cryogenic temperatures are low and charges from the probe beam can accumulate on electronically insulating SSEs, limiting the effectiveness of the method.

One strategy to overcome these challenges is the use of a solid-state nanobattery configuration for interface characterization (Figure 1.6d). To do so, FIB is first used to slice a cross-sectional lamella from a thin-film ASSB. This lamella preserves the full function of the ASSB and is thin enough (~100 nm) to be used in a TEM. This approach was used to show electrochemical cyclability of a cross section LCO/LiPON/amorphous-Si thin film battery.<sup>70</sup> A wedge-shaped nano ASSB prepared by FIB was then placed onto a potentiostat coupled platform, allowing *in-situ* cycling of the nano ASSB within the TEM. Using a combined scanning TEM-electron energy loss spectroscopy (EELS), the decomposition products consisting of lithium oxides and peroxides and oxidized cobalt species could be observed at the cathode-SSE interface (Figure 1.6d). Although such *in-situ* TEM characterization has been demonstrated for thin-film LiPON based batteries, its principles can be applied for sulfide and oxide based ASSBs

too, where sputtering or other vapor deposition methods can be used to fabricate nanobattery interfaces for the analysis.

### 1.3.3. Spectroscopy Techniques

Various spectroscopy-based *in-situ* methods have been adopted to probe electron beam sensitive and amorphous interfacial products. Of these, in situ Raman spectroscopy is a simple and robust method to provide good contrast in SSEs due to the strong scattering signals of covalently bonded interfacial products. With this technique, formation of various lithium thiophosphates, such as  $P_2S_6^{4-}$  or  $PS_4^{3-}$ , can be easily distinguished during lithium plating at a gold-LGPS interface (Figure 1.6e). Thiophosphate signals would otherwise be very difficult to distinguish with EELS, because this technique is sensitive to the P-S bond, which is present in both species. Limitations of in situ Raman include the inability to detect certain Raman inactive materials, especially ionic species such as lithium salts. Raman techniques also tend to be noisy especially from heterogeneous SSE interfaces, owing to the presence of absorbing or blocking materials such as carbon. One approach to overcome this issue is combining higher energy surface sensitive XPS with *in-situ* deposition of lithium metal onto sulfide based LGPS (Figure 1.6f). This allows detecting both chemical bonds and intrinsic band-structure, as well as observing the chemical decomposition products such as  $Li_3P$ ,  $Li_2S$ , and Li-Ge alloy at the lithium-SSE interface.<sup>35</sup> However, its capability to capture subsurface (>10nm) interfaces formation is limited by the escape depth of ejected photoelectrons. To address this issue, X-ray absorption spectroscopy (XAS) has been used in fluorescence mode to study oxidative decomposition of  $Li_3PS_4$ ,<sup>71</sup> where oxidized products of S and  $P_2S_5$  were found in buried interface, in agreement with previous computational work.<sup>17</sup>

Spectroscopy methods can also be utilized to qualitatively deconvolute chemical reactions from electrochemical reactions. This can be done through careful selection of their respective states of charge. For example, to probe chemical reactions between charged cathodes and SSEs

without contributions from electrochemical decomposition, characterization can be conducted for mixtures of pristine SSEs and charged cathodes harvested from liquid electrolyte cells. Likewise, purely electrochemical reactions can be analyzed by characterizing SSE-carbon composites in the absence of transition metal oxide cathodes.<sup>71</sup> The next chapter discusses how such characterization tools are employed to investigate the reversible redox behavior of sulfide SSEs.

## **1.4 Scalable Design – Organic/Inorganic Composites**

### **1.4.1. Role of Polymers in Scalable Fabrication**

To achieve practical energy densities, SSE layers need to be thinner than 50  $\mu\text{m}$ . However, poor mechanical properties of inorganic SSEs make them brittle, posing challenges for processing ASSBs in large formats. Polymer composites can improve mechanical flexibilities of SSE composites, allowing roll-to-roll manufacturing, with good elasticity and adhesion to current collectors. Figure 1.7a illustrates a typical manufacturing process of ASSBs using wet slurry processing methods similar to those in conventional LIBs.<sup>72</sup> However, unlike conventional LIBs manufacturing where common solvents such as water or N-methyl-2-pyrrolidone (NMP) and binders such as carboxymethyl cellulose (CMC) or polyvinylidene fluoride (PVDF) are used, careful consideration must be taken to ensure these solvents are chemically compatible with SSEs. While polyethylene oxide (PEO), polyvinylpyrrolidone (PVP), CMC and PVDF have been adopted in oxide-based ASSBs,<sup>73-74</sup> they cannot be used with sulfide-based SSEs. Electron-rich atoms within the polymer backbone, namely O, N and F, tend to form electrostatic interactions with the strong nucleophilic cations containing aliovalent atoms such as P or transition metals. This can result in localized SSE-binder agglomerations that impede both ionic conductivity and adhesive properties of the polymer. As such, favorable ASSB binders involve polymers with low or no electronegative functional groups, such as poly(acrylonitrile-co-butadiene) (NBR), polystyrene-block-polybutadiene (SBS) or styrene-ethylene-butylene-styrene (SEBS) reported in several cases; usually only 2wt% of binder is needed to achieve sufficient adhesion.<sup>75-77</sup> While



using non-polar binders may lead to poor adhesion between electrodes and current collectors, stack pressures typically applied in ASSBs can circumvent these concerns. Homogeneous electrode distribution is also a crucial factor for ASSBs, because poor particles wettability impedes capacity utilization. As such, binders that can be processed dry are promising candidates for ASSBs because they enable uniform distribution of the SSEs and active particles within the cathode composites.<sup>78</sup>

Whenever solution processing is used, considerations for solvent and binders compatibility with sulfide-based SSEs must be made<sup>79</sup> (Figure 1.7b). Only solvents with polarity index below 3.1 are fully compatible with sulfide-based SSEs.<sup>80</sup> In addition, the stability of the SSEs in ambient conditions need to be considered. Sulfides spontaneously undergo hydrolysis when exposed to moisture, producing H<sub>2</sub>S gas, a safety hazard when not properly vented. ASSB manufacturing should be done under dry-room conditions, similar to that of conventional LIBs. Trace amounts of moisture even in ppm levels can already be detrimental for the extremely hygroscopic sulfide SSEs. Studies have demonstrated improved moisture stability of sulfide SSEs using partial substitution of stable oxides into the bulk SSE.<sup>81</sup> Alternatively, to avoid modifying the intrinsic electrochemical properties of the SSE itself, hydrophobic binders can be adopted during processing.<sup>76</sup>

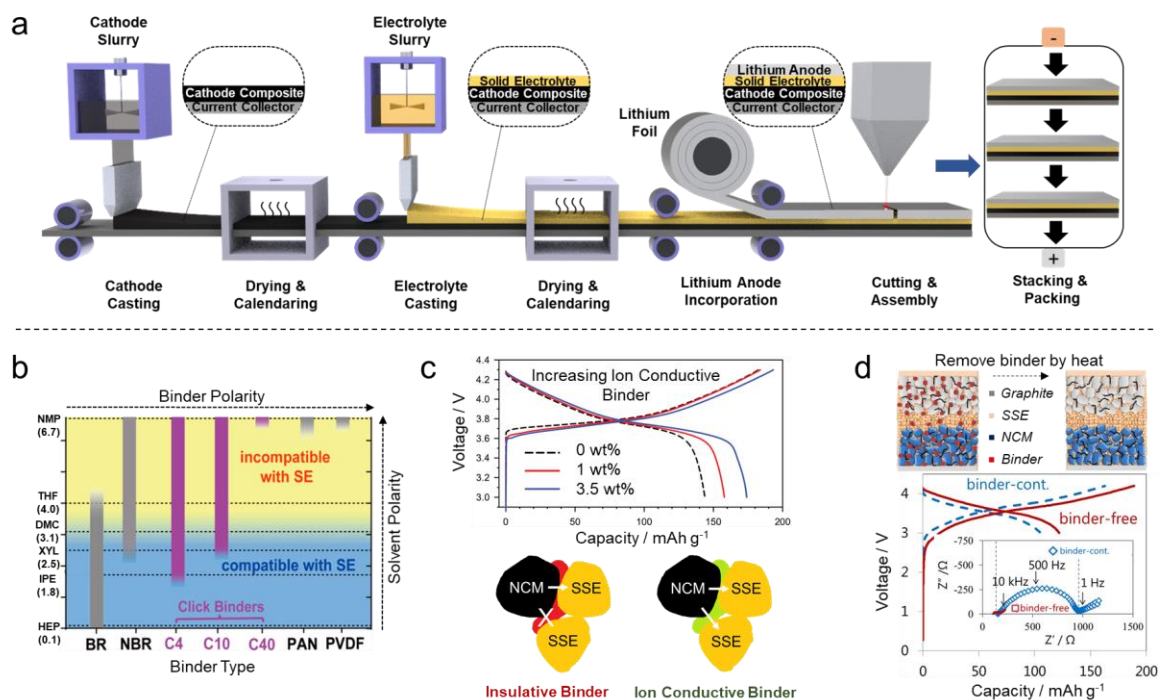


**Figure 1.7.** Manufacturing considerations for ASSBs and the role of polymeric binders. a) Schematic of large-scale manufacturing of ASSBs. Polymer & solid electrolyte composites allow for good mechanical processability as well as decreased separator thickness layers to increase cell-level energy density.<sup>72</sup> b) Binder & solvent selection compatibility, showing the polarity window that binders and solid electrolytes are compatible.<sup>80</sup> c) Role of ionically conductive binder to improve conductive pathway and inter-particle contact.<sup>82</sup> d) Binder-free cell fabrication reduces cell impedance and improves performance.<sup>83</sup>

#### 1.4.2. Resistive Effects of Polymers

In general, it is expected that by mixing a SSE with a binder decreases its conductivity by about an order of magnitude. This is due to the impedance contribution across the polymer-SSE interface as a result of the presence of insulating binder along the grain boundaries.<sup>77</sup> However, solvated ionic liquids (SILs) can reduce binder-induced impedance as well as fill any pore generated in the polymer composite. This strategy has been utilized to increase ionic conductivities by one to two orders of magnitude of oxide-based polymer-SSE composites.<sup>57, 84</sup> However, this can be difficult to achieve in sulfide-based SSEs, as polar solvents that solvate lithium salts will chemically degrade the sulfides. This contradiction can be resolved by controlling the ratio between the salt and solvent. As the proportion of salt to solvent increases until saturation,

a critical salt-solvent complex point is reached, forming a SIL with no available free solvent left to react with or dissolve sulfide SSEs. In one example, when four moles of triglyme G3 ethers were added to 1 mol of LiTFSI, a saturated solvent–salt complex,  $\text{Li}(\text{G3})_4$  was formed. This complex was found to not affect the sulfide SSE.<sup>85</sup> However, incorporation of any solvated ionic liquids in ASSBs such as LiG3 would also inevitably lower the thermal stability of the entire system. Thus, an alternative is the use of ionically conductive binders by solvating the insulating binders with lithium salts (Figure 1.7c).<sup>86</sup> In one case, a composite of  $\text{Li}_6\text{PS}_5\text{Cl}$  and NBR-Li(G3)TFSI solvated binder was applied<sup>82</sup>, improving the cell rate capability and capacity utilization while maintaining good thermal stability. To eliminate the binder impedance contribution, binder-free ASSB cell fabrication has also been proposed. While binders play an important role during the manufacturing process, it is no longer needed once the cell is assembled. As a binder only acts as inactive material, it would be ideal for it to be removed after assembly. Figure 1.7d depicts a heat treatment process that allows for the removal of volatile poly (propylene carbonate)-based binder within the cell after fabrication.<sup>83</sup> However, as the volume occupied by the binder is not filled by SSEs after removal, increased porosity within the ASSBs could potentially occur. As such, this temperature treatment technique can be done under stack pressure, allowing the thermally softened SSEs to deform and fill any pores generated within the solid electrolyte bulk.

## **1.5 Battery Recycling & Sustainability**

### **1.5.1. Battery Recycling Challenges**

With rapidly increased LIBs adoption, the need for sustainable battery recycling is a matter of utmost importance. Spent LIBs contain lithium, cobalt, nickel and other transition metals that are not only economically valuable but are also limited in terms of their natural availabilities. Unfortunately, today's LIBs are not designed to be recycled easily.<sup>87</sup> To re-design batteries for recycling instead of disposal, battery manufacturers will need to modify their established

production protocols, with evident economic backlash. While this might be too late for conventional LIBs, it is prudent to design potential recycling strategies such that future ASSB manufacturers can consider it as part of a sustainable production-to-recycling manufacturing process. Figure 1.8a depicts the battery manufacturing chain from materials mining to disposal.<sup>88</sup> While recycling efficiencies for lead acid batteries exceed 99% in major parts of the world<sup>89</sup>, such as in Europe and USA where recycling is led by strong government mandates, much more can be done to improve recycling rates for end-of-life LIBs and future ASSBs. Moreover, commercial LIBs should be regulated to include labelling of their chemical classifications, to allow ease of recycling and sorting based on their core materials. This would require the cooperation of battery manufacturers and policy makers, in efforts to streamline recycling of respective LIB chemistries. The responsibility can be further extended to original equipment manufacturers as well as EV manufacturers to incentivize battery buy-back programs as part of their in-house recycling or repackaging for secondary use.

The most common recycling technologies adopted today to break down recovered cathode materials and regenerate them for reuse are pyrometallurgical and hydrometallurgical methods. Recent studies on such methods have reported valuable metal recovery rates exceeding 95% using acid leaching followed by chemical precipitation methods.<sup>90-92</sup> The recovered metals in their precursor forms are subsequently used in cathode re-synthesis with co-precipitation, sol-gel or solid state heat treatment steps to reform the active materials. However, these methods tend to be energy intensive, costly and use toxic chemicals processing which can be difficult to handle.<sup>93</sup> Additionally, materials recovery efficiency as a fraction of the entire cell still remains low, due to low recycling rates of other components in the cell such as the liquid electrolytes, lithium salts, separator and additives. To address these shortcomings, the US Department of Energy's ReCell Center has set out core principles of battery recycling that involves design for recyclability, direct regeneration and recovery of other components.<sup>88</sup> Achieving these goals requires a paradigm shift in the way researchers think about battery recycling, to go beyond

metals recovery or materials processability, and to consider LIBs and ASSBs recycling from a wider perspective.<sup>92</sup> Given the lack of reports on ASSBs recycling in the literature, this framework presents an opportunity to explore possible pathways for recycling ASSBs using the goals of ReCell as a starting reference point.

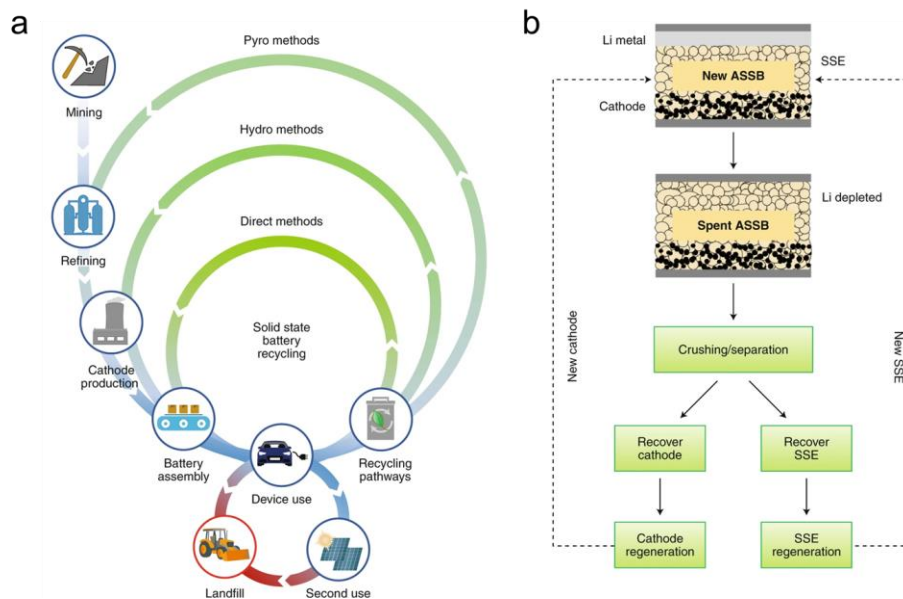


**Figure 1.8.** a) Illustration of various recycling methods.<sup>88</sup> b) Schematic of potential closed loop all solid-state battery recycling process.

### 1.5.2. Fully Recyclable ASSB Model

For any ASSB recycling model to be sustainable and practical, several technical challenges need to be addressed: (1) designing ASSB cell chemistries that allow for efficient materials disassembly with reduced processing steps; (2) avoid using toxic, expensive, and difficult-to-process organic solvents; (3) recovering all components in a battery, rather than just the cathode, in a cost-effective manner; (4) designing a scalable, closed loop ASSB recycling model applicable to a variety of ASSB formats (Figure 1.8b).

Fortunately, compared to conventional liquid-electrolyte-based LIBs, recycling of ASSBs has several advantages. Due to its large stackable formats, ASSBs can be discharged at the pack level before disassembly; and its intrinsic non-flammability also mitigates safety hazards during

packaging breakdown. Conversely, fire and gas evolution hazards in LIBs require individual cells to be submerged typically in salt solution to achieve zero state of charge. However, the major challenge for a recyclable ASSB model is separation of SSEs from electrodes and its subsequent recovery. Unlike liquid electrolytes that can be removed with organic solvents or supercritical drying during dismantling<sup>91, 94</sup>, SSEs contains a host of various metallic and non-metallic elements (oxides, sulfides). Elemental separation and purification of these SSEs can be difficult with conventional recycling approaches. While solution type dissolution and precipitation methods of SSEs might be effective, the fact that transition-metal oxide chemistries are similar in both oxide-based SSEs and cathode materials make it challenging to selectively separate each component via dissolution. Fortunately, this should not be the case in sulfide-based ASSBs, where sulfide dissolution can be done using cheap and safe solvents such as ethanol or acetonitrile to recover sulfide-based SSEs from spent ASSBs.<sup>95</sup> Unlike previous studies that reported chemical incompatibilities between polar solvents and sulfides,<sup>80</sup> it has been found that such polar solvents will only cause dissolution and not chemical degradation of certain SSEs, allowing them to be precipitated in its original chemical formula. Solution-based processing of sulfide-based SSEs using such solvents has been already demonstrated in previous solution synthesis work.<sup>96-98</sup> This is often seen in sulfide-based SSEs comprising of  $\text{PS}_4^{3-}$  conductive thiophosphate units that can be easily solvated with polar solvents and precipitated as either  $\text{Li}_3\text{PS}_4$  or  $\text{Li}_6\text{PS}_5\text{X}$  ( $\text{X} = \text{Cl}, \text{Br}$  or  $\text{I}$ ) forms. By contrast, conventional LIB cells need to be separated into their subcomponents before washing away the electrolyte solvents and salts. Moreover, ASSBs contain no ethers, salts or separators and its SSEs can potentially be fully recovered without energy intensive organics processing. This provides a promising opportunity for simple recovery and recycling of SSEs from spent ASSBs.

### **1.5.3. Direct Regeneration of SSEs and Cathodes**

A crucial requirement for any robust recycling model is the need to avoid the breakdown of spent electrodes and SSEs to their precursor forms. As such, direct regeneration methods would be superior to existing energy intensive pyrometallurgical or hydrometallurgical methods, as they substantially reduce the energy and processing costs of recycling. Conceptually, spent bulk SSEs do not undergo any structural change aside from fractional decomposition in the SEI. Thus, the majority of the SSE can be recovered and directly regenerated without sophisticated re-synthesis processes using dissolution-precipitation methods combined with mild post processing. Although sulfide SSE dissolution processes can result in conductivity losses of 1 to 2 orders of magnitude<sup>96-97</sup>, this is mainly due to the small grain sizes and poor crystallinity of recovered SSEs, not to chemical degradation of the SSE itself. It has been shown that mild annealing can be carried out for precipitated SSEs to regain its pure phase and ionic conductivities greater than  $1 \text{ mS cm}^{-1}$ .<sup>96-97</sup> Such techniques can allow simple and low-cost recovery of lithium in its reusable SSE form.

Aside from the SSE, direct regeneration of spent electrodes is also possible. Previous nanoscale characterization work done on aged LIBs has shown that the degradation of transition metal oxides occurs mainly on the surface or subsurface, forming localized spinel or rock salt phases.<sup>99</sup> Therefore, total destruction and recovery of the bulk cathode are not necessary. Recent reports on direct re-lithiation of spent layered oxides ( $\text{LiCoO}_2$ , NMC532) via solution, solid state and molten salt infusion methods provide promising approaches for cathode direct regeneration.<sup>100-101</sup> As an end-of-life lithium metal ASSB would be fully depleted of lithium, or contain only traces of unconsumed lithium (Figure 1.8b), recycling strategies can be centered around processing the SSE and surface degraded cathodes. Although cathode coating materials used in ASSBs such as  $\text{LiNbO}_3$  would remain on the surface of cathodes, direct regeneration using re-lithiation methods can be done together with these ionically conductive coating layers that facilitate  $\text{Li}^+$  diffusion. This eliminates the need to break down either the protective coating layers or bulk cathode into precursors forms. Once the correct stoichiometric ratio of lithium and

transition metals are achieved, annealing can be done to reach the target crystal structure and removal of any remaining impurities. While existing studies on SSE solution processing and cathode direct regeneration have demonstrated the technical feasibility of recycling an end-of-life ASSB, this has yet to be tested in a full-cell pack. However, the proposed recycling model here may provide potential ASSB manufacturers new strategies for future sustainable battery designs, lowering financial burdens of manufacturing environmentally friendly commercialized ASSBs without compromising energy density and overall cell performance.

## 1.6 Conclusions

The continued pursuit of sustainable energy storage technologies with increasing energy density and safety demands will compel an inevitable shift from conventional LIBs to ASSBs. Developing a single type of SSE capable of meeting all required properties remain challenging, but the combination of materials and nano-engineering show great promise toward overcoming obstacles such as interfacial stability by controlling the thermodynamics and kinetics of SSE decomposition. We have highlighted the state-of-the-art characterization techniques to shed light onto the nano-scale phenomena within buried SSE interfaces and have proposed methods for *in-situ* observation of unstable solid-solid interfaces. We have also discussed polymer-SSE composites, solvent-polymer combination selection criteria, and methods to reduce resistive effects of binders. The aim is to accelerate commercialization of ASSBs using scalable solution-based processes. Finally, we have introduced strategies for sustainable ASSBs recycling, and proposed a fully recyclable ASSB model that can potentially lower costs of battery recycling with safer and simpler methods compared to current technologies. Nanotechnology itself may not be an all-encompassing silver bullet for every challenge faced by ASSBs, however it is certainly becoming an enabler for deeper understanding of nanoscale phenomena, helping better design strategies that can translate into improvements in materials and cell level performance.



The thesis abstract & Chapter 1, in part, is a reprint of the material “From nanoscale interface characterization to sustainable energy storage using all-solid-state batteries” as it appears in Nature Nanotechnology. Tan, D. H. S.; Banerjee, A.; Chen, Z.; Meng, Y. S. 2020, 15 (3), 170-180. The dissertation author was the first author of this paper, all authors contributed to this work.

## Chapter 2. Elucidating Reversible Redox of Sulfide $\text{Li}_6\text{PS}_5\text{Cl}$

Sulfide-based SSEs are promising candidates for ASSBs due to their high ionic conductivity and ease of processability. However, their narrow electrochemical stability window causes undesirable electrolyte decomposition. Existing literature on Li-ion ASSBs report an irreversible nature of such decompositions, while Li-S ASSBs show evidence of some reversibility. Here, we explain these observations by investigating the redox mechanism of argyrodite  $\text{Li}_6\text{PS}_5\text{Cl}$  at various chemical potentials. Various characterization tools and unique cell setups were adopted to characterize these phenomena. We found that Li-In |  $\text{Li}_6\text{PS}_5\text{Cl}$  |  $\text{Li}_6\text{PS}_5\text{Cl}$ -C half-cells can be cycled reversibly delivering capacities of  $965 \text{ mAh g}^{-1}$  for the electrolyte itself. During charging,  $\text{Li}_6\text{PS}_5\text{Cl}$  forms oxidized products of sulfur (S) and phosphorus pentasulfide ( $\text{P}_2\text{S}_5$ ) while during discharge, these products are first reduced to  $\text{Li}_3\text{PS}_4$  intermediate before forming lithium sulfide ( $\text{Li}_2\text{S}$ ) and lithium phosphide ( $\text{Li}_3\text{P}$ ). Finally, we quantified the relative contributions of the products towards cell impedance and proposed a strategy to reduce electrolyte decomposition and increase cell coulombic efficiency. Through this work we highlight the importance of redox kinetics in controlling interfacial stability of sulfide SSEs against electrodes in ASSBs.

### 2.1 Introduction

In the introduction, we established how ASSBs show great promise to become the next-generation energy storage technology. Compared to conventional liquid electrolyte-based batteries, ASSBs utilizes non-flammable SSEs, which translate to improved safety and the ability to operate over a wider temperature range.<sup>102-103</sup> Amongst these electrolytes, argyrodite  $\text{Li}_6\text{PS}_5\text{Cl}$  has attracted much attention due to its high ionic conductivity ( $> 1 \text{ mS cm}^{-1}$  at 298 K), ease of material synthesis and low temperature processability, which are critical requirements for scalable fabrication of ASSBs.<sup>14, 104-106</sup> It is also a relatively well studied electrolyte material with detailed experimental literature on its synthesis parameters, crystalline structure and mechanical

properties.<sup>14, 104-106</sup> However, its electrochemical interface and respective decomposition products against electrodes are not as well investigated. Although existing literature on sulfide electrolyte-electrode interface focuses on the chemical reactions against lithium metal anode or layered oxide cathodes<sup>105, 107-109</sup>, knowledge of its intrinsic interfacial electrochemical properties crucial for designing sulfide-based ASSBs remain lacking.

Like most sulfide-based SSEs,  $\text{Li}_6\text{PS}_5\text{Cl}$  has a relatively narrow electrochemical stability window, causing it to decompose during cell cycling to form unwanted interfacial oxidation or reduction products.<sup>17, 110-111</sup> While these oxidation and reduction products have not been fully identified experimentally due to its amorphous and buried nature, they have been predicted by computational density functional theory (DFT) studies done on common SSEs (e.g.,  $\text{Li}_{10}\text{GeP}_2\text{S}_{12}$ ,  $\text{Li}_7\text{P}_3\text{S}_{11}$ ,  $\text{Li}_3\text{PS}_4$ ,  $\text{Li}_6\text{PS}_5\text{Cl}$ ).<sup>17, 112</sup> Despite its ability to form passivating interfaces enabling their use in ASSBs without forming electronic pathways that short the cell, their interfacial properties are still unfavorable for cell performance due to large impedance growth and poor 1<sup>st</sup> cycle columbic efficiencies.<sup>113</sup> Current reports on sulfide-based Li-ion ASSBs show an irreversible SSE decomposition forming on the interface during the 1<sup>st</sup> charge.<sup>114</sup> However, recent studies have suggested the reversible nature of this decomposition, giving rise to high specific cell capacities.<sup>55, 105-106, 115-116</sup> This electrolyte decomposition-derived capacity is commonly seen in solid-state Li-S battery reports using sulfide-based SSEs, where capacities higher than the cathode's theoretical capacities of  $\text{Li}_2\text{S}$  and S were previously reported (Figure 2.1a). The extra reversible capacity likely arises as result of contributions from reversible electrolyte decomposition beyond the 1<sup>st</sup> cycle, as both Li-S and sulfide-based SSE redox ( $\text{S} / \text{S}^{2-}$ ) occur simultaneously during cycling over the same voltage range. A summary of capacities for Li-S ASSBs in literature is illustrated in Figure 2.1a.

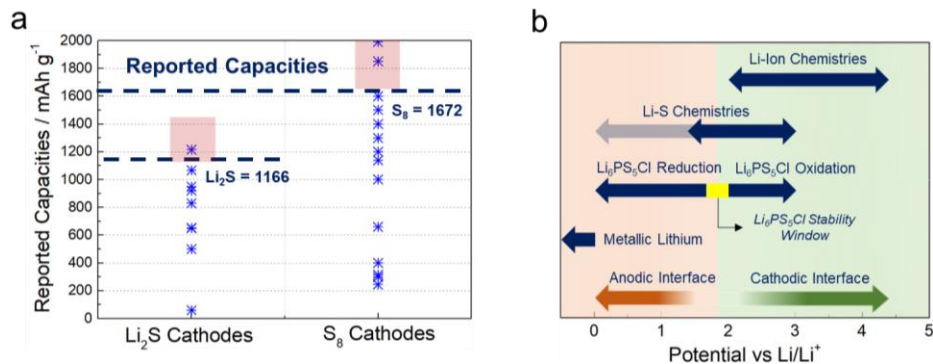


**Figure 2.1.** (a) Reported 1<sup>st</sup> cycle discharge capacities of representative solid-state Li-S batteries in literature.<sup>106, 116-141</sup> Dotted lines represent theoretical capacity of Li<sub>2</sub>S and S respectively. (b) Illustration of electrochemical operating windows for Li<sub>6</sub>PS<sub>5</sub>Cl, Li-S and Li-ion chemistries.

The reversible / irreversible observations made in these reports can be rationalized by comparing the operating voltage ranges of batteries used (Figure 2.1b). Comparing typical voltage ranges used in Li-ion and Li-S batteries against redox potentials of sulfide electrolytes such as Li<sub>6</sub>PS<sub>5</sub>Cl, it becomes clear that oxidative decomposition seen in Li-ion ASSBs would be perceived as irreversible. Likewise, oxidative and reductive decomposition of SSEs in ASSBs with lower voltage operating voltage such as Li-S batteries would be reversible and detected by extra capacities reported from the S or Li<sub>2</sub>S cathodes respectively. However, since both SSE decomposition and Li-S redox occur at overlapping voltage windows, it is hard to characterize and deconvolute capacity contributions from each component respectively. Furthermore, there is poor understanding of redox mechanism of Li<sub>6</sub>PS<sub>5</sub>Cl electrolyte alone, with studies mainly investigating its 1<sup>st</sup> cycle oxidation against layered oxide electrodes, or its chemical reactions against metallic lithium. Thus, it is vital to investigate the intrinsic electrochemical decomposition of Li<sub>6</sub>PS<sub>5</sub>Cl itself and its reversibility at typical cathode and anode potentials, without any contributions from the active electrodes.

Here, we use various characterization tools to experimentally observe the decomposition redox of Li<sub>6</sub>PS<sub>5</sub>Cl and propose a reaction pathway that helps shed light on its capacity contribution. The decomposition products at various potentials are identified and cell level properties are evaluated by isolating species at the anode and cathode interface respectively to quantify their

relative contributions to cell impedance. Finally, we demonstrate a method to reduce electrolyte decomposition in ASSBs and demonstrate its effectiveness in a typical Li-In | Li<sub>6</sub>PS<sub>5</sub>Cl | NCM811 cell. This study is fundamentally important to analyze thermodynamically driven interface product formation at electrodes of ASSBs and inform strategies for interfacial engineering and cell design.

## 2.2 Methods

Due to the sensitivity of the precursor compounds and the SSEs to water and air, all synthesis and electrochemical testing steps took place in an Ar-filled glovebox (MBraun MB 200B, H<sub>2</sub>O < 0.5 ppm, O<sub>2</sub> < 1.0 ppm) unless otherwise specified.

### 2.2.1 Materials Preparation of SSE-Carbon & Counter Electrodes

Commercial Li<sub>6</sub>PS<sub>5</sub>Cl was obtained from NEI Corporation and used as received. XRD and Raman was conducted on the commercial sample to ensure phase purity before use. The Li<sub>6</sub>PS<sub>5</sub>Cl-C electrode composite was prepared by ball milling Li<sub>6</sub>PS<sub>5</sub>Cl at 70 wt.% and carbon black (STREM Chemicals) at 30 wt.% in a 45 ml ZrO<sub>2</sub> ball mill jar (Emax, Retsch) sealed in Ar gas. Ball milling was conducted for 2 hours at room temperature and at 300 rpm. The extracted composite was grinded in an agate mortar and pestle for 5 minutes before use. To prepare the Li-In anode, stabilized lithium metal powder (FMC Lithium) was mixed with indium powder (Sigma Aldrich) in a glass vial using a vortex mixer for about 5 minutes. VGCF was obtained from Sigma Aldrich (Graphitized, Iron-free). (1)

### 2.2.2 Materials Characterization of Pristine and Cycles SSE-Carbon

XRD was conducted using Cu K $\alpha$  radiation ( $\lambda=1.54178$ ) over a  $2\theta$  range of 5-70° with a step size of 0.01°. ICSD database was used to reference the identified peaks of Li<sub>2</sub>S and Li<sub>6</sub>PS<sub>5</sub>Cl. A Perkin Elmer Raman Station 400F Spectrometer was used to collect Raman spectra intensity values from 134 to 1500 cm<sup>-1</sup>. The AXIS Supra XPS by Kratos Analytical was used to study the SSE redox products after cell cycling at various voltages. Binding energies of the mixtures in the

phosphorus, sulfur and chlorine regions were examined against pristine  $\text{Li}_6\text{PS}_5\text{Cl}$ . The XPS spectra were collected using an emission current of 5 mA and over an area of  $700\ \mu\text{m} \times 300\ \mu\text{m}$ . The spectra were analyzed using CasaXPS software. As sulfide-based materials are sensitive to air and moisture, decomposing to form toxic gases such as  $\text{H}_2\text{S}$ , all synthesis and testing steps are done within an Argon-filled glovebox (MBraun MB 200B,  $\text{H}_2\text{O} < 0.5\ \text{ppm}$ ,  $\text{O}_2 < 5.0\ \text{ppm}$ ). NMR reference materials  $\text{Li}_6\text{PS}_5\text{Cl}$  (NEI),  $\text{Li}_3\text{PS}_4$  (NEI) and  $\text{LiCl}$  (Sigma Aldrich) were obtained commercially. Solid-state  $^{31}\text{P}$  MAS NMR single pulse experiments were conducted on a 400 MHz Bruker Avance III spectrometer operating at 161.87 MHz. All samples were handled within a  $\text{N}_2$  glovebox and subsequently loaded into 4mm pencil-type  $\text{ZrO}_2$  rotors with o-ring caps to prevent contamination with moisture during the NMR experiments. The samples were spun at 9.8 kHz and the signal was collected using a  $4.5\ \mu\text{s}$   $\pi/2$  pulse, a recycle delay of 120s, and 48 transients. The  $^{31}\text{P}$  chemical shift was externally referenced to the isotropic chemical shift of hydroxyapatite ( $\delta_{\text{iso}} = 2.65\ \text{ppm}$ ). The  $^7\text{Li}$  and  $^6\text{Li}$  MAS NMR experiments were also carried out as single pulse experiments on the same spectrometer operating at 155.40 and 58.84 MHz, respectively. For the  $^{6,7}\text{Li}$  experiments, the samples were spun at 8 kHz (5.8 kHz) and the signal was collected using a  $5.25\ \mu\text{s}$   $\pi/2$  pulse, a recycle delay of 1.2 s (60 s), and 16 transients. The  $^{6,7}\text{Li}$  chemical shifts were externally referenced to the isotropic chemical shift  $\delta_{\text{iso}}$  of 1M  $\text{LiCl}$  (aq) ( $\delta_{\text{iso}} = 0\ \text{ppm}$ ).

### 2.2.3 Electrochemical Evaluation of SSE & Half Cells

EIS and CV measurements were performed with a Solartron 1260 impedance analyzer for the pristine SSE, cycled  $\text{Li-In} | \text{Li}_6\text{PS}_5\text{Cl} | \text{Li}_6\text{PS}_5\text{Cl-C}$  half-cells and  $\text{Li-In} | \text{Li}_6\text{PS}_5\text{Cl} | \text{NCM811}$  cells. In a typical cell, 100 mg of  $\text{Li-In}$  powder, 75 mg of  $\text{Li}_6\text{PS}_5\text{Cl}$ , 7 mg of cathode composite was used. Applied AC potential of 30 mV over a frequency range from 1 MHz to 0.1 Hz was used for the EIS measurement. The measurements were conducted at room temperature using two titanium blocking electrodes enclosed by a PEEK holder. For cell cycling, electrolyte and electrode

powders were first pressed at 370 MPa between the titanium plungers before being cycled using Neware Battery cyler and analyzed with BTS9000 software.

## 2.3 Results and Discussion

### 2.3.1 Electrochemical Redox of $\text{Li}_6\text{PS}_5\text{Cl}$

To investigate the reversible decomposition redox of  $\text{Li}_6\text{PS}_5\text{Cl}$ , a half cell setup was used with Li-In as the anode and carbon black (CB) (30 wt.%) mixed with  $\text{Li}_6\text{PS}_5\text{Cl}$  (70 wt.%) on the cathode. Cyclic voltammetry (CV) was performed on the Li-In |  $\text{Li}_6\text{PS}_5\text{Cl}$  |  $\text{Li}_6\text{PS}_5\text{Cl}$ -C cell (Figure 2.2a). Starting at open circuit voltage (OCV), a positive sweep yielded two oxidative peaks (1, 2) at 2.6 V and 3.0 V, while the negative sweep showed two reductive peaks (3, 4) at 2.0 V and 1.1 V respectively. During the second cycle, the first oxidative peak (1') appeared more intense, which is associated with a higher charging capacity, followed by a smaller oxidative peak (2'). There is a slight shift of the 1<sup>st</sup> reductive peak (3') to lower voltage, indicating changes in cell polarisation after oxidation. These observations were also validated with galvanostatic cell cycling (Figure 2.2b), where increased charge capacity and lowered discharge voltage at the 2<sup>nd</sup> cycle were found.

From Figure 2.2b, the first galvanostatic charge / discharge cycles of the  $\text{Li}_6\text{PS}_5\text{Cl}$ -C electrode yielded a large capacity of 354 mAh g<sup>-1</sup> and 968 mAh g<sup>-1</sup> respectively, while the second cycle yielded 956 mAh g<sup>-1</sup> and 1002 mAh g<sup>-1</sup> respectively. The first charge voltage plateau starts at the oxidation potential of 2 V, which agrees with DFT calculations in the literature.<sup>17</sup> This oxidation potential has also been reported in work studying sulfide decomposition in Li-ion ASSBs.<sup>113</sup> Interestingly, a typical discharge cycle (Figure 2.2b) displays two plateaus, one between 2.2 V to 1.3 V and a second between 1.3 V and 0 V, corresponding to the two reductive peaks in Figure 2.2a. This indicates two distinct thermodynamically reduction reactions at each respective voltage. Such double discharge plateau has not been observed in previous literature

on either sulfide SSE redox studies,<sup>55, 110, 142</sup> or Li-S batteries work using sulfide SSEs<sup>106, 130</sup> for reasons that will be discussed later.

### Theoretical Capacity of Li<sub>6</sub>PS<sub>5</sub>Cl Oxidation / Reduction

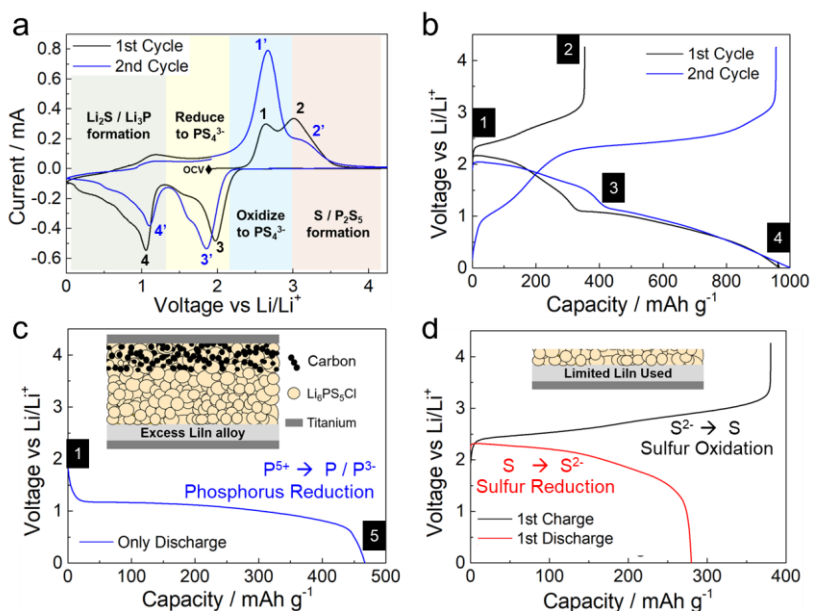
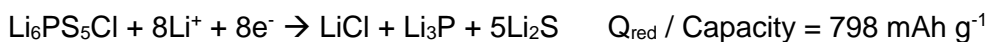
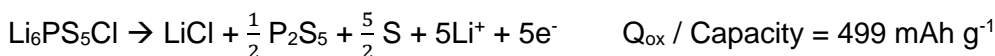


**Figure 2.2.** (a) Cyclic voltammograms for the first two cycles, voltage was swept between 0 - 4.2 V (vs Li/Li<sup>+</sup>) at 100 μV s<sup>-1</sup> starting from OCV. (b) 1<sup>st</sup> and 2<sup>nd</sup> voltage profiles of Li-In | Li<sub>6</sub>PS<sub>5</sub>Cl | Li<sub>6</sub>PS<sub>5</sub>Cl-C half cell. Cycling was done between 0 to 4.2 V (vs Li/Li<sup>+</sup>) at room temperature and a current density of 0.25 mA cm<sup>-2</sup>. (c) 1<sup>st</sup> Direct discharge curve showing 1 voltage plateau at 1.0 V for excess Li<sup>+</sup> source, indicating phosphorus species reduction. (d) 1<sup>st</sup> charge and discharge curves showing 1 voltage plateau at 2.0 V for limited Li<sup>+</sup> source, indicating sulfur species redox. Marked Numbers 1 to 5 represent potentials where Li<sub>6</sub>PS<sub>5</sub>Cl was extracted for characterization.

To understand this phenomenon, we hypothesize that after complete oxidation of the Li<sub>6</sub>PS<sub>5</sub>Cl-C electrode during the first charge, the first discharge plateau is attributed to sulfur species reduction (S → S<sup>2-</sup>) and the second plateau is attributed to phosphorus species reduction (P<sup>5+</sup> → P / P<sup>3-</sup>), as the only species remaining to be reduced is phosphorus. This hypothesis can be verified by directly discharging the Li-In | Li<sub>6</sub>PS<sub>5</sub>Cl | Li<sub>6</sub>PS<sub>5</sub>Cl-C cell from OCV as seen in Figure 2.2c. As the cell at OCV comprises of sulfur in its reduced state (S<sup>2-</sup>) in Li<sub>6</sub>PS<sub>5</sub>Cl, directly



discharging the cell will cause reduction of phosphorus species, as seen in the single discharge plateau at voltages below 1.3 V. Based on the previous computational predictions,  $\text{Li}_6\text{PS}_5\text{Cl}$  reduction will result in the formation of Li-containing products such as  $\text{Li}_3\text{P}$ ,  $\text{Li}_2\text{S}$  and  $\text{LiCl}$ .<sup>17</sup> To further test this hypothesis, we limit the reaction of phosphorus species, by using a minimal amount of Li-In at the anode (Figure 2.2d). As the reduction of phosphorus species in  $\text{Li}_6\text{PS}_5\text{Cl}$  requires extra Li source to form the respective Li containing products (e.g.,  $\text{Li}_3\text{P}$ ), these reactions cannot occur if all the Li at the anode are fully consumed. As such, after being fully charged, only one discharge plateau attributed to sulfur redox was seen between 1.3-2.2 V. The galvanostatic data as well as the cyclic voltammogram provides an indication on the SSE redox mechanism, and the respective sulfur and phosphorus reaction potentials vs  $\text{Li}/\text{Li}^+$ . To support these findings, multiple characterization tools are utilized, and its results are discussed.

### **2.3.2 XPS of $\text{Li}_6\text{PS}_5\text{Cl}$ at various potentials**

To verify specific products of each sulfur or phosphorus species, XPS was conducted at each stage of charge (numbered 1 to 5 in Figure 2.3) for the S 2p, P 2p, and Cl 2p regions. Cycling profiles from Figure 2.2a are plotted vertically for ease of reference. At the pristine state,  $\text{Li}_6\text{PS}_5\text{Cl}$  comprises of  $\text{PS}_4^{3-}$  thiophosphate units which can be detected by the characteristic doublet peaks around 161.5 eV in the S 2p region and 131.5 eV in the P 2p region. This was described as terminal S bonds in some literature.<sup>105, 111</sup> No signals from other components are found in the pristine electrolyte. Upon full charge of the Li-In |  $\text{Li}_6\text{PS}_5\text{Cl}$  |  $\text{Li}_6\text{PS}_5\text{Cl}$ -C cell to 4.2 V,  $\text{Li}_6\text{PS}_5\text{Cl}$  decomposes to form oxidised products of elemental S (Figure 2.3a-2) and  $\text{P}_2\text{S}_5$  (Figure 2.3b-2). These findings agree with existing literature studies on the oxidation behaviour of sulfide SSE,<sup>115</sup> as well as computational studies showing  $\text{Li}_6\text{PS}_5\text{Cl}$  first forming  $\text{LiCl}$  and  $\text{Li}_3\text{PS}_4$ , followed by S and  $\text{P}_2\text{S}_5$  upon further oxidation.<sup>17</sup>

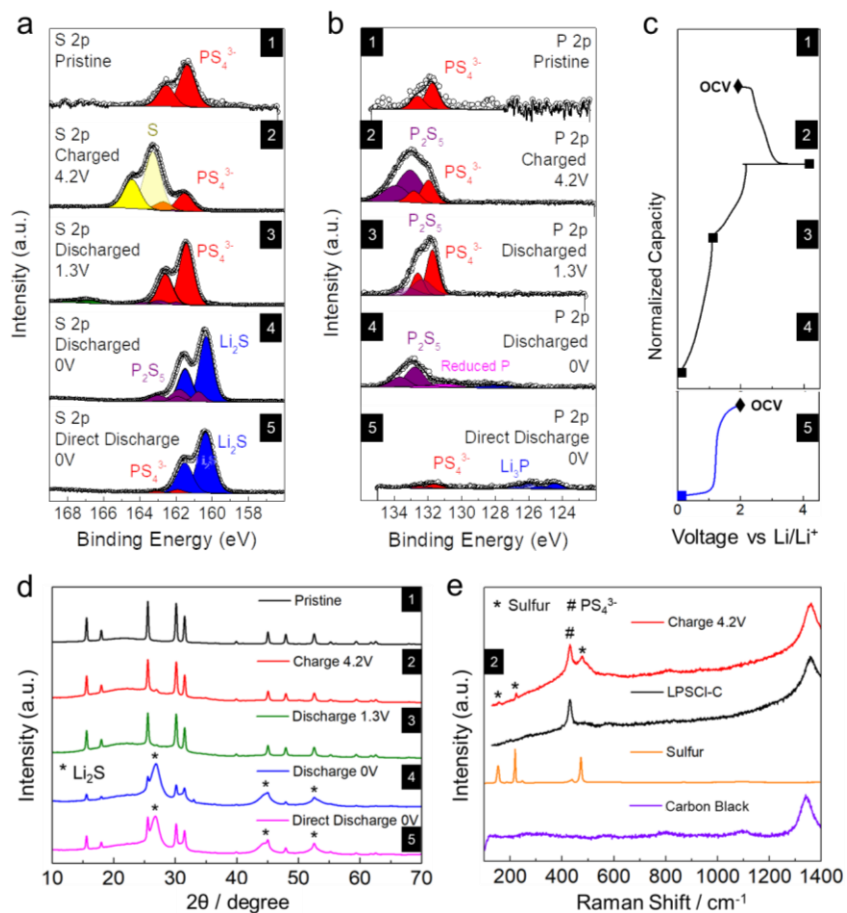


**Figure 2.3.** XPS spectra showing the binding energies of  $\text{Li}_6\text{PS}_5\text{Cl}$  at different cycling potentials. (a) Sulfur 2p region. (b) Phosphorus 2p region. (c) Cycling voltage profile for reference. (d) XRD patterns at different cycling potentials.  $\text{Li}_2\text{S}$  can be identified as reduced product. (e) Raman Spectra at fully charged state. Sulfur is identified as an oxidized product. Raman Spectra from pristine cathode, sulfur and CB are displayed for reference.

Upon discharge of the cell until 1.3 V (Figure 2.3c-3), a decrease in peak intensities for S and  $\text{P}_2\text{S}_5$  and relative intensity increase of  $\text{PS}_4^{3-}$  thiophosphate characteristic energies are observed. This indicates a reformation of  $\text{PS}_4^{3-}$  unit during cell discharge after oxidative decomposition of the pristine electrolyte. While its configuration and structural properties cannot be determined from XPS alone, it clearly suggests that  $\text{Li}_2\text{S}$  has not yet been formed after the first discharge plateau. Some residual signal is detected from unreacted  $\text{P}_2\text{S}_5$  (Figure 2.3b-3). As it is believed to have poor reaction kinetics, some  $\text{P}_2\text{S}_5$  remains as partially irreversible products of  $\text{Li}_6\text{PS}_5\text{Cl}$  oxidation. Upon further discharge to 0 V, strong signals of  $\text{Li}_2\text{S}$  around 160 eV in Figure 2.3a-4 are observed, while weak signals of reduced phosphorus species and  $\text{Li}_3\text{P}$  are detected

along with unreacted residual  $P_2S_5$  in Figure 2.3b-4. It is worthy to note that due to the low stoichiometric ratio of P to S atoms in  $Li_6PS_5Cl$ , signals from P 2p are weaker in relative intensity and difficult to detect. To verify that signals from  $P_2S_5$  are attributed to oxidative species formed by charging to 4.2 V, another cell was prepared and directly discharged to 0 V from OCV (Figure 2.3c-5). As expected, no signals of  $P_2S_5$  are detected and only  $Li_2S$ , reduced P and  $Li_3P$  are found (Figure 2.3b-5).

Two important observations can be made from the XPS study. (1) The decomposed product species at the oxidized state of 4.2 V and reduced state at 0 V represent the typical interfacial products of Li-ion ASSBs when  $Li_6PS_5Cl$  is used as the electrolyte. The half-cell setup used in this XPS study allows us to electrochemically form the thermodynamically driven interface products at typical voltages of oxide-based cathodes such as  $LiCoO_2$  and anodes such as graphite, isolating any effects from the electrode material. (2) This study also demonstrates the reversibility of the electrolyte decomposition, where reformation of  $PS_4^{3-}$  units from elemental S and  $P_2S_5$  acts as an intermediate redox product before formation of  $Li_2S$  when phosphorus is reduced at lower voltages.

### 2.3.3 XRD & Raman of $Li_6PS_5Cl$ at various potentials

To substantiate these findings, X-ray diffraction (XRD) was conducted for the  $Li_6PS_5Cl$ -C cathode at similar cycling potentials (Figure 2.3d). At pristine states, diffraction peaks are observed at the characteristic Bragg angles of crystalline  $Li_6PS_5Cl$  as seen in previous studies.<sup>14, 104, 106</sup> Unfortunately, there are little significant changes observed upon cell charging, due to the poor symmetry and amorphous nature of oxidized S and  $P_2S_5$  products, as reflected by an increased intensity of the amorphous bump between 20-30° at the 2θ. While any LiCl formed should be crystalline, its relative amounts are too low to be detected and it is likely to be deposited as nano-sized crystals as the SSE was pulverized during ball milling. Only signals from unreacted crystalline  $Li_6PS_5Cl$  can be detected. Likewise, the cell discharged to 1.3 V displays no significant

change in diffraction patterns. However, the presence of oxidised elemental S can be detected clearly with Raman as seen in Figure 2.3e. The charged  $\text{Li}_6\text{PS}_5\text{Cl}$ -C cathode at 4.2 V vs.  $\text{Li}/\text{Li}^+$  display signals from oxidized S at  $155\text{ cm}^{-1}$ ,  $220\text{ cm}^{-1}$  and  $475\text{ cm}^{-1}$ , electrolyte  $\text{PS}_4^{3-}$  at  $430\text{ cm}^{-1}$ , as well as the D-band from CB at  $1350\text{ cm}^{-1}$ . Upon further discharge to 0V, the relative intensities of  $\text{Li}_6\text{PS}_5\text{Cl}$  diffraction peaks start to decrease. As phosphorus reduction in the electrolyte occurs, nanocrystalline  $\text{Li}_2\text{S}$  begins to form and is reflected as broad peaks seen around  $26^\circ$ ,  $45^\circ$  and  $52^\circ$  at the  $2\theta$  (Figure 2.3d). A similar trend is observed for the cell that is directly discharged from OCV. These findings are consistent with the XPS analysis discussed earlier, where elemental S is formed as a result of SSE oxidation during charging,  $\text{Li}_2\text{S}$  formation is not observed during discharge until low voltages, where phosphorus reduction occurs. Figure 2.4a illustrates the proposed reaction pathway of  $\text{Li}_6\text{PS}_5\text{Cl}$  reversible electrochemical redox based on the analysis discussed.

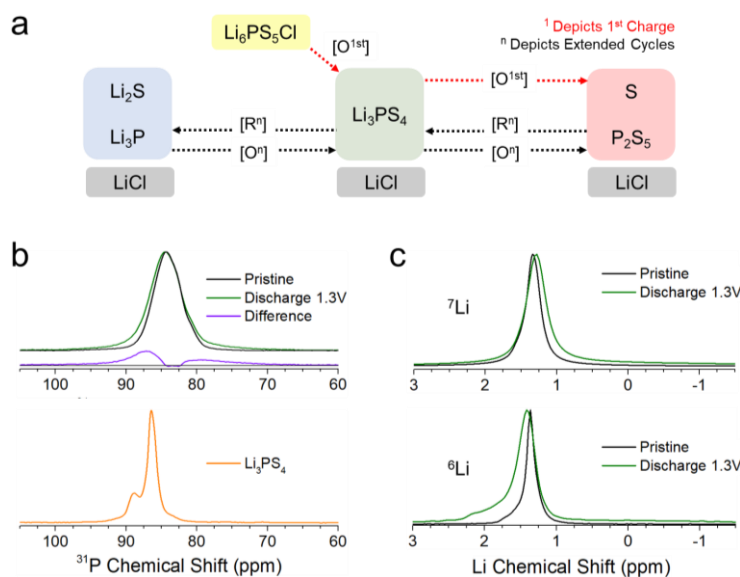


**Figure 2.4.** (a) Redox reaction pathway of  $\text{Li}_6\text{PS}_5\text{Cl}$  for the 1<sup>st</sup> charge and subsequent cycles. (b) (Top)  $^{31}\text{P}$  MAS NMR spectra of pristine and mid-discharged  $\text{Li}_6\text{PS}_5\text{Cl}$ . (Bottom)  $^{31}\text{P}$  MAS NMR spectrum of reference  $\text{Li}_3\text{PS}_4$  containing both  $\gamma$  and  $\beta$  phases. (c) (Top)  $^7\text{Li}$  MAS NMR spectra of pristine and mid-discharged  $\text{Li}_6\text{PS}_5\text{Cl}$ . (Bottom)  $^6\text{Li}$  MAS NMR spectrum revealing the rise of broad peak centered at 0.81 ppm. Expanded chemical shift ranges can be found in SI.

### 2.3.4 Solid-state nuclear magnetic resonance (NMR) at mid-discharged state

To further characterize the nature of products at mid-discharge,  $^6\text{Li}$ ,  $^7\text{Li}$ , and  $^{31}\text{P}$  MAS NMR was conducted by comparing pristine  $\text{Li}_6\text{PS}_5\text{Cl}$  to the mid-discharged state at 1.3V.  $^{31}\text{P}$  NMR spectra of the pristine and mid-discharged  $\text{Li}_6\text{PS}_5\text{Cl}$  material are shown in Figure 2.4b. The  $^{31}\text{P}$  spectra of the pristine  $\text{Li}_6\text{PS}_5\text{Cl}$  is typical of that previously shown in literature,<sup>143-144</sup> with broad features centered at  $\delta = 84.3$  ppm and two low frequency shoulders ( $\delta = 82.7$  and  $81.0$  ppm). The broadened features are caused by disorders on the anion sublattice from the substitutional mixing of Cl and S atoms on their respective crystallographic sites around the phosphorous  $\text{PS}_4^{3-}$  tetrahedron.<sup>144</sup> The  $^{31}\text{P}$  spectrum of the mid-discharged  $\text{Li}_6\text{PS}_5\text{Cl}$  cathode bears the same broadened features as the pristine material with additional broadening at the tails. This difference is attributed to additional high frequency broadening centered around  $\delta = 87$  ppm, which falls in between the isotropic chemical shifts observed in crystalline  $\gamma\text{-Li}_3\text{PS}_4$  (88.4 ppm) and  $\beta\text{-Li}_3\text{PS}_4$  (86.53 ppm) phases.<sup>145-147</sup> This suggests the formation of isolated  $\text{PS}_4^{3-}$  tetrahedra with chemical environments more similar to those found in  $\text{Li}_3\text{PS}_4$  than  $\text{Li}_6\text{PS}_5\text{Cl}$ . The broadening at very high ( $> 90$  ppm) and low ( $< 82$  ppm) frequencies are a result of an overall increase in the amorphous content of various  $\text{PS}_4^{3-}$  and  $\text{P}_2\text{S}_7^{4-}$  units and covers a chemical shift distribution typical of Li rich thiophosphate glasses.<sup>148</sup> The additional broadening observed after cycling suggests the increased presence of distorted  $\text{PS}_4^{3-}$  tetrahedra similar to that observed in  $\text{Li}_3\text{PS}_4$  as well as a more heavily disordered thiophosphate network forming. Assigning definitive isotropic chemical shifts is challenging due to the extremely broadened features resulting from not only a distribution of bond lengths and angles of the  $\text{PS}_4^{3-}$  tetrahedra but also as a result of substitutional mixing of S and Cl within the second and third coordination sphere of  $\text{Li}_6\text{PS}_5\text{Cl}$ . However, deconvolution is performed to demonstrate an example of the rise of the distorted  $\text{Li}_3\text{PS}_4$  and amorphous lithium thiophosphate components after cycling. Evidence of residual  $\text{Li}_2\text{S}$  and  $\text{LiCl}$  after charge cycling

is also found in  $^{6,7}\text{Li}$  MAS NMR (Figure 2.4b). The  $^7\text{Li}$  spectrum of the pristine material displays a single motional narrowed Lorentzian peak centered at 1.33 ppm. After cycling, the  $^7\text{Li}$  spectrum displays a shift towards 1.2 ppm and a rise of a broad component between 0.5 and -2 ppm. These changes can be elucidated by comparison to the  $^7\text{Li}$  chemical shifts for the reference compounds,  $\text{Li}_3\text{PS}_4$  and  $\text{LiCl}$ .<sup>149</sup> The  $^7\text{Li}$  spectrum for  $\text{Li}_3\text{PS}_4$  displays two peaks at 0.98 ppm and 0.41 ppm while  $\text{LiCl}$  displays one peak at -0.99 ppm. The increased intensity of the cycled  $\text{Li}_6\text{PS}_5\text{Cl}$  within these regions indicates the formation of a minor amount of these two compounds. However, a general lack of distinguishable features outside of the primary  $\text{Li}_6\text{PS}_5\text{Cl}$  peak suggests that  $\text{Li}^+$  are exchanging within the chemical environments of these decomposed products. To obtain better resolution of these decomposed products, we turn to  $^6\text{Li}$  MAS NMR (Figure 2.4c) as it offers an increased sensitivity to changes in the local structure compared to  $^7\text{Li}$ . The relative difference of the primary  $\text{Li}_6\text{PS}_5\text{Cl}$  peak to the reference compounds,  $\text{Li}_3\text{PS}_4$  and  $\text{LiCl}$ , is nearly the same as seen in  $^7\text{Li}$ . Comparing the pristine and cycled  $\text{Li}_6\text{PS}_5\text{Cl}$  material reveals the rise of a shallow broad component similar to that observed in the  $^7\text{Li}$  spectrum. This broad component can be contributed to  $\text{Li}_3\text{PS}_4$  and  $\text{LiCl}$  based on similarity of their  $^6\text{Li}$  chemical shifts. The cycled  $\text{Li}_6\text{PS}_5\text{Cl}$  also shows a broadening towards higher chemical shift which was notably absent from the  $^7\text{Li}$  spectrum. This new feature is close to the chemical shift expected for  $\text{Li}_2\text{S}$  (2.35 ppm)<sup>150</sup> suggesting residual formation of  $\text{Li}_{2-x}\text{S}$ .

### 2.3.5 EIS of $\text{Li}_6\text{PS}_5\text{Cl}$ half-cell at various potentials

Next, we investigate the impact of  $\text{Li}_6\text{PS}_5\text{Cl}$  decomposition products on cell impedance in typical Li-ion ASSBs. To do so, we conduct electrochemical impedance spectroscopy (EIS) measurements across the  $\text{Li-In} \mid \text{Li}_6\text{PS}_5\text{Cl} \mid \text{Li}_6\text{PS}_5\text{Cl-C}$  cell at different cycling potentials (Figure 2.5). Considering that charge transfer resistances at the  $\text{Li-In}$  anode and of the bulk electrolyte do not change significantly, any changes in total cell impedance can be attributed to impedance growth or ionic conductivity changes in the  $\text{Li}_6\text{PS}_5\text{Cl-C}$  electrode as redox proceeds.

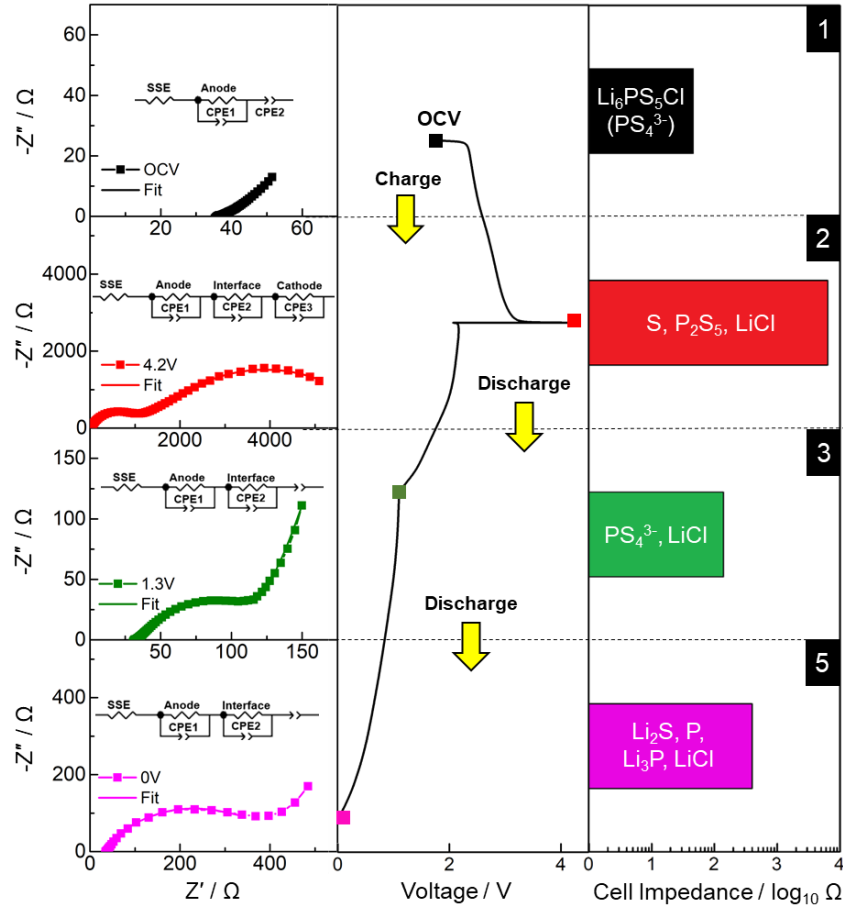


**Figure 2.5.** Nyquist plots at different cycling potentials showing the impedance changes of Li-In | LPSCI | LPSCI-C cell (left). Normalized capacity vs Voltage profiles are displayed for reference (middle). Bar graph shows relative differences in cell impedance at different oxidation or reduction states of  $\text{Li}_6\text{PS}_5\text{Cl-C}$  (right), direct discharge marked as 5 is used at full reduced state for fair comparison.

Nyquist plot of the pristine cell at OCV shows a total cell resistance of approximately 45  $\Omega$ , which translates into the expected  $\text{Li}_6\text{PS}_5\text{Cl}$  conductivity on the order of  $\sim 10^{-3} \text{ S cm}^{-1}$ . However, when the cell is charged, the total cell resistance increases by two orders of magnitude, as reflected in Figure 2.5 (left). This results from formation of highly insulating products of S and  $\text{P}_2\text{S}_5$ , dramatically increasing the charge transfer resistance in the cathode. However, when the cell is discharged to 1.3V, the total cell impedance falls to 139  $\Omega$  as seen in the bar chart of Figure 2.5 (right), regaining almost all the conductive properties of the electrolyte in the cathode. This is due to the reformation of conductive  $\text{Li}_3\text{PS}_4$  found in the previous section. It is likely that the impedance measured at 1.3V is higher than the pristine state due to incomplete reaction of the oxidised

products found in Figure 2.3b as well as contributions from LiCl formed during redox. Upon full discharge to 0V, the total cell impedance increases to 400  $\Omega$  (Figure 2.5) which is an increase of less than 1 order of magnitude compared to the pristine state. The large changes in impedances measured across the cell during cycling provides us an indication of the effects of SSE decomposition on ASSB cell performance.

#### **2.3.5.1 $\text{Li}_6\text{PS}_5\text{Cl}$ reductive decomposition.**

From these results, it can be inferred that impedance growth in ASSB full cells during cycling is largely attributed to oxidation decomposition of SSE at high voltages. By comparison, reduction decomposition of SSEs at anodes such as graphite contributes less to cell resistance. This likely results from the formation of  $\text{Li}_3\text{P}$ , which was previously reported to have some  $\text{Li}^+$  conductive properties.<sup>151-152</sup> Additionally, based on literature work studying Li-S chemistries,  $\text{Li}_2\text{S}$  at discharged states was found to have comparatively lower charge transfer resistances compared to elemental S at charged states when measured with similar impedance methods.<sup>153</sup> To further substantiate this, impedance growth of an anode composite comprising 60 wt% carbon graphite was measured before and after lithiation (Figure 2.6). As expected, impedance growth at the anode was still significantly less compared to the cathode composite comprising only 1wt% CB after charging. EIS measurements were also done on pure interfacial components prepared in their stoichiometric formation ratios. The results showed some ionic conductive properties of reduced species ( $\sim 10^{-6} \text{ S cm}^{-1}$ ), while the oxidized species were found to be entirely insulative (Figure 2.7).



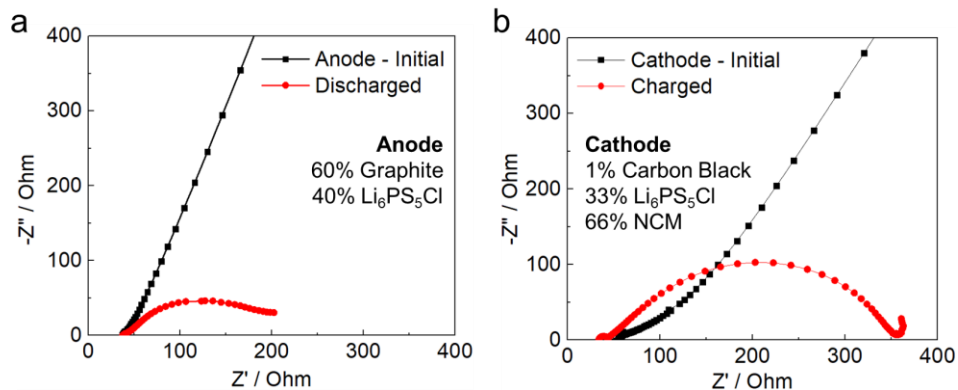


**Figure 2.6.** EIS measurements of impedance growth before and after: (a) 1<sup>st</sup> Discharge of anode with 60wt% Graphite. (b) 1<sup>st</sup> Charge of cathode NCM811 with 1wt% Carbon additive. Showing large impedance growth at cathode despite small amounts of carbon additive.

### 2.3.5.2 Li<sub>6</sub>PS<sub>5</sub>Cl oxidative decomposition.

While SSE decomposition brings about negative effects on electrode charge transfer resistance and overall cell impedance, its impact is more pronounced at the cathode where oxidative decomposition occurs. As such, strategies to mitigate SSE oxidative decomposition in ASSBs are vital. Although it is difficult to change the decomposition thermodynamics of sulfide-based SSEs, it is possible to control its kinetics by tuning the morphology or specific surface area of carbon used. With reduced surface area, the SSE would have less exposure to electronically conductive surfaces. Without sufficient electronic pathway for redox to occur, the kinetics of SSE decomposition can be significantly reduced.

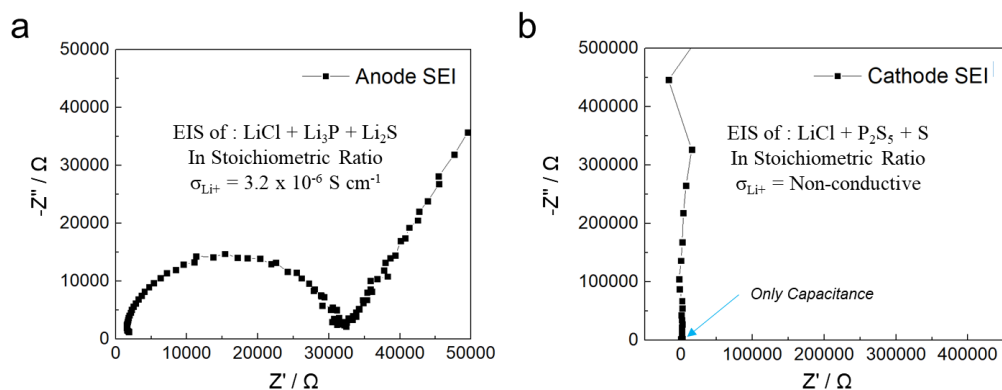


**Figure 2.7.** EIS measurements of pure interfacial products: (a) reduced species of LiCl, Li<sub>3</sub>P and Li<sub>2</sub>S. (b) oxidized species of LiCl, P<sub>2</sub>S<sub>5</sub> and S.

Due to its nanosized particles (Figure 2.8a), carbon black has a higher specific surface area ( $80 \text{ m}^2 \text{ g}^{-1}$ ) that promotes decomposition kinetics of SSEs compared to other types of carbon such as vapor-grown carbon fiber (VGCF) with lower surface area ( $24 \text{ m}^2 \text{ g}^{-1}$ ) (Figure 2.8b). Such differences were also detected with Raman, where VGCF exhibits significantly lowered D / G band ratios compared to CB.<sup>149</sup> Figure 2.6c illustrates the effect of using 30 wt.% of both types of carbon in the Li-In |  $\text{Li}_6\text{PS}_5\text{Cl}$  |  $\text{Li}_6\text{PS}_5\text{Cl}$ -C cell charged at  $0.25 \text{ mA cm}^{-2}$ . The cell using CB showed much higher decomposition capacity and faster decomposition kinetics compared to the cell using VGCF. The sharp vertical voltage line at the end of the plateau of SSE-CB composite also indicates a complete reaction of SSE in the composite, while the VGCF composite shows a higher polarization indicating decreased decomposition kinetics. The effect of using lower surface area carbon can also be seen in Figure 2.8d, which compared the 1<sup>st</sup> cycle cell voltage curves of a Li-In |  $\text{Li}_6\text{PS}_5\text{Cl}$  | NCM811 half-cell using 1 wt.% of each carbon type in the oxide cathode. The cell using VGCF carbon additive shows a reduced electrolyte decomposition profile offset (inset), as well as a higher 1<sup>st</sup> cycle coulombic efficiency compared to CB. Additionally, the discharge curve from the cell using VGCF also displays lower cell polarization. This results from lower cell impedance due to reduced SSE decomposition compared to the cell using CB.

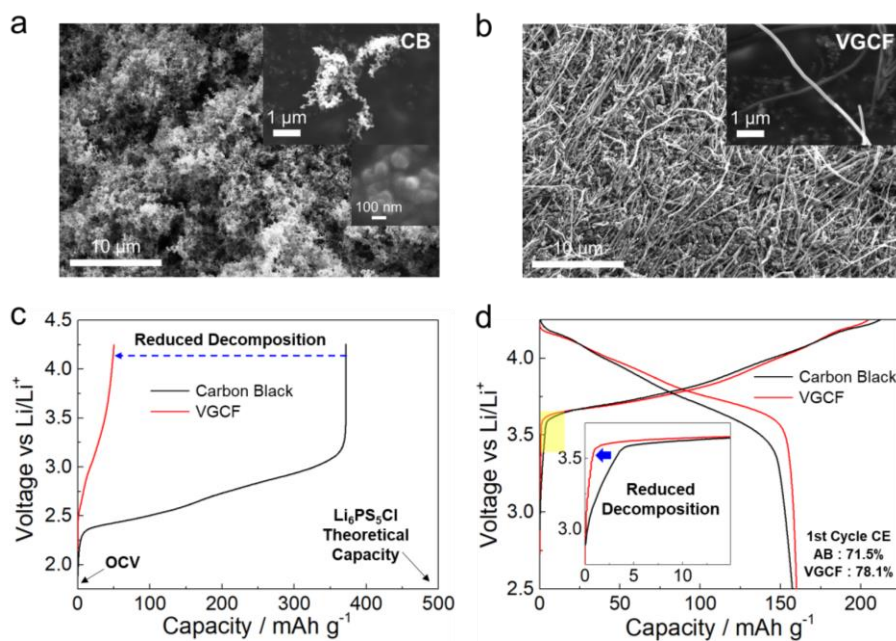


**Figure 2.8.** SEM images of: (a) carbon black (b) vapor grown carbon fibre showing differences in morphology and size. (c) Charge voltage profiles of Li-In | Li<sub>6</sub>PS<sub>5</sub>Cl | Li<sub>6</sub>PS<sub>5</sub>Cl-C cells using 30 wt% carbon black (surface area: ~ 80 m<sup>2</sup>/g) vs vapor grown carbon fibre (surface area: ~ 24 m<sup>2</sup>/g). (d) Charge & discharge voltage profiles of Li-In | Li<sub>6</sub>PS<sub>5</sub>Cl | NCM811 cells using 1 wt.% of carbon black vs vapor grown carbon fibre.

As such, scientific efforts to improve the performance of ASSBs such as widening of SSE's electrochemical stability window and/or reducing cell polarization growth over extended cycling can be directed toward reducing electrolyte oxidative decomposition. However, this is challenging to overcome, as the oxidative decomposition during the 1<sup>st</sup> charge is an unavoidable thermodynamic property of the electrolyte. Existing methods to apply surface coatings on the cathode particles can only reduce the interfacial reactions between the electrolyte and electrode but cannot prevent the formation of highly resistive oxidized SSE products. Current efforts to tackle this by controlling the decomposition kinetics should go beyond carbon optimization or using materials with lower specific surface area at the cathode, as carbon still plays an important role in capacity utilization of layered oxide cathodes. Other strategies are needed to either improve the intrinsic property of the SSE or further reduce its decomposition kinetics. New methods may include surface or bulk modification of SSE particles to improve their stability at

high voltage or developing better conductive networks to maintain electronic pathway between cathode particles with minimal exposure to the SSE.

## 2.4 Conclusion

In summary, this study elucidates the redox behaviour and the mechanisms of  $\text{Li}_6\text{PS}_5\text{Cl}$  solid electrolyte decomposition. We found that  $\text{Li}_6\text{PS}_5\text{Cl}$  decomposition is irreversible in Li-ion batteries due to the high voltage ranges used. When lower voltage cycling is done, large reversible capacities of  $965 \text{ mAh g}^{-1}$  from the electrolyte alone are observed. To investigate this reversible decomposition, XPS, XRD, Raman and NMR characterizations were conducted at various voltages of a Li-In |  $\text{Li}_6\text{PS}_5\text{Cl}$  |  $\text{Li}_6\text{PS}_5\text{Cl}$ -C cell, where its oxidation and reduction products were identified experimentally. It was found that oxidised products of elemental S and  $\text{P}_2\text{S}_5$  undergo an intermediate transition product of  $\text{Li}_3\text{PS}_4$  before being reduced to  $\text{Li}_2\text{S}$  and  $\text{Li}_3\text{P}$ . Subsequently, the impedance contributions of reductive and oxidative decomposition products were measured using EIS measurements. It was found that the cell impedance and polarisation growth in typical Li-ion ASSBs are a result of SSE decomposition at the cathode, where reductive SSE decomposition have less effects on overall cell impedance. Alternative types of low specific surface area carbon are proposed to reduce SSE decomposition, and its effect was demonstrated in a Li-In |  $\text{Li}_6\text{PS}_5\text{Cl}$  | NCM811 cell. The principles of SSE redox and its mechanism found in this study can be further extended toward new electrolyte material selection or modification, that mitigates SSE oxidation decomposition and thus improves cycle performance of ASSBs.

Chapter 2, in full, is a reprint of the material “Elucidating Reversible Electrochemical Redox of  $\text{Li}_6\text{PS}_5\text{Cl}$  Solid Electrolyte” as it appears in ACS Energy Letters. Tan, D. H. S.; Wu, E. A.; Nguyen, H.; Chen, Z.; Marple, M. A. T.; Doux, J.-M.; Wang, X.; Yang, H.; Banerjee, A.; Meng, Y. S. 2019, 2418-2427. The dissertation author was the first author of this paper, all authors contributed to this work.

### Chapter 3. Scalable Solution Processing for ASSBs Manufacturing

ASSBs have the potential to deliver higher energy densities, wider operating temperature range and improved safety compared with today's liquid electrolyte-based batteries. However, of the various major SSE classes: polymers, sulfides or oxides, none alone can deliver the combined properties of ionic conductivity, mechanical and chemical stability needed to address scalability and commercialization challenges. While promising strategies to overcome these include the use of polymer / oxide or sulfide composites. There is still a lack of fundamental understanding between different SSE-polymer-solvent systems and its selection criteria. Here, we isolate various SSE-polymer-solvent systems and study their molecular level interactions by combining various characterization tools. With these findings, we introduce a suitable  $\text{Li}_7\text{P}_3\text{S}_{11}$  SSE - SEBS polymer - xylene solvent combination that significantly reduces SSE thickness ( $\sim 50 \mu\text{m}$ ). The SSE-polymer composite displays high room temperature conductivity ( $0.7 \text{ mS cm}^{-1}$ ) and good stability with lithium metal by plating and stripping over 2000 hours at  $1.1 \text{ mAh cm}^{-2}$ . This study suggests the importance of understanding fundamental SSE-polymer-solvent interactions and provides a design strategy for scalable production of ASSBs.

#### 3.1 Introduction

Methods to produce conventional batteries on a large scale are well established, however due to the air/moisture sensitivities and poor mechanical properties of sulfide or oxide based electrolytes, it is challenging to adopt the conventional slurry casting assembly set-up for ASSBs manufacturing.<sup>72, 154</sup> In terms of energy density, ASSBs still remain inferior to conventional batteries due to the thick SSEs used to compensate poor mechanical properties in its pelletized form.<sup>155-156</sup> Most reports on ASSBs utilize sulfide or oxide electrolyte layers ranging from 0.6-1.2mm, vastly reducing the weight fraction of active materials in the cells, keeping their overall energy density low.<sup>103, 157-159</sup> The thickness of electrolyte layers needs to be reduced by at least an order of magnitude for ASSBs to compete with conventional batteries in terms of energy

density. Physical vapor deposition (PVD), pulsed laser deposition (PLD) and sputtering have been explored in some cases to fabricate SSE with reduced thicknesses,<sup>72, 103, 160</sup> but solvent based techniques such as solution casting used in conventional batteries remain most attractive from a manufacturing point of view. To address these limitations, using flexible composite solid electrolytes by combining inorganic Li<sup>+</sup> superionic conductors and polymers have been considered a promising approach. Recent reports of oxide-based composite electrolytes such as Li<sub>7</sub>La<sub>3</sub>Zr<sub>2</sub>O<sub>12</sub> (LLZO) with polyethylene oxide (PEO)<sup>40, 161</sup> and LiAlGePO<sub>4</sub> (LAGP) class ceramics with polyvinylidene fluoride (PVDF)<sup>162</sup> in ASSBs have generated interest for new types of composite electrolytes, relying on their mechanical flexibility and ability to form thin films with good electrochemical stability. Compared to their oxide-based counterparts, relatively few have reported the use of composite sulfide-polymer electrolytes to address cell energy density and processability problems, owing to their chemical instability.<sup>75, 162-166</sup> Amongst the literature on sulfides (Li<sub>6</sub>PS<sub>5</sub>Cl / Li<sub>3</sub>PS<sub>4</sub>) with polymers (acrylonitrile butadiene (NBR)/ polyvinylpyrrolidone (PVP)), promising electrochemical results on composite conductivity and cell performance have been reported.<sup>75, 165-166</sup> However, there is still a limited understanding of how sulfide electrolytes behave and how they interact with various functional moieties in both polymers and solvents. This knowledge is key toward developing successful composite electrolytes.

In this work, we developed a scalable method to synthesize thin, flexible and electrochemically stable sulfide-based composite electrolytes with high room-temperature Li<sup>+</sup> conductivities. We hypothesize that an inert chemical environment needs to be created and maintained for sulfide species throughout the solution process. This will suppress the high reactivity of sulfides in the presence of solvents and polymers, which can preserve the intrinsic high conductivity of sulfide electrolytes. Our strategy was to systematically investigate their electrochemical properties and interactions with solvents and polymers to elucidate how sulfide solid electrolytes behave with a variety of functional moieties. This was done by applying both

bulk and surface sensitive characterization tools to different sulfide-solvent and sulfide-polymer mixtures to probe their respective chemical compatibilities. Furthermore, we examined their relative stability in air, and demonstrate the potential use of hydrophobic polymers to improve its moisture stability. Our understanding led to rationale designs of organic/inorganic composite SSE that are found to be stable against lithium metal and show significantly improved chemical stability in air compared with the original sulfide solid electrolyte. This work provides a promising approach towards scalable manufacturing of composite electrolytes to realize high energy ASSBs.

## **3.2 Methods**

### **3.2.1 Glass Ceramic Synthesis**

$\text{Li}_7\text{P}_3\text{S}_{11}$  was synthesized using the melt quench process developed in an earlier study.<sup>167</sup> Precursors  $\text{Li}_2\text{S}$  (99.98%, Sigma Aldrich),  $\text{P}_2\text{S}_5$  (99%, Sigma Aldrich) were mixed in an agate mortar and pestle for 15 minutes in the following stoichiometric ratio:  $70\text{Li}_2\text{S}.30\text{P}_2\text{S}_5$ . Once mixed, the powder was vacuum sealed in a quartz tube. The sealed tube was heated to  $750^\circ\text{C}$  over a period of 4 hours, with 1.5 hours of ramping time. Subsequently, the tube was quickly quenched in an ice bath. Upon cooling, the glassy SSE powder was once again mixed in an agate mortar and pestle for 15 minutes, sealed in a vacuum quartz tube. The sealed tube was then placed in a pre-heated furnace at  $300^\circ\text{C}$  for 2 hours. Subsequently, the tube was quickly removed from the box furnace and quenched in an ice bath. Upon cooling, the final glass ceramic  $\text{Li}_7\text{P}_3\text{S}_{11}$  was grinded in an agate mortar and pestle for 15 minutes before use.

#### **3.2.1.1 Preparation of SSE - Solvent / Polymer Mixtures for Characterization**

All solvents and polymers were obtained from Sigma Aldrich. Solvents used were in anhydrous forms or dried with molecular sieves. Polymer powders were first dried in a heated vacuum oven before use. To prepare sulfide/polymer mixtures, as-synthesized  $\text{Li}_7\text{P}_3\text{S}_{11}$  powder was mixed with different polymers in a vial at a 50:50 wt. ratio. The vial was mixed in an ARM 310

Thinky mixer for 3 minutes at 2000 rpm and allowed to rest for one day before characterization. To prepare the sulfide/solvent mixtures, equal amounts of as-synthesized SSE powder were added to 5 ml of each solvent. The mixtures were hand-swirled briefly to disperse the powders before allowing to rest for 1 hour. Subsequently, the solvents were removed by heating at 60 °C under vacuum overnight to obtain the residual solutes. To eliminate air exposure, all samples were collected and prepared in Argon-filled environment.

In a typical experiment, 250 mg of SEBS polymer was added to 10 ml of solvent. The vial was capped and left to stir until the polymer was fully dissolved. To prepare the electrolyte slurry, SSE was first weighed into a Thinky mixer vial before the polymer solution was added. The vial was then capped and sealed to prevent air exposure before mixing for 3 minutes under 2000 rpm. After mixing, the slurry was casted with a doctor blade and left to dry at room temperature for 1 hour, and overnight at 60 °C under vacuum. Casting was done either on an aluminum current collector or a Teflon plate. The dried films cut from the current collector or peeled from the Teflon plates were pressed under 370 MPa of pressure for at least 3 minutes before use.

### **3.2.1.2 Air Stability Evaluation**

The amount of H<sub>2</sub>S gas generated from the composite electrolyte film due to reaction with moisture in air was measured. A H<sub>2</sub>S gas monitor (SensorCon, Industrial Pro), a fan and the electrolyte film were sealed in an air-filled 0.31 cu ft desiccator (Bel-Art Products). The air temperature was 22-24 °C with a relative humidity between 50-55%. Measurements were taken from the H<sub>2</sub>S gas monitor over a period of 10 minutes and compared against 100 mg of bare Li<sub>7</sub>P<sub>3</sub>S<sub>11</sub> electrolyte. Contact angle of each polymer was collected using a Rame Hart Goniometer and measured with a DROPimage Advanced tool.

### **3.2.2 Experimental Characterization & Electrochemical Testing**



### 3.2.2.1 Materials Characterization

All fabrication processes were conducted in an Ar-filled glovebox (mBraun 200B, H<sub>2</sub>O ppm <0.5, O<sub>2</sub> ppm < 1), unless otherwise noted.

X-ray diffraction (XRD) was conducted using Cu K $\alpha$  radiation ( $\lambda=1.54178$ ) over a  $2\theta$  range of 5-70° with a step size of 0.01°. XRD Rietveld crystal refinement was conducted using the Full-Prof software and the lattice parameters were reported. A Perkin Elmer RamanStation 400F Spectrometer was used to collect Raman spectra intensity values from 134 to 1500 cm<sup>-1</sup>. Raman spectra were then deconvoluted with a range of 350 and 455 cm<sup>-1</sup> using least squares fitting. A FEI Quanta 250 Scanning Electron Microscope was used to characterize the film thickness as well as surface morphology. Thickness of films were noted using the cross-section measurement tool. The AXIS Supra XPS by Kratos Analytical was used to study the chemical degradation of Li<sub>7</sub>P<sub>3</sub>S<sub>11</sub> when exposed to the various polymers and solvents. Binding energies of the mixtures in the phosphorus and sulfur regions were examined against pristine Li<sub>7</sub>P<sub>3</sub>S<sub>11</sub>. The XPS spectra were collected using an emission current of 5 mA and over an area of 700  $\mu\text{m}$  x 300  $\mu\text{m}$ . The spectra were analyzed using CasaXPS software.

### 3.2.2.2 Electrochemical Characterization

EIS measurements were performed with a Solartron 1260 impedance analyzer for the pristine SSE, synthesized electrolyte films and precipitates derived from different solvents. Applied AC potential of 30 mV over a frequency range from 1 MHz to 1 Hz was used for the EIS measurement. The composite films were pressed at 370 MPa before being cut circular discs and placed between two titanium blocking electrodes for measurements. In the symmetric cells, Li foils were placed on both sides of the free-standing film, and lithium plating and stripping were conducted across the film.

### 3.2.2.3 Density Functional Theory (DFT) Calculations

The solvation and reaction energies of sulfur and thiophosphate anions are calculated using the Gaussian 09 quantum chemistry package.<sup>168</sup> The hybrid B3LYP density functional based on Becke's three-parameter exchange functional<sup>169</sup> and the correlation functional of Lee, Yang and Parr<sup>170</sup> were chosen for all calculations. Geometry optimizations were carried out at the B3LYP/6-31+G(d) level, followed by single-point energy calculations at the B3LYP/6-311+G(2d,p) level. The inclusion of diffuse functions in the basis sets ensures an adequate description of the diffuse electron cloud of anions. An SMD solvation model is adopted for all calculations involving solvents.<sup>171</sup>

### 3.3 Results and Discussion

An ideal SSE must meet several key requirements, 1) low overall ionic resistance at room temperature, 2) small thickness to minimize electrolyte vol%, 3) high mechanical robustness to withstand deformation, and 4) good electrochemical stability versus metallic lithium.<sup>172-173</sup> Considering these criteria,  $\text{Li}_7\text{P}_3\text{S}_{11}$  would be an ideal candidate for this study. The glass ceramic  $\text{Li}_7\text{P}_3\text{S}_{11}$  is also known to deliver high room temperature ionic conductivity (up to 1.3 mS/cm) by simple cold press.<sup>167</sup> Although the electrochemical stability window of  $\text{Li}_7\text{P}_3\text{S}_{11}$  is narrow, various studies have found interfacial decomposition products to have ideal properties of ionic conductivity and interface passivation.<sup>107, 167, 174</sup> Additionally,  $\text{Li}_7\text{P}_3\text{S}_{11}$  is a unique glass ceramic SSE that contains various lithium thiophosphates ( $\text{P}_2\text{S}_7^{4-}$ ,  $\text{P}_2\text{S}_6^{4-}$ ,  $\text{PS}_4^{3-}$ ) within its chemical structure, allowing effective characterization of any degradation in its various units. In this work, we first synthesized  $\text{Li}_7\text{P}_3\text{S}_{11}$  powder, which showed expected crystal structure, chemical composition and intrinsic electrochemical properties.<sup>76</sup> The as synthesized SSE powders were used to prepare composite electrolytes.

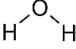
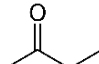
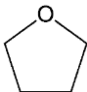
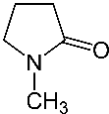
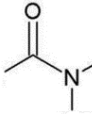
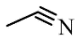
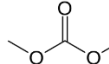
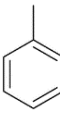
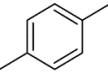
Considering the chemical reactivities of sulfide electrolytes, we must account for potential interactions that might arise between the sulfides and the polymers or solvents. Given that chemical properties of polymers are largely dependent on their functional groups, four types of polymers with different functional groups are chosen for our investigation, including PEO, polyvinylidene fluoride-co-hexafluoropropylene (PVDF-HFP), NBR and polystyrene-*block*-polyethylene-*ran*-butylene-*block*-polystyrene (SEBS). These polymers have been commonly used in battery fabrication.<sup>75, 165, 175-178</sup> Additionally, their distinct functional groups containing oxygen, fluorine or nitrogen make them good candidates for this study. SEBS is a polymer that comprise of only carbon and hydrogen groups, representing another type of chemically inert polymer for comparison. The solvents, acetonitrile (ACN), dimethyl carbonate (DMC), toluene (TOL) and *p*-xylene (XYL) are chosen based on their ability to dissolve the selected polymers. Solid  $\text{Li}_7\text{P}_3\text{S}_{11}$ /polymer composite electrolyte films were synthesized using the solution slurry casting method. To understand the SSE-polymer-solvent behavior and their selection criteria for synthesizing thin flexible electrolyte films, we first isolated the effects of each SSE-solvent and SSE-polymer mixtures respectively and studied their chemical and electrochemical compatibilities.

### 3.2.1 $\text{Li}_7\text{P}_3\text{S}_{11}$ -Solvent Compatibility

To examine the solvent effects on the electrolyte, common solvents: water, methyl ethyl ketone (MEK), tetrahydrofuran (THF), N-methyl-2-pyrrolidone (NMP), dimethylformamide (DMF), ACN, DMC, TOL and XYL were first used for  $\text{Li}_7\text{P}_3\text{S}_{11}$  dispersions. Various color changes were observed as seen in Figure 3.1. While NMP and DMF solutions turned dark green and blue respectively, MEK, THF and ACN solutions turned yellow initially before settling to a yellowish-white color. This is an indication of chemical degradation of  $\text{Li}_7\text{P}_3\text{S}_{11}$  when exposed to these solvents. To characterize these degradations, solvents were removed, and their precipitates collected for XRD, Raman and XPS analysis. Only electrolyte precipitates obtained from ACN,

DMC, TOL and XYL dispersions were selected for characterization as they were solvents used to dissolve the respective polymers.

**Table 3.1.** Common solvents used in battery materials and its polarities and dielectric constants.

Solvent	Water	MEK	THF	NMP	DMF	ACN	DMC	TOL	XYL
<b>Polarity Index</b>	10.2	4.7	4	6.7	6.4	5.8	4.7	2.4	2.5
<b>Dielectric Constant</b>	80.1	18.2	7.5	32.3	37.2	35.7	3.1	2.4	2.3
<b>Structure</b>									
<b>Color on Mix</b>	Light Yellow	Yellow White	Yellow White	Dark Green	Dark Blue	Yellow White	Nil	Nil	Nil

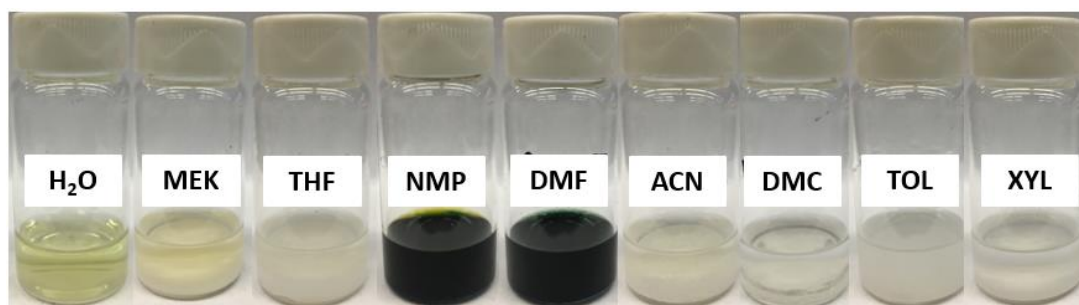


**Figure 3.1** Different solvent color changes after addition of  $\text{Li}_7\text{P}_3\text{S}_{11}$ .

As shown in Figure 3.2, the XRD patterns of solutes derived from ACN and DMC solutions no longer matched that of the pristine  $\text{Li}_7\text{P}_3\text{S}_{11}$ . The crystal structure of  $\text{Li}_7\text{P}_3\text{S}_{11}$  has completely degraded, evident from the absence of main peaks in the pristine pattern. It is difficult to determine the specific degradation products formed from just the XRD patterns as it is likely a mixture of various phosphorus and sulfide derivatives in both crystalline and amorphous phases. Conversely, patterns derived from the TOL and XYL dispersions (Figure 3.2b) remain unchanged compared to the pristine pattern, indicating the feasibility of using these solvents to retain the crystalline structure of  $\text{Li}_7\text{P}_3\text{S}_{11}$  during the solution mixing process.

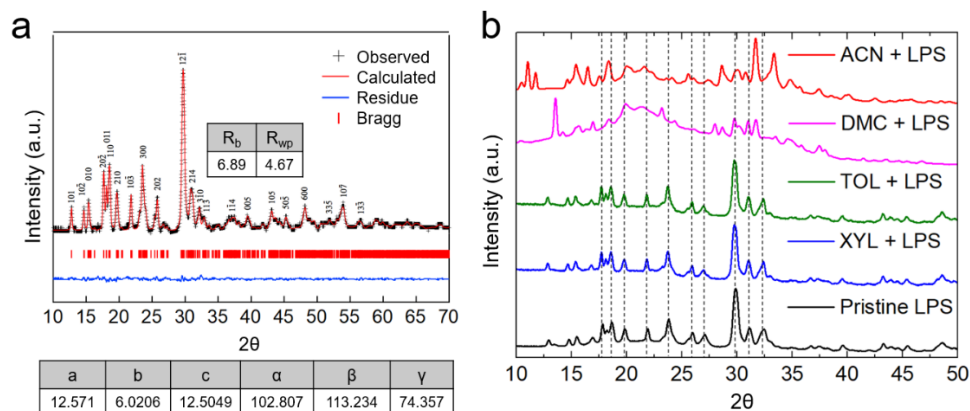


**Figure 3.2.** (a) Rietveld refinement of pristine  $\text{Li}_7\text{P}_3\text{S}_{11}$ , the refinement model was adapted from literature.<sup>179</sup> (b) XRD patterns of  $\text{Li}_7\text{P}_3\text{S}_{11}$  after dispersion in: ACN, DMC, TOL, XYL.

The Raman spectra in Figure 3.3a reaffirm findings in the XRD study, where precipitates derived from TOL and XYL dispersions were able to retain the characteristic Raman modes of pristine  $\text{Li}_7\text{P}_3\text{S}_{11}$  (Figure 3.3b), while precipitates from ACN and DMC dispersions were distinctly different. Relative intensities of the main conduction modes  $\text{P}_2\text{S}_7^{4-}$  ( $406\text{ cm}^{-1}$ ) decreased while  $\text{PS}_4^{3-}$  ( $420\text{ cm}^{-1}$ ) and  $\text{P}_2\text{S}_6^{4-}$  ( $385\text{ cm}^{-1}$ ) increased significantly. The result indicates that the dispersion of SSE in ACN and DMC solvents favors decomposition of  $\text{Li}_7\text{P}_3\text{S}_{11}$ , generating the undesired products. There was also an unknown product shown at the wavelength of  $430\text{ cm}^{-1}$  for solute from the ACN dispersion which requires additional analysis to identify. According to the XRD and Raman analysis, there are significant changes to both bulk and local structures of electrolyte dispersed in ACN and DMC solvent compared to pristine  $\text{Li}_7\text{P}_3\text{S}_{11}$ . To identify any additional specific decomposition products, X-ray photoelectron spectroscopy (XPS) was conducted on all precipitates and combined XPS binding energies are plotted in Figure 3.3c. As the binding energies of various phosphorus and sulfur products are similar, with energies of  $\text{P}_2\text{S}_7^{4-}$  and  $\text{P}_2\text{S}_6^{4-}$  overlapping at  $161.5\text{ eV}$ , it was difficult to deconvolute these products from the peak patterns. However, it was observed that peak shapes of solutes from ACN and DMC dispersions were blue-shifted in the phosphorus region (Figure 3.3c), indicating an increased amount of  $\text{PS}_4^{3-}$  mode, consistent with the Raman analysis. Additionally, the XPS analysis also showed no phosphate or sulfate products present. This suggests that solvent-induced degradation of  $\text{Li}_7\text{P}_3\text{S}_{11}$

was not a result of any chemical reaction with the solvents containing oxygen/nitrogen groups, but due to the degradation of the  $\text{Li}_7\text{P}_3\text{S}_{11}$  itself, forming decomposed products such as  $\text{P}_2\text{S}_6^{4-}$  and  $\text{PS}_4^{3-}$ . This likely occurs from a partial or complete dissolution of pristine  $\text{Li}_7\text{P}_3\text{S}_{11}$  in certain solvents, and the subsequent reaction forming undesired Li/P/S derivatives after the solvents were removed. These findings agree with existing solution-based synthesis methods of sulfide SSEs, where solvents such as ACN are used in the dissolution and precipitation of precursors followed by heat treatment during the synthesis process.<sup>96, 98, 180</sup>

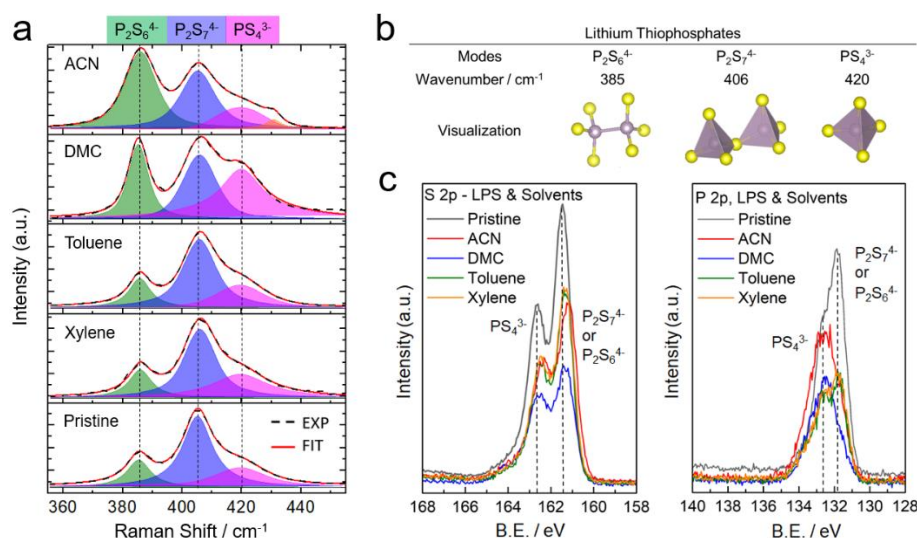


**Figure 3.3.** (a) Deconvoluted Raman spectra of  $\text{Li}_7\text{P}_3\text{S}_{11}$  after dispersion in different solvents. (b) Visualizations of detected lithium thiophosphates present. (c) XPS spectra of 2p regions of sulfur and phosphorus showing the combined binding energies of  $\text{Li}_7\text{P}_3\text{S}_{11}$  after dispersion.

To better understand the relationship between  $\text{Li}_7\text{P}_3\text{S}_{11}$  and the respective solvents, we can compare the solvent relative properties using their polarity indexes and dielectric constants. From Table 1, one can identify a qualitative trend between the solvent polarity and its degradative effect on  $\text{Li}_7\text{P}_3\text{S}_{11}$ , consistent with some reported literature.<sup>165, 181</sup> However, this trend is more pronounced when dielectric constants are considered. As dielectric constant of the solvent increases, a greater degree of degradation was observed visually through their color changes as well as based on the above XRD, Raman and XPS analysis. To further analyze solvent polarity

and dielectric constant effects, computational methods were used to examine their molecular level interactions.

### 3.2.2 Computational DFT Calculations of Molecular Interactions

Using DFT calculations, we find that the solvation free energies of  $P_2S_7^{4-}$  become more favorable as dielectric constant of solvent increases (Figure 3.4a), indicating that these components are more likely to dissolve in polar solvents with high dielectric constants. In addition, reaction energies were calculated for two reactions involving  $P_2S_7^{4-}$ , the characteristic building unit of  $Li_7P_3S_{11}$ . Reaction A:  $2e^- + P_2S_7^{4-} \rightarrow P_2S_6^{4-} + S^{2-}$ , and reaction B:  $P_2S_7^{4-} + S^{2-} \rightarrow 2PS_4^{3-}$ . The reaction A forming  $P_2S_6^{4-}$  and  $S^{2-}$  becomes highly favorable as the dielectric constant of solvent increases (Figure 3.4b). This explains the experimental observation of increased  $P_2S_6^{4-}$  after mixing  $Li_7P_3S_{11}$  in solvents such as ACN with larger dielectric constant (Figure 3.3a). In contrast, reaction B between  $P_2S_7^{4-}$  and the  $S^{2-}$  intermediate to form  $PS_4^{3-}$  is more favorable for solvents with lower dielectric constants (e.g.,  $< 10$ ), and remains relatively constant for solvents with dielectric constants  $> 10$ . This suggests that  $PS_4^{3-}$  formation is driven by a combination of  $S^{2-}$  formation from the first reaction A (favored by higher dielectric constants) and the subsequent reaction B of that intermediate to form  $PS_4^{3-}$  (favored by low dielectric constants). This explains why an increase in the intensity for  $PS_4^{3-}$  is observed in an intermediate dielectric constant DMC, lower dielectric constant solvents such as TOL and XYL would limit  $S^{2-}$  formation, while higher dielectric constant solvents such as ACN would inhibit  $PS_4^{3-}$  formation. These indicate that conductive and crystalline properties of  $Li_7P_3S_{11}$  can be retained using solvents with relatively low dielectric constants such as TOL and XYL.

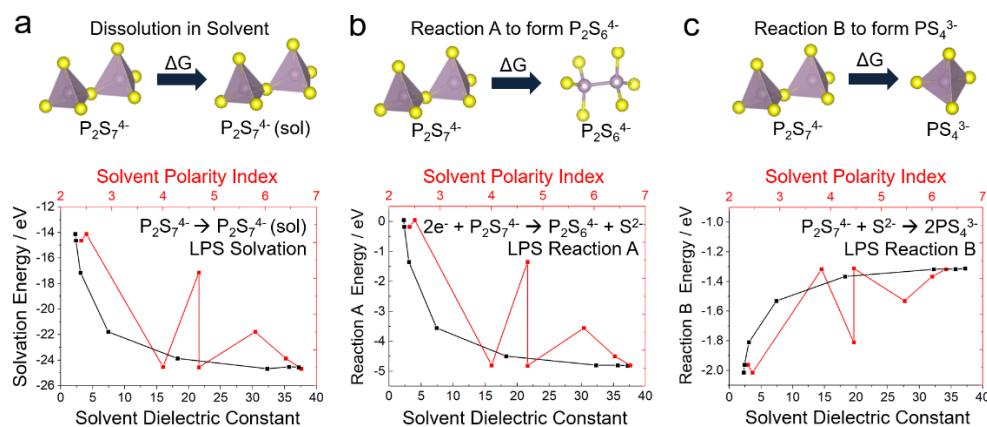


**Figure 3.4.**  $\text{Li}_7\text{P}_3\text{S}_{11}$  – Solvent degradation mechanism vs solvent polarity / dielectric constant: (a)  $\text{P}_2\text{S}_7^{4-}$  dissolution energies. (b)  $\text{P}_2\text{S}_7^{4-}$  reaction A energies forming  $\text{P}_2\text{S}_6^{4-}$  and  $\text{S}^{2-}$ . (c)  $\text{P}_2\text{S}_7^{4-}$  and  $\text{S}^{2-}$  reaction B energies forming  $\text{PS}_4^{3-}$ . Calculation details can be found in the methods section.

These findings are validated by the EIS measurements (Figure 3.5) of SSE powders collected after the solvent removal. Specifically, the precipitates from ACN and DMC solvent mixtures showed a loss of 2-3 orders of magnitude in conductivities, at  $7.4 \times 10^{-7}$  and  $1.1 \times 10^{-5}$   $\text{S cm}^{-1}$ , respectively (Table 2). This results from a large charge transfer resistance represented by the semi-circle feature in the Nyquist plots of ACN and DMC dispersed SSE powders (Figure 3.5). This is expected as the decomposed products of  $\text{PS}_4^{3-}$  and  $\text{P}_2\text{S}_6^{4-}$  formed are either poor conductors or insulative in nature, contributing to increased resistance of the electrolyte. By contrast, the conductivity of precipitates from TOL and XYL measured at  $1.12 \times 10^{-3}$  and  $1.19 \times 10^{-3}$   $\text{S cm}^{-1}$ , respectively, retaining almost all the pristine conductivity of  $1.2 \times 10^{-3}$   $\text{S cm}^{-1}$ .



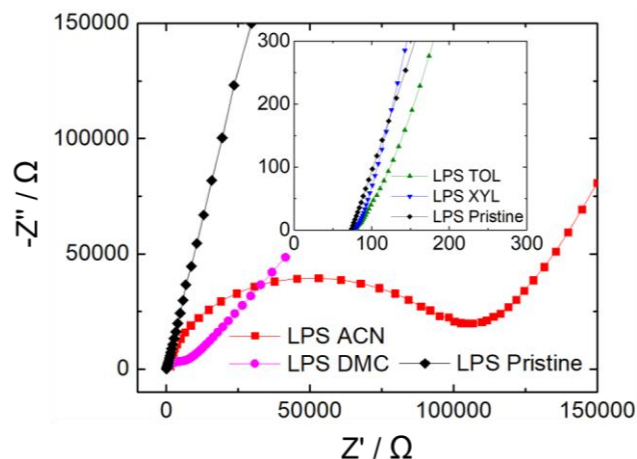


**Figure 3.5.** Nyquist plots of  $\text{Li}_7\text{P}_3\text{S}_{11}$  EIS measurements after dispersion in different solvents, showing large charge transfer resistances from ACN and DMC dispersions, the high frequency inset shows TOL and XYL dispersions.

**Table 3.2.** Conductivity measurements of  $\text{Li}_7\text{P}_3\text{S}_{11}$  after dispersion in different solvents.

Solvent	Conductivity / $\text{S cm}^{-1}$
Pristine	$1.20 \times 10^{-3}$
Xylene	$1.19 \times 10^{-3}$
Toluene	$1.12 \times 10^{-3}$
DMC	$1.11 \times 10^{-5}$
ACN	$7.4 \times 10^{-7}$

From the characterization study, it is clear that solvent selection is crucial to the performance of composite electrolytes. Chemical degradation was observed in  $\text{Li}_7\text{P}_3\text{S}_{11}$  when dispersed in polar solvents with high dielectric constants such as ACN and DMC, while chemical structure and ionic conductivities were retained when non-polar solvents with low dielectric constant such as TOL and XYL were used.

### 3.2.3 $\text{Li}_7\text{P}_3\text{S}_{11}$ -Polymer Compatibility

To examine effects of polymer on the composite electrolyte,  $\text{Li}_7\text{P}_3\text{S}_{11}$  and respective polymers including PEO, PVDF-HFP, NBR and SEBS were mixed and characterized. A 50:50 wt% ratio was used to ensure excess of polymer in the mixtures to exaggerate any potential reactions observed. However, no reactions or electrolyte degradation was detected in the SSE-

polymer mixtures. The Raman spectra of all mixtures retained both peak positions and relative intensities of lithium thiophosphate modes  $P_2S_7^{4-}$ ,  $PS_4^{3-}$  and  $P_2S_6^{4-}$ , indicating retention of the local structures of  $Li_7P_3S_{11}$ . XPS analysis was also conducted to identify any new phosphorus and sulfur products formed as a result of any side reactions in each mixture. Consistent with the Raman analysis, no new reaction or decomposition products were detected by XPS. The characteristic peak patterns matched the pristine counterparts in both the phosphorous and sulfur regions, comprising the main components of  $P_2S_7^{4-}$  and  $PS_4^{3-}$ . As a result, we are not able to detect any chemical reactions or electrolyte decomposition from the dry mixtures of  $Li_7P_3S_{11}$  and the respective polymers. However, this analysis does not account for other potential interactions such as localized electrostatic interactions or coordination between the nucleophilic phosphorus groups in the SSE and electronegative oxygen or fluorine groups in polymers. While it is also important to study such behavior to understand their physical behavior, we will focus instead on the chemical and electrochemical effects since they ultimately determine the composite electrolyte's properties. Accordingly, suitable polymer-solvent pairs include polymers with weak or no electronegative groups which can be readily dispersed in non-polar solvents with low dielectric constants. From the analysis, SEBS polymer and *p*-xylene appear to be a suitable choice.

### **3.2.4 Electrochemical Evaluation of $Li_7P_3S_{11}$ – Polymer Composite**

Composite films of  $Li_7P_3S_{11}$  and SEBS were fabricated by casting slurries with XYL as the solvent. The thickness of the composite electrolyte films can be controlled at approximately 50  $\mu\text{m}$  or less (Figure 3.6a). For this study, all composites were synthesized with 5 wt.% of polymer to minimize variables. Lower weight percent of polymer may be used to optimize the electrochemical performance in future studies. With this composition, large area composite electrolyte films can be fabricated (Figure 3.6b). The flexibility of composite film was demonstrated.<sup>76</sup> The fabricated composite film electrolyte's room temperature conductivity was

evaluated via electrochemical impedance spectroscopy (EIS) (Figure 3.6a). Titanium blocking electrodes were used in the test, which measured resistances of 10 ohms across the 55  $\mu\text{m}$  thick film (Figure 3.6c), translating to an area specific resistance of  $3.9 \Omega \text{ cm}^2$ .

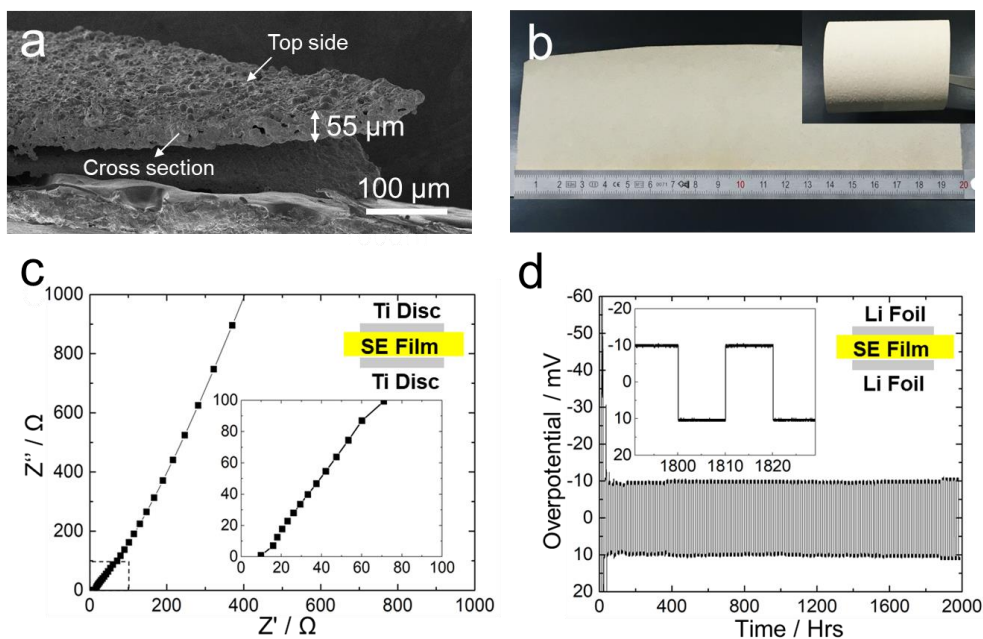


**Figure 3.6.** (a) Cross-section SEM image of composite electrolyte film fabricated with 95 wt.%  $\text{Li}_7\text{P}_3\text{S}_{11}$  and 5 wt.% SEBS. (b) Digital photograph of a 20 cm \* 6 cm casted electrolyte film and a rolled-up film (inset). (c) Nyquist plot of the composite electrolyte film. (d) Li plating and stripping across composite electrolyte film with 100 cycles at 20 hours per cycle. The inset shows setup used. All measurements were done at room temperature.

Its conductivity was calculated to be  $0.7 \text{ mS cm}^{-1}$ , which is within the expected conductivity loss from pure  $\text{Li}_7\text{P}_3\text{S}_{11}$  at  $1.2 \text{ mS cm}^{-1}$ . Conductivity losses are expected to vary based on the composition and can be minimized with further reductions in polymer wt%. Addition of polymer into the composite also introduced extra porosity into the matrix, the pores are non-conductive and contribute to resistance of the film. However, despite losses in specific conductivity, the significant reduction ( $> 1$  order) in electrolyte thickness can still give rise to dramatic decrease in the overall resistance compared to the bulk pristine electrolyte pellets. While EIS measurements can provide quantitative understanding of electrolyte conductivity based on charge transfer, its limitations include inability to provide qualitative information such as the identity of the conducting

species. To ensure no other components such as proton species or water adsorption influenced the measurements, non-blocking electrodes were also used. Plating and stripping was performed with 20 hours per cycle using a current of  $0.11 \text{ mA cm}^{-2}$  at room temperature. The electrolyte film was found to remain stable over 2000 hours of cycling, with a measured overpotential of 10 mV. It is observed that the plating overpotential of the symmetric cell was high initially and stabilized after a several cycles. This can be attributed to the poor dotted contact between Li foil and the fresh surface of the electrolyte film at the initial stage. We hypothesize that as plating and stripping proceeds, the gaps gradually become filled, and contact improved over extended cycling, allowing plating overpotentials to stabilize.

### **3.2.5 Air / Moisture Stability Test**

The hydrophobicity of each polymer used was first compared by measuring their contact angles with water. SEBS was found to be the most hydrophobic polymer (with a contact angle of  $103^\circ$ ) in the study. Subsequently, moisture stability in air of the composite electrolyte was tested based on the quantity of  $\text{H}_2\text{S}$  evolved during air exposure of  $\text{Li}_7\text{P}_3\text{S}_{11}$  (Figure 3.7a). The use of hydrophobic SEBS in the composite electrolyte was found to significantly improve the film's moisture stability in air with a relative humidity of 50-55% compared to the bare  $\text{Li}_7\text{P}_3\text{S}_{11}$  powder. Using 5 wt.% of SEBS in the composite electrolyte, considerably reduced  $\text{H}_2\text{S}$  evolution was observed compared with bare  $\text{Li}_7\text{P}_3\text{S}_{11}$  samples under the same exposure condition (Figure 3.7b).

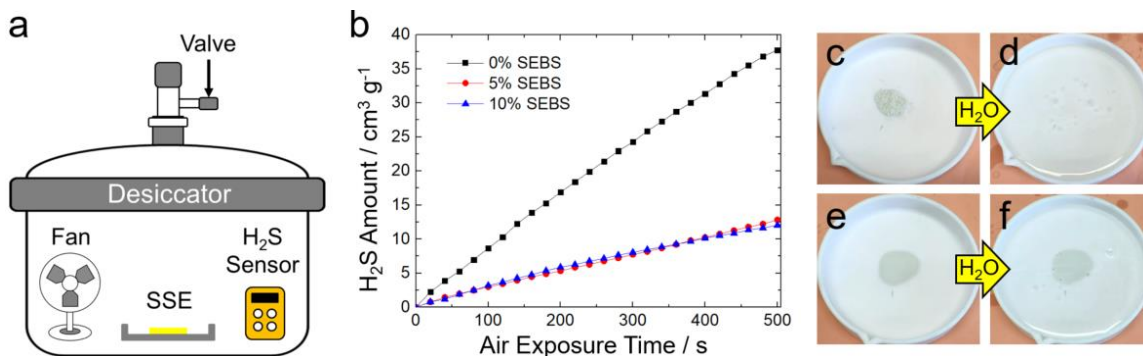


**Figure 3.7.** (a) Setup used for H<sub>2</sub>S gas measurements from 100 mg of Li<sub>7</sub>P<sub>3</sub>S<sub>11</sub> hydrolysis in air. (b) H<sub>2</sub>S amount released vs time for fixed volume air exposed to: 100 mg bare Li<sub>7</sub>P<sub>3</sub>S<sub>11</sub>, 100 mg composite with hydrophobic SEBS polymer. (c) & (d) Bare Li<sub>7</sub>P<sub>3</sub>S<sub>11</sub> before and after flooding in water, showing full hydrolysis and disappearance in water. (d) & (e) Composite electrolyte film before and after flooding in water, showing retention of the film.

To further examine the effects of moisture on the electrolyte stability, distilled water was gradually added to a dish containing 100 mg of bare electrolyte, and the composite electrolyte film. From Figures 3.7c & 3.7d, it is observed that the bare electrolyte completely degraded upon contact with water, while the composite electrolyte film remained intact despite being fully submerged in water (Figures 3.7e & 3.7f). This result indicates that use of hydrophobic polymers can help to stabilize the water-sensitive Li<sub>7</sub>P<sub>3</sub>S<sub>11</sub> electrolyte in moisture, potentially improving the processability of sulfide-based electrolytes in dry room conditions if other super-hydrophobic materials can be used.

### 3.4 Conclusion

In summary, this study seeks to elucidate various polymer and solvent interactions and their compatibilities with a representative sulfide solid electrolyte. We demonstrated that by using an SSE such as Li<sub>7</sub>P<sub>3</sub>S<sub>11</sub>, in combination with non-polar solvents of low dielectric constant such as *para*-xylene and a corresponding polymer without electronegative functional groups such as SEBS, highly conductive ( $\sim 0.7 \text{ mS cm}^{-1}$ ), thin electrolyte films ( $\sim 50 \text{ }\mu\text{m}$ ) with good mechanical properties can be fabricated. The composite electrolyte film was also found to be electrochemically stable with lithium over long cycles of plating and stripping (2000 hours,  $1.1 \text{ mAh cm}^{-2}$  per cycle), potentially enabling the use of metallic lithium anode in ASSBs. Moreover,

the use of hydrophobic SEBS was also found to improve moisture stability of  $\text{Li}_7\text{P}_3\text{S}_{11}$  in air. The principles of SSE-polymer-solvent selection found in this study can be further extended to other SSE-polymer-solvent compositions and optimized to achieve better performance. Additionally, the knowledge gained in this study may provide new material selection philosophy and lead to development of future scalable methods to produce high-performance, low-cost ASSBs.

Chapter 3, in full, is a reprint of the material “Enabling Thin and Flexible Solid-State Composite Electrolytes by the Scalable Solution Process.” as it appears in ACS Applied Energy Materials. Tan, D. H. S.; Banerjee, A.; Deng, Z.; Wu, E. A.; Nguyen, H.; Doux, J.-M.; Wang, X.; Cheng, J.-h.; Ong, S. P.; Meng, Y. S.; Chen, Z. 2019, 2, 6542–6550. The dissertation author was the first author of this paper, all authors contributed to this work.

## Chapter 4. Enabling Carbon Free Silicon Anodes for Robust ASSBs

The development of silicon anodes to replace conventional graphite in efforts to increase energy densities of lithium-ion batteries has been largely impeded by poor interfacial stability against liquid electrolytes. Here, stable operation of 99.9 weight% micro-Si ( $\mu\text{Si}$ ) anode is enabled by utilizing the interface passivating properties of sulfide based solid-electrolytes. Bulk to surface characterization, as well as quantification of interfacial components showed that such an approach eliminates continuous interfacial growth and irreversible lithium losses. In  $\mu\text{Si} ||$  layered-oxide full cells, high current densities at room temperature ( $5 \text{ mA cm}^{-2}$ ), wide operating temperature ( $-20^\circ\text{C}$  to  $80^\circ\text{C}$ ) and high loadings ( $>11 \text{ mAh cm}^{-2}$ ) were demonstrated for both charge and discharge operations. The promising battery performance can be attributed to both the desirable interfacial property between  $\mu\text{Si}$  and sulfide electrolytes, as well as the unique chemo-mechanical behavior of the Li-Si alloys.

### 4.1 Introduction

Recent years have seen a rapid growth in demand for batteries to serve a wide variety of energy storage applications. While lithium ion batteries (LIBs) have done well to serve the needs of conventional portable devices, emerging markets in electric vehicles (EVs) and large scale grid storage necessitate batteries to be safer, lower in costs as well as more energy dense. To this end, silicon (Si), with a specific capacity exceeding  $3500 \text{ mAh g}^{-1}$ , has emerged as a promising alternative to graphite-based anodes (with specific capacity of around  $370 \text{ mAh g}^{-1}$ ) in order to increase energy density of LIBs.<sup>182-183</sup> Beyond being the second most abundant element in the Earth's crust, it is also environmentally benign and exhibits electrochemical potentials close to graphite ( $0.3 \text{ V vs Li/Li}^+$ ).<sup>183</sup> Unfortunately, commercialization of Si anodes is hindered by its poor cycle and calendar life resulting from continuous solid electrolyte interphase (SEI) growth between the highly reactive Li-Si alloy and organic liquid electrolytes used in LIBs. This is further exacerbated by its large volumetric expansion ( $>300\%$ ) during lithiation causing electrode

pulverization, and loss of Li<sup>+</sup> inventory due to irreversible trapped Li-Si alloy enclosed within the SEI formed.<sup>184</sup> Current efforts to mitigate capacity fade include the use of sophisticated Si nanostructures in combination with carbon composites, robust binder matrix to mitigate pulverization, and Si pre-lithiation to reduce effects of Li loss.<sup>182, 184-187</sup> Liquid electrolyte modifications, including the use of cyclic ethers, fluorinated additives or other ionic liquids additives that stabilize the SEI have also been explored.<sup>186, 188</sup> While improvements are reported, such strategies are still limited in enabling stable cycling with high loading Si and beyond 100 cycles in the full cell (Figure 4.1). Potentially effective solutions need to address the fundamental failure mechanisms at the Si electrode-electrolyte interface that cause poor cycle and calendar life. To realize high energy density, binder and carbon conductive additive ratios also need to be kept at a minimum.

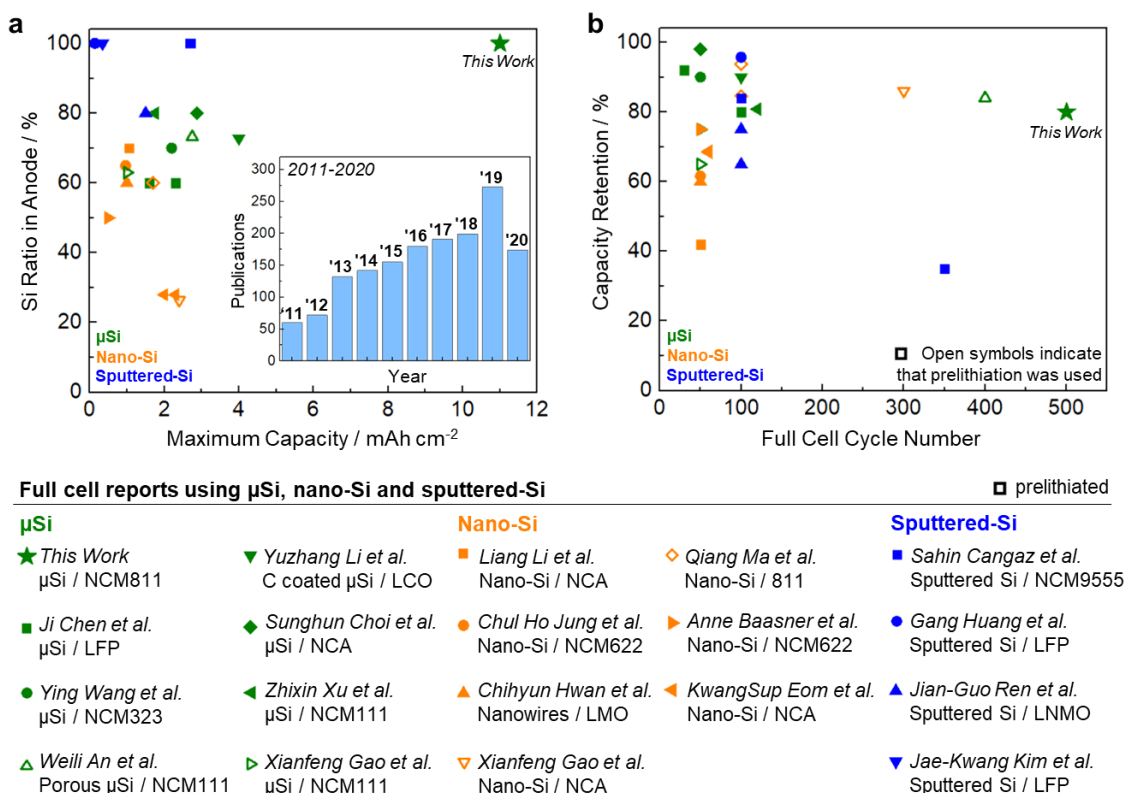


**Figure 4.1.** Literature summary on Si anodes classified by  $\mu$ Si, nano-Si and sputtered-Si. (a) Plot of Si ratio in anode vs maximum capacity for full cells, inset shows the number of Si publications per year in the past decade, with a vast majority presenting only half-cell studies. (b) Plot of capacity retention vs Full cell cycle numbers reported. Open symbols indicate that pre-lithiation was used.



To obtain a better understanding of the state-of-the-art, reports on Si anode-based full cells containing only Si as the electrochemically active material (without graphite or other alloys) are summarized in Figure 4.1a.<sup>186, 189-205</sup> Despite a vast majority of literature reports on half cells, the uncontrolled amounts of lithium excess used were difficult to determine, which makes proper evaluation challenging. As such, only full cell data points with 0% excess Li<sup>+</sup> or with controlled pre-lithiation were selected for this comparison. These studies can be classified into 3 main categories: those adopting 1)  $\mu$ Si particles, 2) nano-Si particles and 3) sputtered-Si thin films. From Figure 4.a1, it becomes clear that most reports adopt composites containing between 60 to 80 wt% Si, with carbon additives and polymeric binders typically making up the rest of the electrode. While carbon and binder additives are necessary to maintain an electronically conductive network as well as to mitigate effects of volume expansion, these also negatively affect gravimetric and volumetric energy densities achievable in the cell. Figure 4.1b shows that most reported full cell performances are limited to 100 cycles, apart from a few that demonstrated longer cycle life using various pre-lithiation strategies to compensate for Li<sup>+</sup> inventory losses. While pre-lithiation is widely believed to be effective to enable extended cycle life, the ideal Si anode should be composed of pristine  $\mu$ Si particles that do not require further treatment, reaping the benefits of low costs, ambient air-stability and environmentally benign properties. Similarly, sophisticated Si nano-structures also increase the complexity of materials fabrication, resulting in higher costs. Thus, it is vital to address the two key challenges of  $\mu$ Si anodes: a) achieving high  $\mu$ Si loading with minimal incorporation of carbon and binder, b) stabilizing interfacial growth (SEI) originating from volume expansion, and Li<sup>+</sup> consumption due to trapped Li-Si formation.

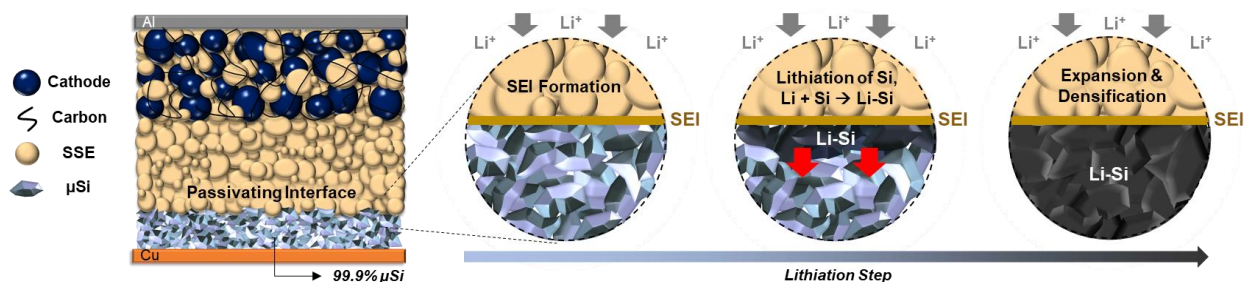


**Figure 4.2.** Schematic of 99.9 wt%  $\mu\text{Si}$  electrode in an all solid-state full cell. 1) During lithiation, a passivating SEI is formed between the  $\mu\text{Si}$  electrode and the SSE, followed by lithiation of  $\mu\text{Si}$  particles near the interface. 2) The highly reactive Li-Si then reacts with Si particles within its vicinity. 3) The reaction propagates throughout the electrode, forming a densified Li-Si layer.

Recognizing that the Si stability problems arise mainly from the liquid electrolyte interface, the use of solid-state electrolytes (SSEs) in an all solid-state battery (ASSB) cell configuration is a promising alternative approach, due to its ability to form a stable SEI<sup>36</sup> while also reducing the need for large amounts of carbon or binder additives in the anode composite. This would directly address the two fundamental problems faced by Si anodes in liquid electrolytes and extend the calendar life of the cell due to the passivating nature of SSE-electrode interfaces. In this work,  $\mu\text{Si}$  electrode consisting of 99.9 wt% Si is used in a  $\text{Li}_6\text{PS}_5\text{Cl}$  argyrodite SSE system to enable high areal capacities as well as long cycle life of a  $\mu\text{Si}||\text{SSE}||$ lithium nickel cobalt manganese oxide (NCM811) full cell. This is achieved by adopting a  $\mu\text{Si}$  electrode prepared using 0.1wt% PVDF binder and no additional carbon additives (Figure 4.2). As bulk  $\mu\text{Si}$  already exhibits a sufficient electronic conductivity of about  $3 \times 10^{-5} \text{ S cm}^{-1}$ , comparable to most common cathode materials ( $\sim 10^{-6}$  to  $10^{-4} \text{ S cm}^{-1}$ ), carbon additives are no longer necessary.<sup>206-207</sup> Moreover, carbon has also been found to be detrimental to the stability of SSEs, as it increases the kinetics of SSE decomposition at both the anode and cathode interfaces.<sup>149, 208</sup> Unlike its liquid counterparts, the SSE does not permeate through the porous  $\mu\text{Si}$  electrode, and the interfacial contact area between the SSE and the  $\mu\text{Si}$  electrode is significantly reduced to a 2D plane. As a result, during cell cycling, the passivating nature of the SEI formed dramatically reduces both  $\text{Li}^+$  consumption as well as trapped Li-Si typically observed in liquid electrolyte-based cells. A stable SEI formation using SSEs also enables long calendar life by preventing unwanted side reactions between the

highly reactive Li-Si alloy and organic liquid electrolytes. During lithiation of  $\mu\text{Si}$ , Li-Si formation can propagate throughout the electrode, benefiting from the direct contact between Li-Si and Si particles in the absence of any SEI or electronically insulative components such as electrolytes or binder (**Fig 2**). This process was found to be highly reversible at relatively high current densities up to  $5 \text{ mA cm}^{-2}$ , able to operate between  $-20^\circ\text{C}$  to  $80^\circ\text{C}$ , as well as deliver high areal capacities of up to  $11 \text{ mAh cm}^{-2}$ . Without any excess lithium, the  $\mu\text{Si}$ -NCM811 full cell was found to deliver a capacity retention of 80% after 500 cycles, demonstrating the overall robustness of  $\mu\text{Si}$  anodes enabled by ASSBs.

## 4.2 Methods

### 4.2.1 Materials Preparation

Commercial  $\text{Li}_6\text{PS}_5\text{Cl}$  was obtained from NEI Corporation and used as received for the SSE separator layer. The  $\mu\text{Si}$  particles were obtained from Alfa Aesar and used as received. The PVDF binder used for the anode was obtained from Kynar (HSV-900) and used as received. The PTFE binder used for the cathode was obtained from DuPont and used as received. VGCF was obtained from Sigma Aldrich (Graphitized, Iron-free), and the carbon black was obtained from STREM Chemicals, both were used as received. NCM811 protected with a boron based coating layer was obtained from LG Chem and used as received. To prepare the 99.9 wt%  $\mu\text{Si}$  anode, a slurry was prepared using the  $\mu\text{Si}$  particles, N-Methyl-2-Pyrrolidone solvent and 0.1 wt% of the PVDF binder, before casting on a copper current collector using a doctor blade. The casted electrode was left to dry under vacuum at  $80^\circ\text{C}$  overnight to remove the solvent, before punching to obtain the electrode discs. To prepare the dry cathode electrodes, NCM811,  $\text{Li}_6\text{PS}_5\text{Cl}$ , VGCF and PTFE were first mixed in a heated mortar and pestle before being hot rolled using a polished titanium or stainless-steel cylinder. The electrodes were repeatedly rolled until the desired thickness was achieved, before being punched out for cell assembly. For the cathode composite electrode, the  $\text{Li}_6\text{PS}_5\text{Cl}$  was pre-milled in a 45 ml  $\text{ZrO}_2$  ball mill jar (Emax, Retsch) sealed in Ar

gas to reduce its particle size and promote interface contact with the cathode particles. Wet ball milling was conducted for 2 hours at room temperature and at 300 rpm using anhydrous xylene as the dispersant. The dispersed milled powders were then extracted and dried under vacuum at 80°C overnight before use in the dry process cathode composite fabrication.

#### 4.2.2 Materials Characterization

XRD was conducted using Cu K $\alpha$  radiation ( $\lambda=1.54178 \text{ \AA}$ ) over a  $2\theta$  range of 5-70° with a step size of 0.01°. In a typical experiment, pristine and cycled electrodes were first extracted from the cell and hand ground using an agate mortar and pestle before being sealed in Ar gas for the measurement. ICSD database was used to reference the identified peaks of Li<sub>2</sub>S and Li<sub>6</sub>PS<sub>5</sub>Cl. The AXIS Supra XPS by Kratos Analytical was used to study the Si-SSE interface products after cell was charged with and without carbon additives. Binding energies of the mixtures in the lithium 1s, sulfur 2p and silicon 2p regions were examined against pristine silicon-Li<sub>6</sub>PS<sub>5</sub>Cl. The XPS spectra were collected using an emission current of 5 mA and over an area of 700  $\mu\text{m}$  x 300  $\mu\text{m}$ . The spectra were analyzed using CasaXPS software. As sulfide-based materials are sensitive to air and moisture, decomposing to form toxic gases such as H<sub>2</sub>S, all synthesis and testing steps are done within an Argon-filled glovebox (MBraun MB 200B, H<sub>2</sub>O < 0.5 ppm, O<sub>2</sub> < 5.0 ppm). In the TGC method used to quantify SEI and trapped Li-Si growth, the following steps were conducted: after cell cycling, the cathode electrode was removed from the full cell while the rest of the cell containing the Cu foil, anode and SSE were fully submerged in anhydrous ethanol within the Ar-filled jar to react with the Li-Si completely, producing H<sub>2</sub> gas as reaction products. Subsequently, a gas-tight syringe was used to transfer 30  $\mu\text{l}$  of the mixed gas from the container into the TGC system for measurement. The amount of Li-Si derived from quantified H<sub>2</sub> gas was calculated against a standard H<sub>2</sub> gas calibration curve. FEI Scios Dualbeam was used for the cross-section SEM imaging. In a typical experiment, the cycled full cell was transferred from an Argon-filled glovebox to the instrument via an air-free quick loader (FEI) to avoid sample

contamination in air. Ga<sup>+</sup> milling was conducted normal to the sample surface using cross-sectional and cross-sectional cleaning procedures at various currents. SEM-EDX imaging was conducted using the in-built functional tool of the FEI Scios Dualbeam. In the X-ray computed tomography (CT) measurements, a homemade cell was designed to enable high resolution via smaller voxel sizes. A 4 mm diameter PTFE rod was drilled with a 2mm internal diameter and capped with 2mm PTFE rods before being sealed using epoxy with the dry / solution processed cathode composite electrodes enclosed within. X-ray CT was conducted with a Versa 510 (Zeiss/Xradia) X-ray microscope, and a source voltage of 80kV using the LE2 filter. Analysis of the reconstruction data was performed using Amira2019.1 (ThermoFisher Scientific) software.

#### **4.2.3 Electrochemical Characterization**

EIS measurements were performed with a Solartron 1260 impedance analyzer for the pristine  $\mu$ Si-SSE-NCM811 full cell and cycled cells at every 6 cycles at the discharged state. An applied AC potential of 30 mV over a frequency range from 1 MHz to 0.1 Hz was used for the EIS measurement. The measurements were conducted at room temperature using two titanium blocking electrodes enclosed by a PEEK holder. To fabricate the full cells, 75 mg of Li<sub>6</sub>PS<sub>5</sub>Cl was first pressed between two titanium rods at 370 MPa, forming a separator layer of 10 mm in diameter. Following which, casted  $\mu$ Si were then matched against free standing dry processed cathode composite films at NP ratios of 1.1 before being pressed against opposite sides of the SSE pellet under 370 MPa with titanium plungers which also acted as current collectors. Cell cycling was done under a stack pressure of 50 MPa using a Neware Battery cycler and analyzed with BTS9000 software. For the temperature operation tests, cells were cycled within a temperature chamber with wiring feed throughs to the battery cycler. Likewise, the self-discharge tests at elevated temperatures were also conducted in a temperature chamber held at 55°C. All other cells were cycled at room temperature within the Argon-filled glovebox.

## 4.3 Results and Discussion

### 4.3.1 Interface Characterization

To demonstrate the importance of eliminating carbon, as well as the passivating nature of the Si-SSE interface, the SEI products as well as the extent of SSE decomposition were characterized and quantified with and without presence of carbon additives. While Li metal is typically used as the counter electrode in liquid electrolyte studies, it is highly sensitive to pressure and temperature conditions in ASSBs and exhibits a low critical current density, making it unsuitable in our system.<sup>209-210</sup> Thus, NCM811 was instead chosen as the counter electrode, allowing direct evaluation of  $\mu\text{Si}$  in a full cell. To prepare the lithiated  $\mu\text{Si}$  electrode, two  $\mu\text{Si}$ -SSE-NCM811 cells were assembled (with and without 20 wt% carbon additives). Figure 4.3a shows the voltage profiles of both cells during the first lithiation. The cell without carbon shows an initial voltage plateau around 3.5 V, typical of a  $\mu\text{Si}||\text{NCM811}$  full cell. However, the cell with 20 wt% carbon shows a stark difference, with a lower initial plateau at 2.5 V, indicating electrochemical decomposition of the SSE before reaching the lithiation potential above 3.5 V. Previous studies have found that sulfide SSEs reduce at potentials of around 1 V vs  $\text{Li}/\text{Li}^+$ , which agrees with the observations of the different initial voltage plateau when carbon is used.<sup>149</sup> To characterize the SSE decomposition, the electrodes were extracted and analyzed using X-ray diffraction (XRD) and X-ray photoelectron spectroscopy (XPS) to examine the bulk and surface characteristics of the SEI. Figure 4.3b compares the diffraction patterns of the pristine Si-SSE, lithiated Si-SSE and lithiated Si-SSE-carbon interfaces. The lithiated Si-SSE sample retained the crystalline structure of the SSE as well as the unreacted Si, with some signals of amorphous Li-Si manifesting as a hump at around  $20^\circ$ . While some SEI is expected, the low amount formed as the interface is most likely not detectable using this bulk technique. However, in the cell where carbon is used, most of the pristine SSE's diffraction signals are no longer present, indicating severe electrolyte decomposition. During this process, nanocrystalline  $\text{Li}_2\text{S}$  forms as a major electrolyte

decomposition product and is observed as broad peaks appearing at  $2\theta$  angles of around  $26^\circ$ ,  $45^\circ$  and  $52^\circ$ .

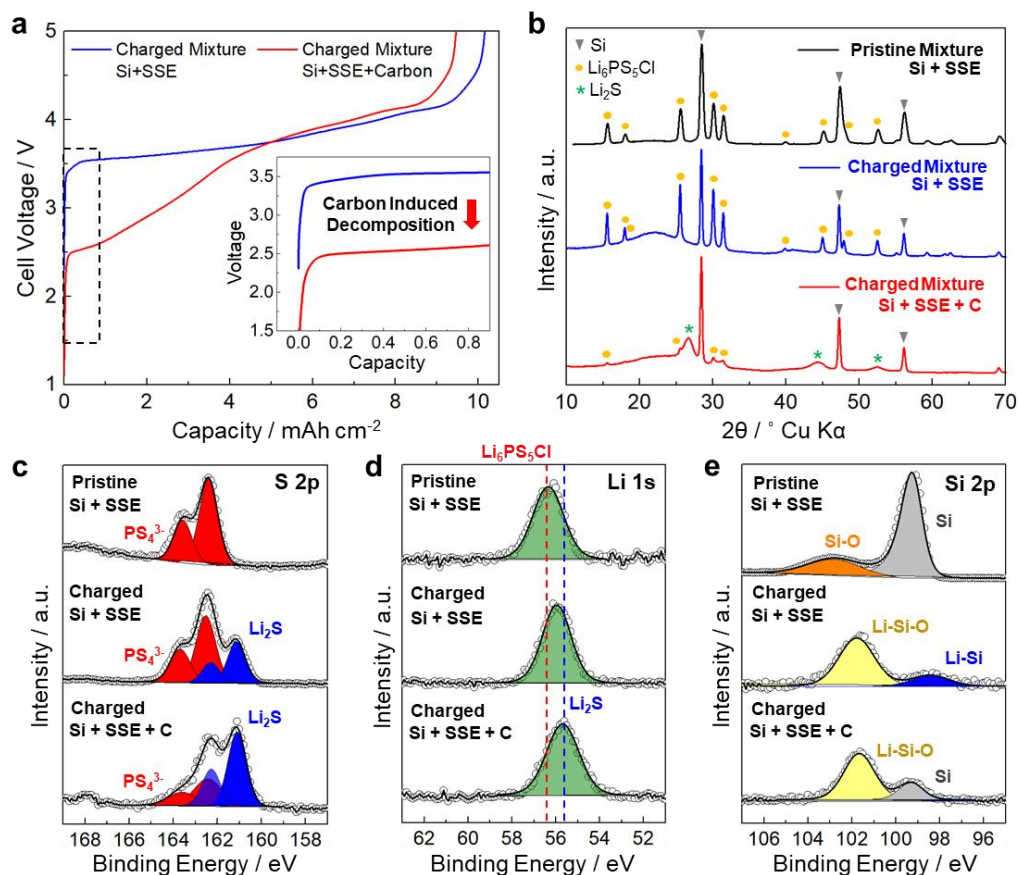


**Figure 4.3.** Carbon effects on SSE decomposition. (a) Voltage profiles of  $\mu\text{Si} \parallel \text{SSE} \parallel \text{NCM811}$  cells with and without carbon additives (20 wt.%), inset shows a lower initial plateau indicating SSE decomposition to form SEI. (b) XRD patterns, and (c-e) XPS spectra of the (c) S 2p, (d) Li 1s and (e) Si 2p core regions, showing increased growth of  $\text{Li}_2\text{S}$  interfacial products when carbon additives are used. Lithiation of  $\mu\text{Si}$  is hindered by excessive SEI growth when carbon is present.

These observations are in agreement with the XPS analysis in Figure 4.3c, where the presence of carbon results in a greater extent of SSE decomposition, as seen by the formation of  $\text{Li}_2\text{S}$  (161 eV) in the S 2p region. Consequently, a larger decrease in peak intensities for the  $\text{PS}_4^{3-}$  thiophosphate unit signals is observed for the electrode containing carbon (Figure 4.3c bottom) compared to the electrode without carbon (Figure 4.3c middle). Although the Li 1s region (Figure 4.3d) is difficult to deconvolute due to the presence of multiple  $\text{Li}^+$  species, a shift toward lower binding energies is observed as a result of reduction of  $\text{Li}^+$  from the pristine SSE. While a smaller

shift is observed in the sample without carbon (Figure 4.3c middle), the peak position for the sample containing carbon is dominated by the  $\text{Li}_2\text{S}$  signals at about 55.6 eV (Figure 3d bottom), reaffirming the previous observation using XRD. In the Si 2p region, a native oxide layer is detected near the surface of the Si particles (Figure 4.3e top). Upon cell charging, this signal shifts to a lower binding energy as a result of lithiation. Interestingly, a peak with a binding energy consistent with Li-Si is found in the sample without carbon, while Si appears to remain unreacted in the sample with carbon. This is likely due to formation of the  $\text{Li}^+$  consuming SEI products, severely limiting the lithiation of the  $\mu\text{Si}$  electrode itself. These results demonstrate the importance of eliminating carbon conductive additives in the  $\mu\text{Si}$  electrode when SSEs are used. With the low-density carbon eliminated from the electrode composite, binder (PVDF) use can be minimized to 0.1 wt% of the anode. This amount was found to be ample to prepare slurries for casting of 99.9 wt%  $\mu\text{Si}$  anodes, as shown in Figure 4.4 below. This electrode was then used for all subsequent interface quantification analysis.

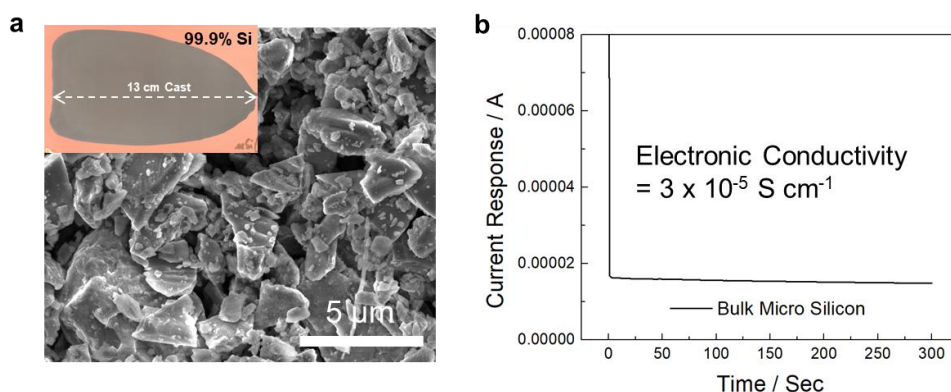


**Figure 4.4** (a) Scanning electron microscopy image of  $\mu\text{Si}$  cast used in this work. Inset shows digital image of the 99.9 wt%  $\mu\text{Si}$  cast. (b) DC polarization of bulk  $\mu\text{Si}$  electrode, showing electronic conductivity of  $3 \times 10^{-5} \text{ S cm}^{-1}$ .

### 4.3.2 Quantification of SEI Components

Fundamental challenges of Si anodes in conventional liquid electrolyte-based cells include the continuous formation of SEI and accumulation of trapped Li-Si during cell cycling. While capacity fade can be detected as a function of coulombic efficiency (CE%) losses, it is difficult to



accurately deconvolute contributions from the SEI or trapped Li-Si respectively. In previous studies, titration gas chromatography (TGC) has been effectively employed to quantify SEI and dead Li growth in Li metal batteries.<sup>49</sup> Here, TGC is applied to quantify SEI growth and ascertain its passivating and stable nature. As TGC experiments are destructive in nature, each data point is extracted from separate individual cells. Five  $\mu\text{Si}||\text{SSE}||\text{NCM811}$  full cells were assembled and cycled from 1 to 5 cycles respectively (Figure 4.5a). After cycling, the cathode was removed from each cell, and the remaining Li-Si anode was fully reacted with anhydrous ethanol to generate  $\text{H}_2$  gas products in a sealed vial. The  $\text{H}_2$  gas was then extracted and quantified using the TGC method, allowing the quantification of the active  $\text{Li}^+$  present in the cycled sample. The difference between the CE% losses and the quantified  $\text{Li}^+$  allows quantification of the SEI formed. Details of the TGC method can be found in the supplementary information. The amounts of SEI accumulated, active  $\text{Li}^+$  from Li-Si, sum of cumulative losses, and total cumulative capacities are plotted in Figure 4.5b. After the 1<sup>st</sup> cycle, the total amount of SEI formed was found to be 11.7% of the cell's capacity, and this amount increases slightly to 12.4% in the 2<sup>nd</sup> cycle. In the subsequent cycles, both the accumulated SEI as well as the active  $\text{Li}^+$  were found to remain stable and relatively unchanged, indicating interface passivation that prevents unwanted continuous reaction between Li-Si and the electrolyte. As the formation of SEI also results in impedance growth, electrochemical impedance spectroscopy (EIS) was conducted on the full cell over 30 cycles. The voltage profiles are shown in Figure 4.5c. From the pristine state in Figure 4.4d, an initial increase in impedance is observed after the 1<sup>st</sup> cycle as a result of the initial SEI formation, an observation in agreement with the TGC measurements. The impedance then remains stable over the subsequent 30 cycles, indicating that the SEI is no longer growing after the first cycle.

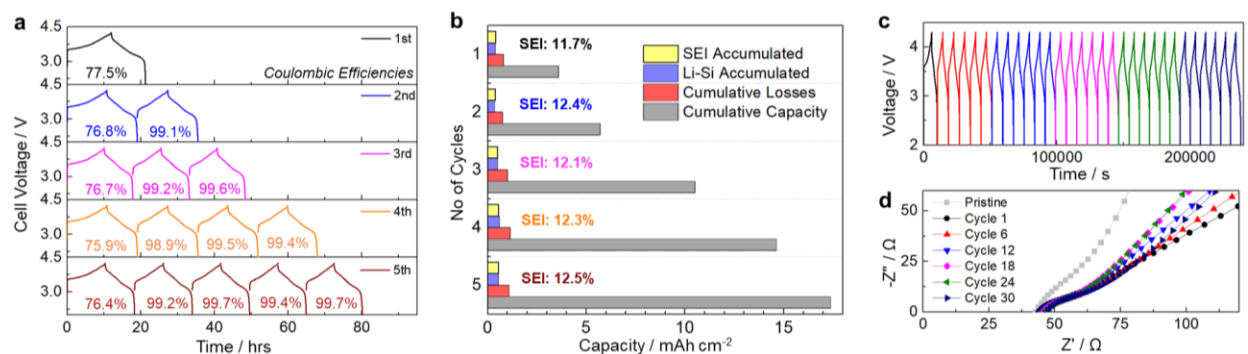


**Figure 4.5.** (a) Voltage profiles of full cells used in titration gas chromatography (TGC) experiments. (b) Quantified Li-Si and SEI amounts relative to cell capacity. (c) Voltage profile of full cell used for EIS, and (d) Nyquist plots for different cycle numbers showing limited impedance growth.

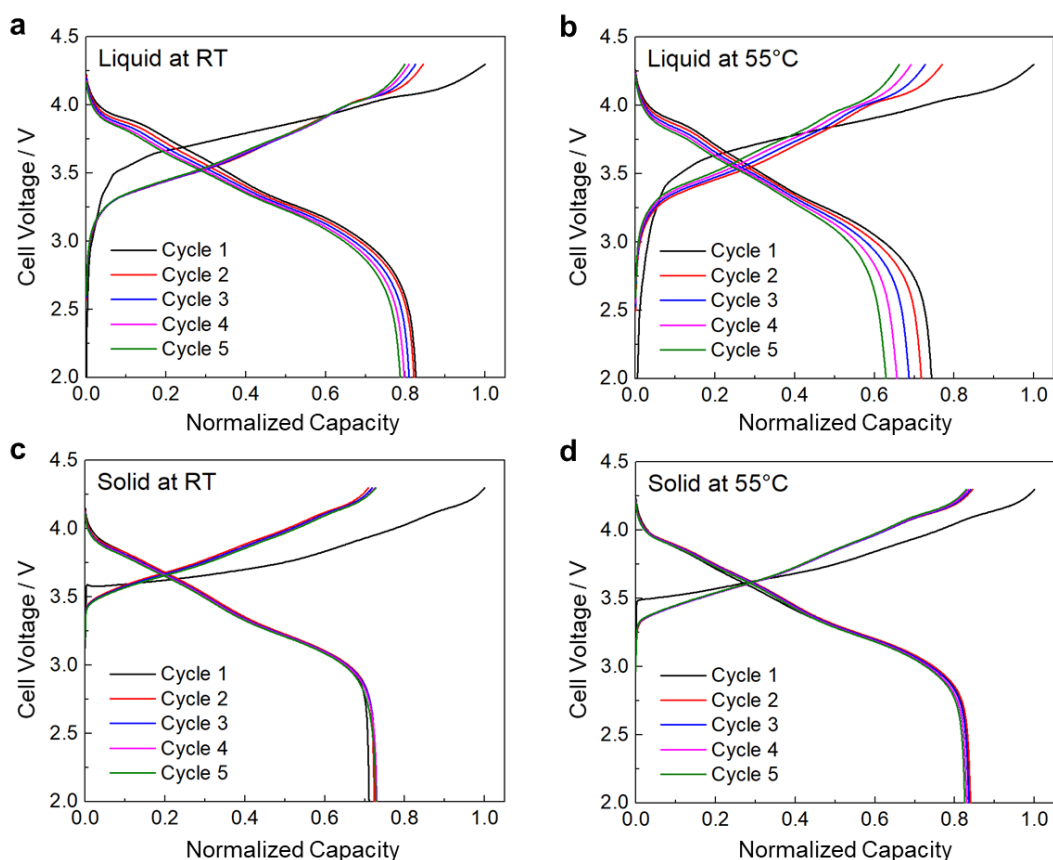


**Figure 4.6.**  $\mu$ Si - SSE - NCM811 full cells voltage profiles at room temperature and 55°C using (a) liquid electrolyte at room temperature, (b) liquid electrolyte at 55°C, (c) solid electrolyte at room temperature, (d) solid electrolyte at 55°C.

The passivating nature of the SEI is not only important to prevent impedance growth but is also vital to extend the calendar life of Si based anodes. In conventional liquid-based cells, lithiated Si is known to undergo parasitic reactions with the liquid electrolytes (Figure 4.6a). Such

unwanted reactions are worsened at elevated temperatures where fast capacity decay is observed (Figure 4.6b), making it unsuitable for long term storage or operation under warmer environments. On the other hand, the use of SSEs, owing to their passivating interfaces, prevents such side reactions from occurring, allowing a high reversibility at both room and elevated (55°C) temperatures as shown in Figure 4.6c & d. To further illustrate the detrimental effects of elevated temperature on Si anodes in liquid-based cells,  $\mu\text{Si}||\text{Liquid}||\text{NCM811}$  and  $\mu\text{Si}||\text{SSE}||\text{NCM811}$  full cells were fully charged and allowed to rest for up to 3 days before discharge. Figure 4.7a & b shows that while capacity fade is seen in the liquid cells and aggravated by elevated temperatures, the cells using SSEs were able to retain most of their capacity after resting at 55°C. To better illustrate this effect, a self-discharge test was performed on both cell configurations to examine their voltage decay after being fully charged. At room temperature, the SSE cell's voltage stabilized after a few hours, while the liquid cell's voltage continued to drop steadily over the next 100 hours (Figure 4.7c). At 55°C, the difference is even more pronounced: the SSE cell's voltage plateaus at about 4.05 V, while the liquid cell's voltage drops more dramatically to 3.85 V over 100 hours (Figure 4.7d). These observations highlight the importance of designing a stable and passivating interface between the Si anode and electrolyte system used.

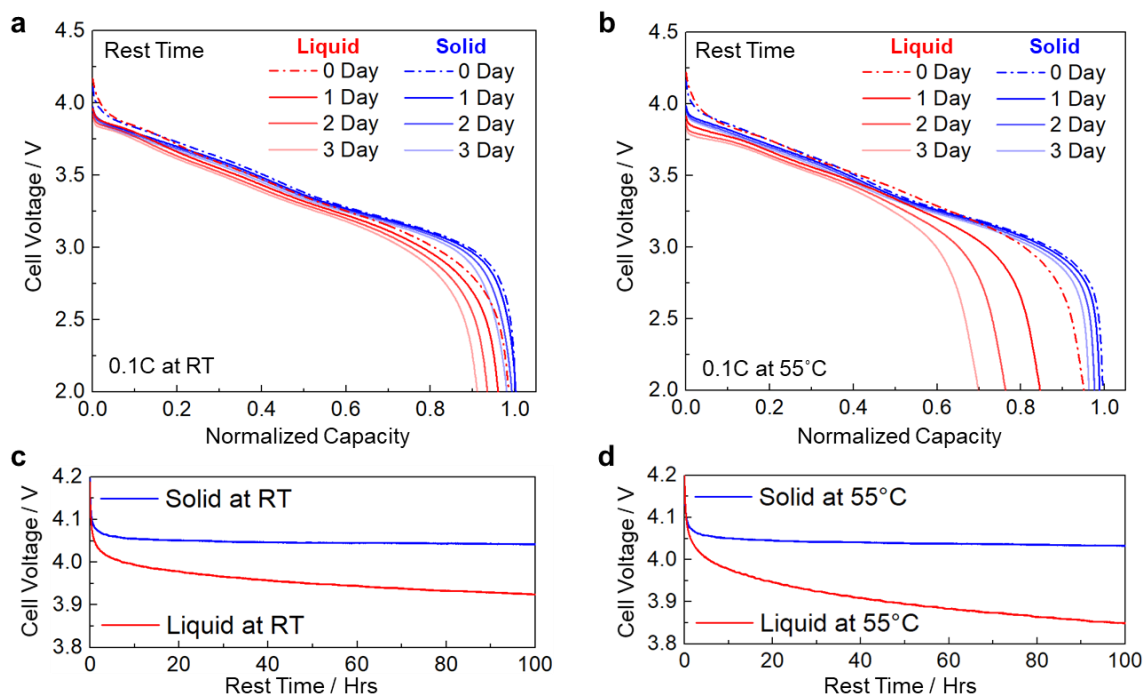


**Figure 4.7.**  $\mu\text{Si}$  - NCM811 full cells voltage profiles at room temperature and 55°C using (a) liquid electrolyte at room temperature, (b) liquid electrolyte at 55°C, (c) solid electrolyte at room temperature, (d) solid electrolyte at 55°C.

### 4.3.3 Morphological Evolution

As discussed in the previous section, the interfacial contact area in the Si-ASSB cell configuration only occurs along a 2D plane between the SSE layer and the 99.9 wt%  $\mu\text{Si}$  electrode. Unlike liquid electrolyte-based cells, where the liquid infiltrates the pores of the electrode and form a SEI that encompasses each  $\mu\text{Si}$  particle,  $\mu\text{Si}$  particles in the SSE cell remain in direct contact with each other. This allows for fast diffusion of  $\text{Li}^+$  and transport of  $e^-$  throughout the electrode, unhindered by any electronically insulative components such as SEI or electrolyte, as illustrated in Figure 4.2.

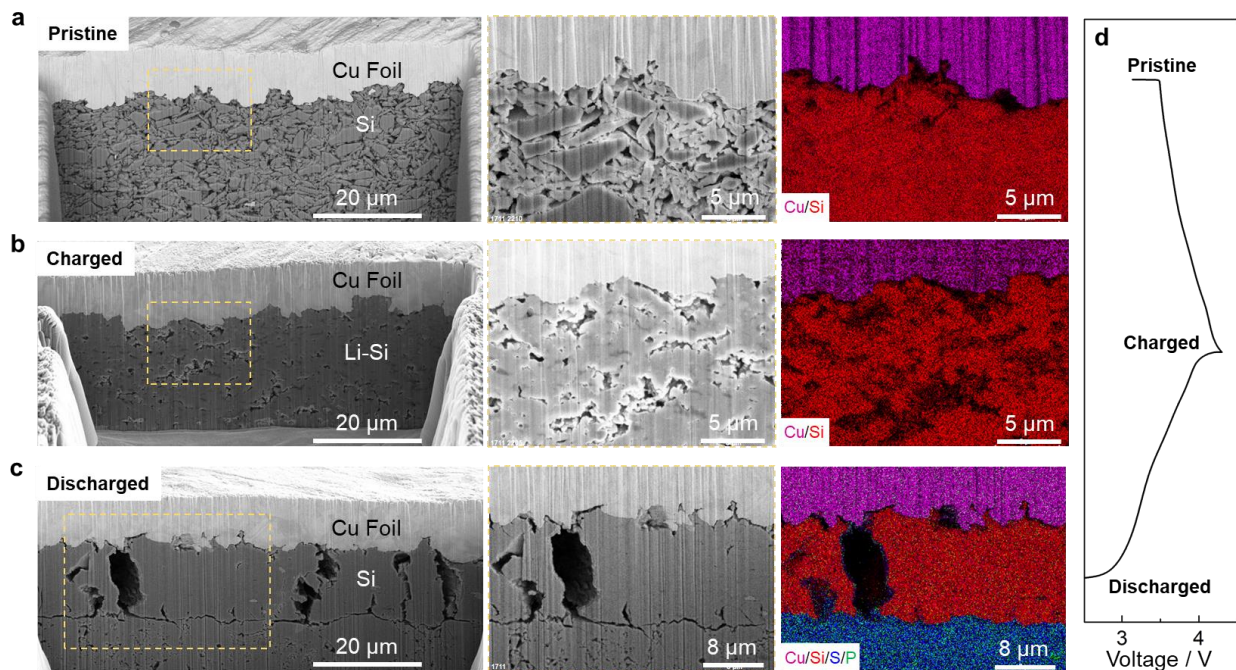


**Figure 4.8.** Visualizing lithiation and delithiation mechanism of 99.9 wt% Si anodes using focused ion beam (FIB) and energy-dispersive X-ray spectroscopy (EDS) imaging. (a) Pristine porous microstructure of  $\mu$ Si electrode. (b) Charged state with densified interconnected Li-Si structure. (c) Discharged state with void formation between large dense Si particles. Yellow dotted box represents enlarged porous regions of interest for each sample. (d) Reference voltage profile of the full cell charge and discharge.

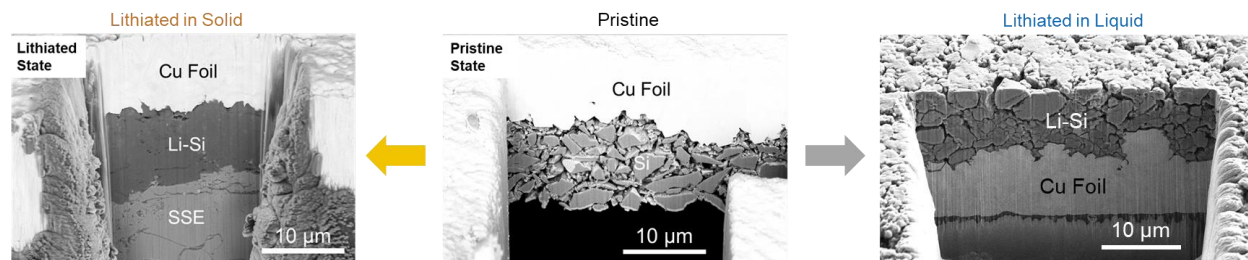


**Figure 4.9.** SEM cross section images of 99.9%  $\mu$ Si electrodes at the pristine and lithiated states using a solid and liquid electrolyte. A lower loading of about  $2 \text{ mAh cm}^{-2}$  is used to image the entire electrode due to the limited milling depth achievable with the FIB tool.

Figure 4.8 shows a cross-section scanning electron microscopy (SEM) image prepared by focused ion beam (FIB) at the pristine, charged and discharged states of the  $\mu$ Si||SSE||NCM811 full cell. At the pristine state in Figure 4.8a, discrete  $\mu$ Si particles are observed, with sizes ranging between 2 and 5  $\mu\text{m}$ . Despite the initial calendaring pressure of 370 MPa used, the electrode exhibits porosity of about 40% due to the high yield strength of elemental Si that prevents deformation during calendaring. After lithiation and volume expansion in Figure 4.8b, the electrode becomes densified, with the majority of pores disappearing between the initial

pristine  $\mu\text{Si}$  particles. More importantly, the boundaries between separate  $\mu\text{Si}$  particles have entirely vanished. An enlarged view of the more porous region shows that the entire electrode has become an interconnected densified Li-Si alloy. After delithiation and volume contraction (Figure 4.8c), the  $\mu\text{Si}$  electrode did not revert to its original discreet micro-particle structure but instead forms large particles between the SSE layer and the copper current collector. Large voids are also formed between these particles. Energy-dispersive X-ray (EDS) imaging confirms that the pores are indeed voids, with no evidence of SEI or SSE present between each delithiated particle. The charge and discharge voltage profiles are displayed in Figure 4.8d for reference. This morphological behavior is a stark contrast to morphological changes of  $\mu\text{Si}$  particles in liquid electrolyte systems. In liquid cells, as SEI formation throughout the electrode prevents direct contact and chemical/electrochemical reactions between  $\mu\text{Si}$  particles, the particles remain isolated and separate from each other during lithiation and undergo volume expansion during cell cycling (Figure 4.9). However, without permeation of SSEs into the pores of the  $\mu\text{Si}$  electrode, lithiated Li-Si can remain in direct contact with unreacted  $\mu\text{Si}$ , allowing progressive lithiation and alloying of the entire electrode (Figure 4.2).

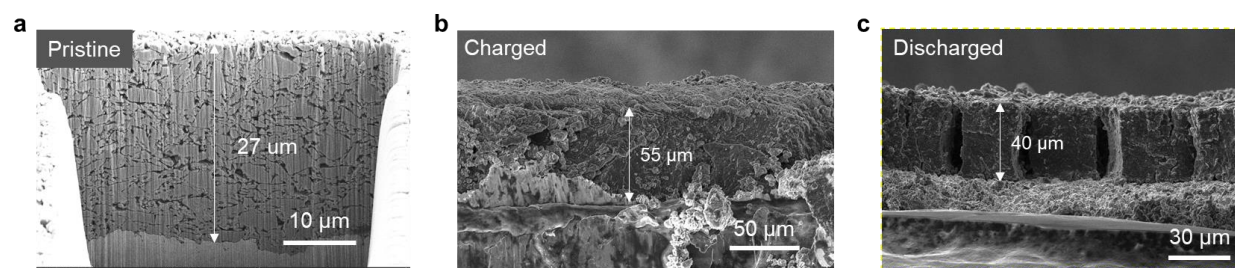


**Figure 4.10.** SEM cross section images of  $\mu\text{Si}$  anode electrode with  $\sim 3.8 \text{ mg cm}^{-2}$  mass loading. (a) Pristine electrode of  $27 \mu\text{m}$  in thickness, with a porosity of 40%. (b) Charged state showing dense Li-Si layer formation of  $55 \mu\text{m}$  in thickness. (c) Discharged state of  $40 \mu\text{m}$  in thickness showing void formation between large silicon particles. All three electrodes were punched from the same batch. Calculated porosities are found in Table S1.

This unique chemo-mechanical behavior of the Li-Si alloy has been previously reported in literature studies on porous Si thin film ASSBs using sulfide SSEs as well, where initial porosity incorporated into the pristine Si thin film electrode was found to be able to accommodate volume

expansion during lithiation to some extent.<sup>195, 211</sup> However, given the large volume expansion expected in  $\mu\text{Si}$  particles (>300%), the 40% porosity found in the pristine electrode is insufficient to fully accommodate this expansion, and thickness changes along the z-axis are still expected. To visualize thickness growth as well as determine porosity changes during lithiation and delithiation,  $\mu\text{Si}$  electrodes with mass loadings of  $\sim 3.8 \text{ mg cm}^{-2}$  were used in full cells with N/P ratio of 1.1 and their thickness changes during cycling measured using the FIB/SEM cross-section. At the pristine state, a thickness of  $\sim 27 \mu\text{m}$  was measured (Figure 4.10a), and after lithiation to  $\text{Li}_{3.35}\text{Si}$ , the thickness increased to  $\sim 55 \mu\text{m}$  (Figure 4.10b). This increase falls short of the expected >300% growth commonly reported in literature on Si anodes<sup>182</sup>, indicating that a significant decrease in porosity must occur. To rationalize this, expected thicknesses vs porosities were calculated in Table 4.1, which shows a low resulting porosity (<10%) of the  $\sim 55 \mu\text{m}$   $\mu\text{Si}$  electrode after lithiation.

**Table 4.1.** Expected electrode layer thickness vs relative density at the pristine, charged and discharged states. Thick electrodes were used in the calculations to reduce measurement error. Asterisks\* indicate approximate observed thicknesses measured with SEM imaging.

Density	100%	90%	80%	70%	60%	50%	mAh / cm <sup>2</sup>
Pristine / $\mu\text{m}$	16.3	18.1	20.4	23.3	27.2*	32.6	0
Charged / $\mu\text{m}$	52.2	58.0*	65.3	74.6	87.0	104.4	12.2
Discharged / $\mu\text{m}$	29.4	32.6	36.7	41.9*	48.9	58.7	3.05

This agrees with the observations made in Figure 4.8, where significant densification is observed compared to the pristine state. After delithiation (Figure 4.10c), a thickness of  $\sim 40 \mu\text{m}$  was measured, with a porosity of  $\sim 30\%$  calculated using the same approach. The lower porosity at the delithiated state compared to the pristine 40% is expected as some  $\text{Li}^+$  remains in the anode of the full cell (Figure 4.5b). Despite the relatively large thickness and porosity changes of the anode during cycling, the lithiation and delithiation was found to be highly reversible over a wide range of conditions as discussed in the subsequent section, contrary to observations made in

liquid based Si cells, where changes in porosity and specific surface area are widely known to be detrimental to cell performance.<sup>182-183</sup> This suggests that the mechanical properties of the Li-Si and SSE have a crucial role in maintaining the integrity of the interfaces as well as retaining conformal contact with the anode in order to facilitate Li<sup>+</sup> diffusion. Any loss of contact area between the anode electrode and the SSE would result in loss of Li<sup>+</sup> diffusion pathways, resulting in impedance growth or Li-plating resulting from the large overpotentials formed. While contact losses are less likely during lithiation, where volume expansion occurs, it is an important consideration during delithiation. However, despite volume shrinkage, good contact is still maintained between the SSE layer and the porous structure of the delithiated Li-Si (Figure 4.8c). This indicates that some degree of Li-Si deformation occurred during cell cycling under a uniaxial stack pressure of 50 MPa used. While pristine  $\mu$ Si did not deform even under large pressures of 370 MPa, existing reports found that both young modulus as well as hardness of Li-Si alloys decreases significantly as a function of lithiation, with a modulus reaching as low as 12 GPa for Li<sub>3.75</sub>Si, resulting in mechanical properties more similar to metallic Li (modulus of 8 GPa) than pristine  $\mu$ Si (modulus of 92 GPa).<sup>212-215</sup> Given that metallic Li was found to achieve sufficient deformation and mechanical contact with SSEs under stack pressures of 5 to 7 MPa<sup>210, 216</sup>, it can be expected that Li-Si also undergo sufficient deformation during cell cycling under 50 MPa, maintaining the conformal contact with the SSEs used here. Naturally, as pressure is only applied in the z-axis, volume shrinkage would result in pore formation in directions parallel to the electrode during delithiation, an observation also reported in other Si thin film studies.<sup>195</sup> As the interfacial contact is maintained along the 2D plane between the SSE and the anode (Figure 4.8), there is no generation of new anode surfaces exposed to the SSE where further SEI grows, enabling high reversibility of the lithiation and delithiation process.

#### **4.3.4 Electrochemical Performance**



To further investigate electrochemical performance of the 99.9 wt%  $\mu$ Si anode in a full cell, performance metrics such as current density, operating temperature, areal capacity as well as cycle life were evaluated. While Li metal-based ASSBs offer high energy densities and have demonstrated long cycle life with 0% excess Li,<sup>217</sup> they still suffer from low critical current densities, inability to operate at room or low temperature, often requiring elevated temperatures during cell charging to avoid cell short as a result of dendrite formation.<sup>218-219</sup> Likewise, while Si anodes in liquid electrolyte cells can exhibit high rates of charge at room to low temperature, their reversible areal capacities in full cells remain low due to inability to achieve high Si loadings in the anode composite electrode.<sup>220-221</sup> Adopting a Si-ASSB cell configuration would overcome both of these shortcomings simultaneously. To test the  $\mu$ Si in full cells, a high loading NCM811 cathode was prepared using a dry electrode process (Figure 4.12), where Polytetrafluoroethylene (PTFE) was used as a binder to achieve thick electrodes. These electrodes were characterized using X-ray computed tomography experiments and compared with slurry casted ones. Unlike conventional slurry cast electrodes, the dry process is able to achieve improved electrode homogeneity as well as higher packing density. Electrode thicknesses of up to 240  $\mu$ m were fabricated while retaining homogeneous distribution of NCM811 cathode as well as conductive carbon fiber (VGCF) within the SSE composite. The dry processed cathode composites were then paired against the  $\mu$ Si anodes with an N/P ratio of 1.1 in full cells. While higher N/P ratios reduced the likelihood of Li plating and cell short, it was found to deliver lower average CE% compared to lower N/P ratios, thus N/P ratios were kept at 1.1 for all cells.

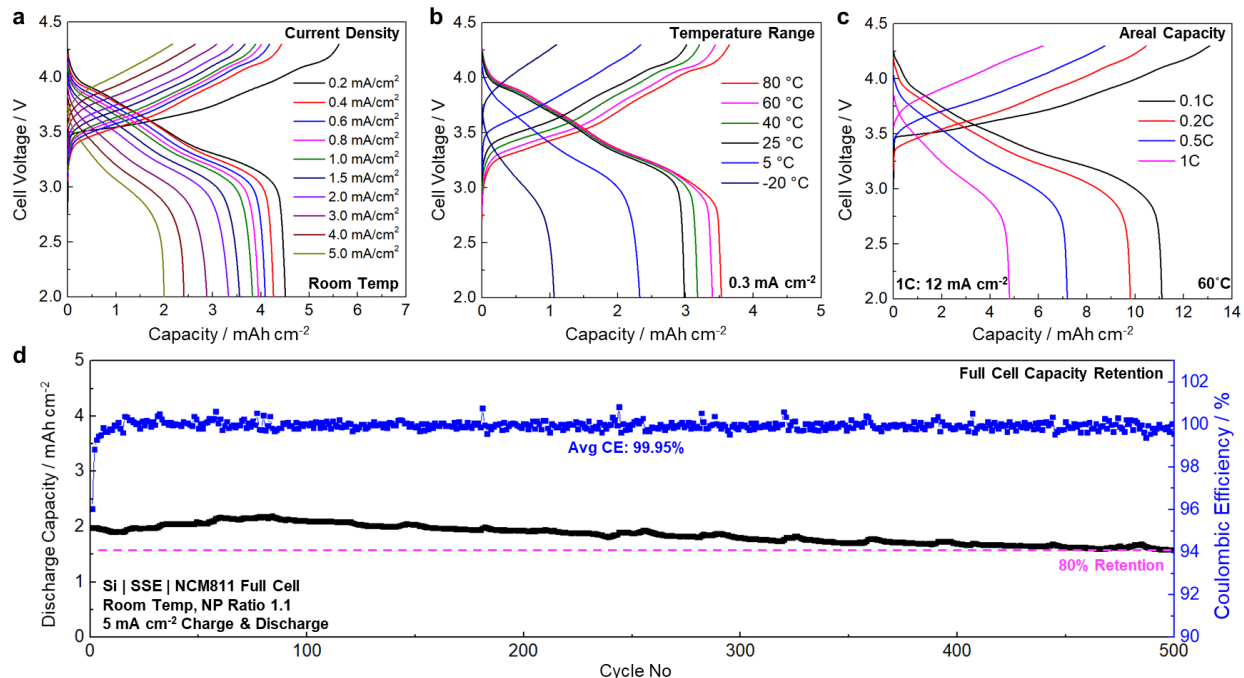


**Figure 4.11.**  $\mu\text{Si}||\text{SSE}||\text{NCM811}$  full cell performance: (a) High current densities at room temperature, (b) Wide operating temperature ranges under  $0.3 \text{ mA cm}^{-2}$ , (c) High areal capacities, (d) Extended cycle life at room temperature, demonstrating overall robustness of ASSB using 99.9 wt%  $\mu\text{Si}$  anodes. All cells were tested under similar conditions for charge and discharge between 2.0-4.3V.

Figure 4.11a shows the room temperature galvanostatic cycling, where current is gradually increased from  $0.2 \text{ mA cm}^{-2}$  to  $5 \text{ mA cm}^{-2}$  for both charge and discharge operation. No evidence of cell short occurs even up to  $5 \text{ mA cm}^{-2}$  at room temperature, significantly higher than the typical room temperature critical current density of Li metal ASSBs reported in the literature.<sup>209-</sup><sup>210</sup> The cell was then allowed to continue cycling at the same conditions to evaluate its cycle life. In Figure 4.11b, a full cell was charged and discharged over a temperature range between  $-20^\circ\text{C}$  to  $80^\circ\text{C}$  using a moderate current density of  $0.3 \text{ mA cm}^{-2}$ . As temperature increased, the cell's capacity utilization increased as well. While the cell polarization increases dramatically at lower temperatures, likely due to Arrhenius behavior of  $\text{Li}^+$  diffusion within the SSE, the cell does not exhibit any sign of shorting at temperatures as low as  $-20^\circ\text{C}$ . From Figure 4.11c, a cell with a cathode sized to  $12 \text{ mAh cm}^{-2}$  was fabricated in order to evaluate high areal loading  $\mu\text{Si}$  electrodes. To overcome the bulk impedance of the thick cathode electrode, the full cell was operated at  $60^\circ\text{C}$  to enhance  $\text{Li}^+$  diffusion kinetics. Under current rates of 0.1C ( $1.2 \text{ mA cm}^{-2}$ ), the  $\mu\text{Si}$  anode was

found to deliver reversible capacities of more than 11 mAh cm<sup>-2</sup>. Under continuous cycling at 1C (12 mA cm<sup>-2</sup>), the  $\mu$ Si anode delivers stable reversible capacity of more than 4 mAh cm<sup>-2</sup> (Figure 4.12d). As room temperature charge and discharge remains to be the ideal condition for ASSB operation, cycle life of the  $\mu$ Si||SSE||NCM811 full cell was evaluated using a current density of 5 mA cm<sup>-2</sup> at room temperature as shown in Figure 4.11d. The cell was found to achieve a capacity retention of 80% after 500 cycles and an average coulombic efficiency of 99.95%. This capacity fade likely occurs as a result of cathode impedance growth over time resulting from contact losses and cathode interfacial growth.<sup>222-223</sup> In order to achieve longer cycle life, further improvements can be made to engineer the interface and chemo-mechanical properties of the cathode||SSE interface. Nonetheless, the electrochemical results shown above reaffirm the effectiveness of the sulfide-based SSE approach to enable 99.9%  $\mu$ Si anodes capable of operating at high current densities, under a wide temperature range, with high areal loadings as well as with a long cycle life and calendar life.

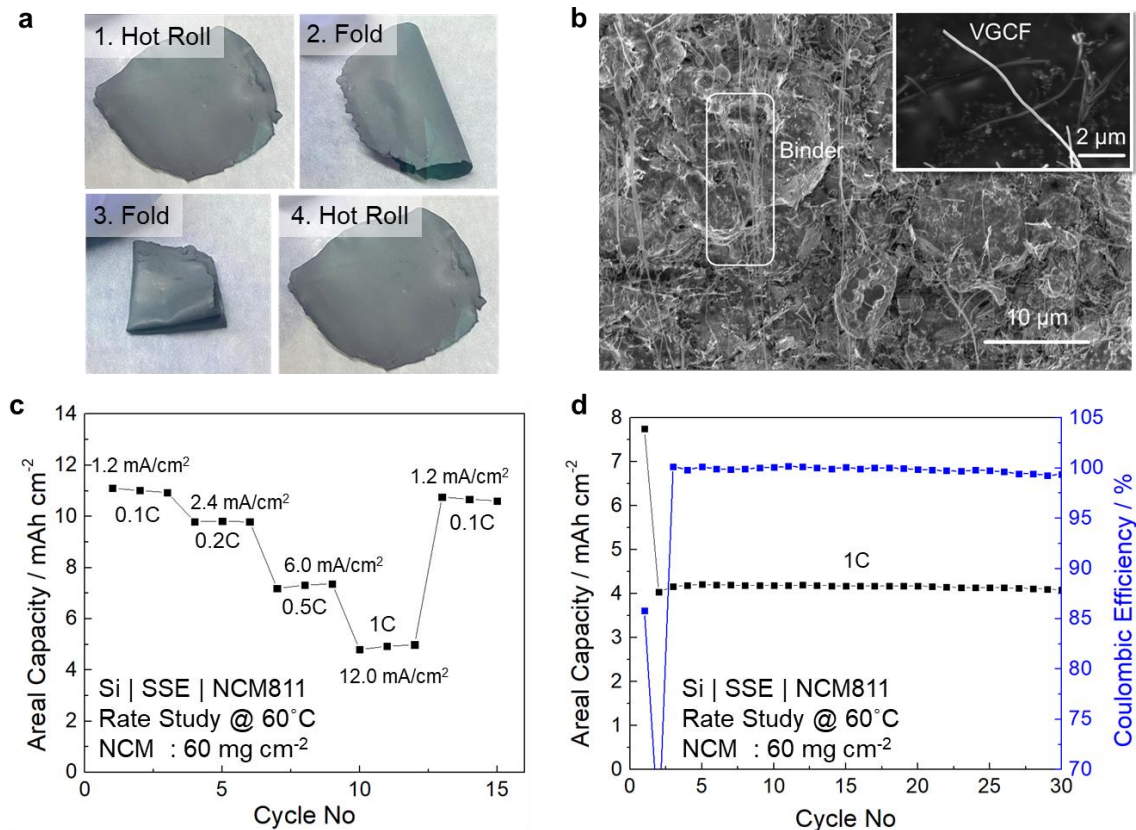


**Figure 4.12.** Dry electrode processing for cathode to achieve high loading. Cathode composition: 80 (NCM) : 20 (SSE) : 3(VGCF): 0.5 (PTFE) in weight. (a) Digital images of hot rolling and folding process. Sequence is repeated until target thicknesses are achieved. (b) SEM image of dry processed cathode showing homogenous distribution of binder and VGCF. (c) Rate performance of 11 mAh cm<sup>-2</sup> Si-NCM811 full cell with silicon anode at 60°C. (d) Extended Si-NCM811 full cell cycling at 1C.

#### 4.4 Conclusion

Through adoption of a sulfide-based SSE system, carbon-free 99.9 wt%  $\mu\text{Si}$  anode electrodes can be enabled in ASSBs. The Si-ASSB cell configuration offers several benefits over the conventional liquid electrolyte system, primarily through the utilization of the stable anode interfaces formed. As the SSE does not permeate throughout the  $\mu\text{Si}$  anode electrode, the interfacial contact layer is maintained along a 2D plane between the SSE separator and the anode electrode. This allows  $\text{Li}^+$  and  $\text{e}^-$  diffusion throughout the electrode and prevents continuous SEI growth and trapped Li-Si formation. Qualitative characterization using XRD and XPS, along with quantification of lithium losses using TGC, demonstrated the passivating nature of SEI formed. The Si-ASSB system was found to exhibit significantly lower self-discharge rates compared to liquid systems under room and elevated temperatures (55°C). FIB-SEM cross section imaging

revealed the morphological changes of the 99.9 wt%  $\mu\text{Si}$  anode electrode, showing the disappearance of interparticle boundaries during lithiation which is unique to the chemo-mechanical properties of the Li-Si alloys, and the formation of large particles separated by voids during delithiation. Electrochemically, the  $\mu\text{Si}||\text{SSE}||\text{NCM811}$  cell was found to be highly robust, achieving high current densities at room temperature ( $5 \text{ mA cm}^{-2}$ ), wide temperature operation ( $-20$  to  $80^\circ\text{C}$ ) and high areal capacities (up to  $11 \text{ mAh cm}^{-2}$ ) for both charge and discharge operations. The full cell delivered a capacity retention of 80% after 500 cycles with an average CE% of 99.95% without the use of pre-lithiation. Overall, the use of sulfide-based SSEs offers a promising strategy to enable low cost, environmentally benign and robust  $\mu\text{Si}$  particles, and addresses the fundamental interfacial bottleneck in the commercialization of high loading  $\mu\text{Si}$  anode electrodes.

Chapter 4, in full, has been submitted for publication as “Carbon Free High Loading Silicon Anodes Enabled by Sulfide Solid Electrolytes for Robust All Solid-State Batteries” as a research article in Science. Tan, D. H. S.; Chen, Y.-T.; Yang, H.; Bao, W.; Sreenarayanan, B.; Doux, J.-M.; Li, W.; Lu, B.; Ham, S.-Y.; Sayahpour, B.; Scharf, J.; Wu, E. A.; Deysheer, G.; Han, H. E.; Hah, H. J.; Jeong, H.; Chen, Z.; Meng, Y. S. The dissertation author was the first author of this paper, all authors contributed to this work.

## **Chapter 5. Sustainable design of fully recyclable all solid-state batteries**

With the rapidly increasing ubiquity of lithium-ion batteries (LIBs), sustainable battery recycling is a matter of growing urgency. The major challenge faced in LIB sustainability lies with the fact that the current LIBs are not designed for recycling, making it difficult to engineer recycling approaches that avoid breaking batteries down into their raw materials. Thus, it is prudent to explore new approaches to both fabricate and recycle next-generation batteries before they enter the market. Here, we developed a sustainable design and scalable recycling strategy for next-generation all solid-state batteries (ASSBs). We use the EverBatt model to analyze the relative energy consumption and environmental impact compared to conventional recycling methods. We demonstrate efficient separation and recovery of spent solid electrolytes and electrodes from a lithium metal ASSB and directly regenerate them into usable formats without damaging their core chemical structure. The recycled materials are then reconstituted to fabricate new batteries, achieving similar performance as pristine ASSBs, completing the cycle. This work demonstrates the first fully recycled ASSB and provides critical design consideration for future sustainable batteries.

### **5.1 Introduction**

Lithium-ion batteries (LIBs) are often touted to be the key toward unlocking renewable energy technologies in global efforts to reduce carbon footprint and human reliance on fossil fuels.<sup>224</sup> Vast improvements in battery technologies over the past few decades in terms of performance and cost per kWh have resulted in a surge in EV sales and the deployment of large-scale grid storage since 2010.<sup>225-226</sup> Unfortunately, as battery packs from these applications reach their end-of-life, efforts to incorporate sustainable practices in handling these spent batteries have not yet been well-established.<sup>227</sup> While conventional battery recycling technologies such as pyrometallurgy and hydrometallurgy have been explored, they still face limited adoption in the industry largely due to their energy intensive and costly nature.<sup>91, 227</sup> Moreover, the use of toxic

chemicals during these processes increases the complexity and hazards involved in handling large volumes of spent batteries.<sup>91, 93</sup> Although recent studies on improved pyrometallurgical and hydrometallurgical methods reported higher metal recovery rates (> 95%),<sup>228-229</sup> their overall material recovery efficiencies (as a function of the entire cell) remains low due to difficulties in recovering the liquid electrolytes and lithium salts. Crucially, today's batteries are not designed for recycling ease, making it difficult to directly recover the critical materials and embedded value in spent batteries.

To this end, the US Department of Energy's ReCell Center has taken up the mantle, setting out core principles for LIB recycling that involve: 1) batteries designed for recyclability, 2) direct recycling of electrodes, and 3) recovery of more components within the cell.<sup>230</sup> Such guidelines compel researchers and manufacturers to consider battery recyclability beyond material processing or metal recovery and explore means to redesign batteries at the cell to pack level instead, promoting ease of recyclability using cost-efficient and low carbon footprint processes. However, major battery manufacturers still face difficulties in adjusting existing production protocols and have little incentive to improve current designs especially when profit margins are concerned. As such, it would be judicious for researchers in the field to design robust recycling strategies for next generation batteries instead, in order to chart pathways for future manufacturers to become early adopters of sustainable production-to-recycling manufacturing processes. Of the various next-generation batteries currently being developed, all-solid-state batteries (ASSBs) are regarded to be a highly promising technology that might see widespread applications in electric vehicles and grid storage.<sup>60, 231</sup> Due to their use of non-flammable inorganic solid-state electrolytes (SSEs), wide operating temperature ranges, and potential for high energy density at lower costs per kWh, ASSBs can offer the right balance of factors needed in large device applications. However, there is still a stark lack of studies on ASSB recycling in the literature to date, providing an opportunity to explore possible pathways for recycling ASSBs.

In this work, we propose a sustainable design and scalable ASSB recycling model. This model demonstrates the recovery and regeneration of both the SSEs and electrodes within the cell in order to minimize waste generation and achieve high recycling efficiencies. We conduct life cycle analysis of our recycling design using the EverBatt model and analyze its energy consumption and greenhouse gas emissions against conventional recycling technologies. We demonstrate the ability to avoid breakdown of the cell components into their core raw materials, instead directly regenerating them into useful formats for reconstitution. Notably, these are done using safe processing methods without any toxic chemicals or a high carbon footprint. The regenerated materials are then reassembled into a new, fully-recycled battery and evaluated against the pristine battery. We show that this process can achieve comparable battery performance to the pristine state and this study provides a promising pathway for large-scale adoption of environmentally-friendly and sustainable battery recycling practices.

## **5.2 Methods**

### **5.2.1 Materials Preparation**

Commercial  $\text{Li}_6\text{PS}_5\text{Cl}$  was obtained from NEI Corporation. XRD and Raman was conducted on the commercial sample to ensure phase purity before use. The  $\text{Li}_6\text{PS}_5\text{Cl}$ - $\text{LiCoO}_2$  electrode composite was prepared by hand mixing  $\text{LiCoO}_2$  (MTI Corporation) and  $\text{Li}_6\text{PS}_5\text{Cl}$  in a 70:30 weight ratio in an agate mortar and pestle for 5 minutes. Commercial lithium metal foil (FMC) was used as the counter electrode; the surface of the foil was first polished and pressed between stainless steel plates to reduce its thickness to 50-100  $\mu\text{m}$  before use. Approximately 2wt% of  $\text{LiNbO}_3$  protective coating was applied onto the  $\text{LiCoO}_2$  particles via the sol-gel method before use.

### **5.2.2 Materials & Electrochemical Characterization**

XRD was conducted using  $\text{Cu K}\alpha$  radiation ( $\lambda=1.54178 \text{ \AA}$ ) over a  $2\theta$  range of  $5\text{-}70^\circ$  with a step size of  $0.01^\circ$ . The ICSD database was used to identify the peaks of  $\text{Li}_6\text{PS}_5\text{Cl}$ . A Perkin Elmer



Raman Station 400F Spectrometer was used to collect Raman spectra intensity values from 134 to 1500  $\text{cm}^{-1}$ . As sulfide-based materials are sensitive to air and moisture, decomposing to form toxic gases such as  $\text{H}_2\text{S}$ , all synthesis and characterization steps were done within an Argon-filled glovebox (MBraun MB 200B,  $\text{H}_2\text{O} < 0.5$  ppm,  $\text{O}_2 < 5.0$  ppm). EIS was performed with a Solartron 1260 impedance analyzer for the pristine and recycled SSE. In an EIS setup, 70 mg of  $\text{Li}_6\text{PS}_5\text{Cl}$  was cold pressed between two titanium current collectors. An applied AC potential of 30 mV over a frequency range from 1 MHz to 0.1 Hz was used for the EIS measurement. The measurements were conducted at room temperature. For cell cycling, the solid electrolyte powders were first pressed at 370 MPa between the titanium plungers enclosed in a polyetheretherketone (PEEK) intermediate holder to form a separator pellet. Next 10 mg of electrode composite powders (70wt%  $\text{LiCoO}_2$ ) was placed on one side of the pellet and once again pressed at 370 MPa. Finally, the lithium metal foil is placed on the opposite side of the pellet and pressed lightly to adhere the foil to the entire cell. The entire cell was then placed in an aluminum jig for mechanical support, a load cell used on one end of the cell to maintain the pressure at 5 MPa throughout the cycling process. Cells were electronically connected via the titanium plungers as the current collectors and cycled using the Neware Battery cycler and analyzed with the BTS9000 software. All cells were cycled under galvanostatic conditions between 2.5-4.2V at 0.1C rate at room temperature with no rest between each cycle.

### **5.2.3 Recycling Methods & Everbatt Model**

After cell cycling, the cell was removed from its aluminum jig and the entire cell pellet was immersed in anhydrous ethanol to dissolve the solid electrolyte, with the undissolved cathode remaining as the solutes. After dissolution, the entire suspension was phase separated using centrifugal methods sealed under inert conditions. After separation, the solution was decanted and the dissolved  $\text{Li}_6\text{PS}_5\text{Cl}$  was recovered using a rotavapor under 80°C and vacuum conditions. The recovered solid electrolyte powder was then annealed at 450°C under vacuum to regain its

ionic conductivity. The ethanol used for the dissolution was recovered via distillation from the rotavapor. For the cathode hydrothermal regeneration, recovered cathodes after decanting were first washed with distilled water and sonicated to remove the CEI before being loaded into a 100 mL Teflon-lined autoclave filled with 80 mL of 4 M lithium hydroxide (LiOH) solution and heated at 220°C for 4 hours. The treated LiCoO<sub>2</sub> powders were washed thoroughly with deionized water before heat treatment under flowing oxygen in a tube furnace to remove impurities. This procedure was designed to simulate scalable conditions where the full ASSB removed from its external pouch packaging can be directly processed for recycling without additional separation into its sub-components. The impacts of battery recycling were modelled by the EverBatt model. The output parameters of energy consumption and environmental emissions were extracted for comparison. Evaluation of recycling energy consumption and emissions for cathode and electrolytes were conducted. The anode is excluded from the modelling considerations. Cathode: Three recycling technologies: direct, hydrometallurgical, and pyrometallurgical cathode recycling are considered in the EverBatt model. Electrolyte: Two recycling technologies, solid electrolyte and liquid electrolyte recycling, are considered in the EverBatt model. Both cases consider direct cathode recycling in order to retain the electrolytes for recycling. Direct cathode recycling is modelled for the electrolyte recycling cases as there would be no remaining electrolyte to be recycled if hydro/pyro processes were used.

## **5.2 Results and Discussion**

### **5.2.1 All Solid-State Battery Recycling Model**

To design a sustainable and practical ASSB recycling model, several criteria needs to be met: (1) Selection of cell chemistries that allow for efficient component separation with minimal steps; (2) Elimination of toxic, expensive, and low-vapor-pressure-organic solvents; (3) Cost-effective recovery of components in the cell beyond just the cathode; and (4) Processes should

be applicable to a variety of cell chemistries.<sup>13</sup> Figure 5.1 illustrates a proposed five-step model that involves: safe cell/pack disassembly, scalable solution processing, component separation, component recovery, and direction regeneration for reuse. For this work, only the sulfide-based  $\text{Li}_6\text{PS}_5\text{Cl}$  (LPSCI) is used as it exhibits a high ionic conductivity ( $> 1\text{mS cm}^{-1}$ ), is interface passivating in nature, and has been reported in several studies to demonstrate promise for future commercialization.<sup>75, 231</sup> Additionally, sulfide-based SSEs including the commonly reported glassy  $\text{Li}_3\text{PS}_4$  or argyrodite  $\text{Li}_6\text{PS}_5\text{X}$  ( $\text{X} = \text{Cl, Br or I}$ ) have been shown to be compatible with scalable solution processing, vital for any successful recycling process.<sup>95, 97, 232-233</sup> Metallic lithium was selected as our representative anode material in this model as its application is widely reported to be the ultimate goal to achieve high energy density ASSBs.<sup>209, 234</sup> In this design, fresh lithium metal foil is used at the anode and is assumed to be fully consumed upon reaching the battery's end-of-life. For the cathode,  $\text{LiCoO}_2$  was used as it is the most common transition metal (TM) oxide-based cathode used in both commercial LIBs as well as ASSBs reported in the literature.<sup>97, 235-236</sup> While the  $\text{Li} | \text{Li}_6\text{PS}_5\text{Cl} | \text{LiCoO}_2$  configuration is used in this study, the processes developed are designed to be applicable to other chemistries as well.

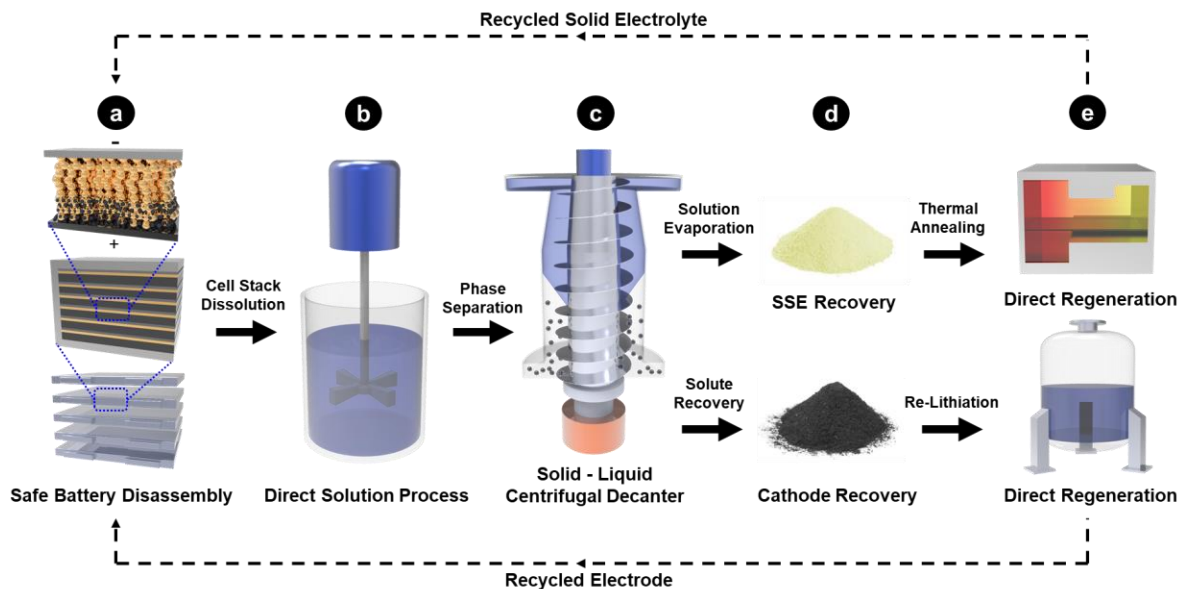


**Figure 5.1.** Schematic of the proposed ASSB recycling procedure at an industrial scale, based on the principles of direct recycling. Cell packaging of the ASSB is first removed before the entire cell stack is processed in a solution without further component separation. Solids and liquids are then separated and recovered for direct regeneration via thermal annealing for the solid electrolyte and direct re-lithiation for the cathode.

Compared to commercial organic liquid-electrolyte based LIBs which can pose significant fire hazards during disassembly, the intrinsic nonflammable nature of ASSBs mitigates such safety hazards during breakdown of large spent battery packs. Upon removal of packaging materials (Figure 5.1a), no further separation of the cell is required, and the full cell undergoes solution processing using a low cost, low-boiling point, and safe solvent such as ethanol (Figure 5.1b). Previous studies have found that polar solvents such as acetonitrile or various alcohols can induce dissolution of sulfide-based SSEs (that comprise of  $PS_4^{3-}$  conductive thiophosphate units) and allow recovery into their original chemical state without chemical degradation.<sup>95, 97, 232-233</sup> The dissolution process will result in a suspension of dissolved SSEs in the solution and the spent transition metal oxide cathodes as the precipitates. The suspension comprising of two phases are then separated using either filtration or gravity-based separation methods such as centrifugal decanting (Figure 5.1c), followed by drying of the solvent to recover the SSE and cathodes respectively (Figure 5.1d). Upon recovery, the SSEs and cathodes are then directly regenerated,

using thermal annealing and chemical re-lithiation respectively, to produce fully recycled materials that can then be used to assemble new ASSBs (Figure 5.1e).

While lithium metal anode is used in this recycling design, it is noted that alternative anode materials have been reported as well, such as anode free, graphite-based and Li-alloy type configurations.<sup>237-239</sup> As treatment and separation of unreacted lithium metal is considerably more complex than graphite and metallic alloys, which can be separated using physical methods, using lithium metal anode in this ASSB recycling design would offer a more conservative approach. In the case where unreacted lithium metal remains, the cell should first be safely discharged to low voltages, ensuring all excess lithium are fully reacted before beginning the recycling process. Alternatively, any trace amounts of lithium remaining can be treated by first pre-processing the cell with heavier alcohols and filtering before the ethanol dissolution step in Figure 5.1b. This eliminates the presence of lithium ethoxide impurities within the SSE solution.

## **5.2.2 Economical & Environmental Impact Analysis**

To evaluate the relative economic and environmental impacts of the ASSB recycling design, the EverBatt model is used to analyze the energy consumption and greenhouse gas (GHG) emissions for various battery recycling processes. Developed by Argonne National Laboratory under the support of the Department of Energy, EverBatt is a publicly available battery recycling cost and environmental impact modelling tool that allows researchers to evaluate the effectiveness of various battery recycling technologies.<sup>240</sup> For recycling processes, EverBatt mainly considers pyrometallurgical, hydrometallurgical and direct recycling routes for both electrolyte and cathode materials. These capabilities are utilized in our ASSB recycling design to evaluate impact of recycling the SSE and cathode when compared to conventional LIBs. It is noted that lithium metal recycling is not within the scope of the EverBatt model but could potentially impact overall energy balance considerations. Likewise, while recycling of graphite and other inactive components such as current collectors are possible and should be encouraged,

these are out of scope for this work (due to the relatively low economic and environmental impact) and will not be included in the energy and GHG analysis.

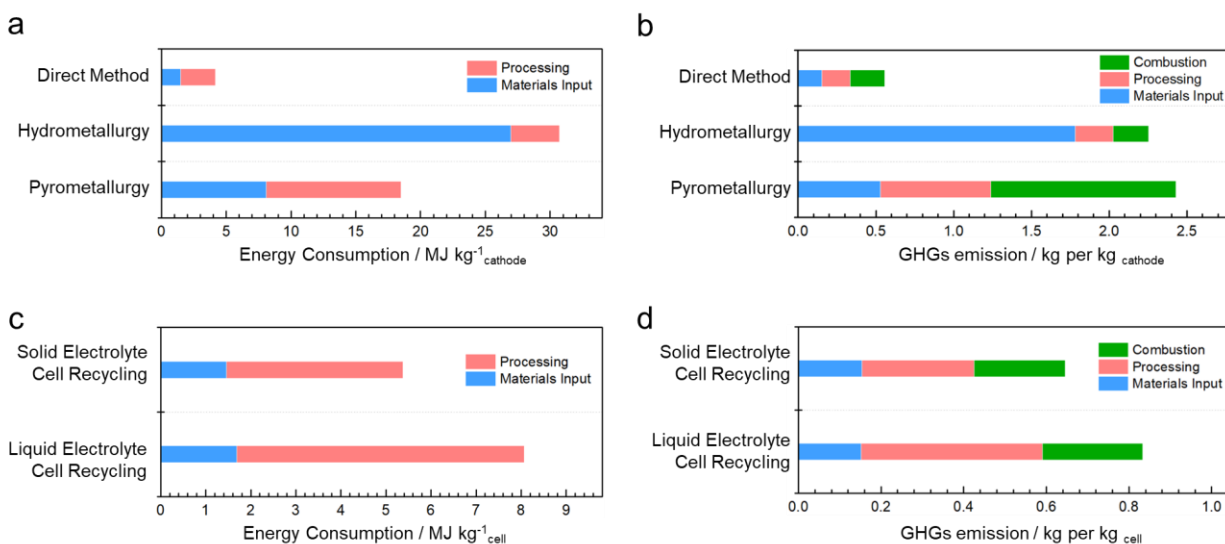


**Figure 5.2.** Energy and environmental impact analysis from upstream processing to the fully recycled state. (a) Total energy consumption and (b) greenhouse gas emission (GHG) comparisons from direct methods, conventional hydrometallurgy, and pyrometallurgy for LiCoO<sub>2</sub> recycling. (c) Energy consumption and (d) greenhouse gases emission comparisons between solid and liquid electrolyte recycling in full cells using solution processing with heat treatment, and super critical CO<sub>2</sub> extraction, respectively.

### 5.2.2.1 Direct Cathode Recycling

For any new recycling strategy to be effective, it must achieve both lower costs and lower GHG emissions than existing processes. This entails the elimination of sophisticated multi-step processes that are both energy intensive and require handling of toxic organic chemicals commonly seen in hydrometallurgy.<sup>91, 229</sup> Combustion of waste and organics, a core component of pyrometallurgy, should also be avoided to minimize GHG emissions and energy consumption.<sup>91, 228</sup> Thus, direct recycling is a promising alternative for recovery and regeneration of spent battery components. Direct recycling of spent cathode materials has been reported in previous studies using hydrothermal re-lithiation or molten eutectic salts to directly regenerate degraded electrodes to their pristine states without breakdown of their core chemical structures.<sup>92, 101, 241</sup> Figure 5.2a compares the relative energy consumption (energy needed to recycle 1 kg of spent LiCoO<sub>2</sub>) of direct recycling compared to pyrometallurgy and hydrometallurgy. The energy required to directly

regenerate cathodes is 78% lower than pyrometallurgical and 86% lower than hydrometallurgical methods, respectively. It is important to point out that these energy values also account for consumption during upstream material processing such as the production of chemicals required for recycling. The large differences in the total energy required stems from a reduced material input during regeneration as major inputs in direct methods only involve lithiation precursors such as LiOH and Li<sub>2</sub>CO<sub>3</sub>. In contrast, large volumes of acids (such as H<sub>2</sub>SO<sub>4</sub>) required in the leaching steps used in hydrometallurgy, and heat energy used in smelters during pyrometallurgy, are major contributors to the high energy usage in these processes. Consequently, this has a direct impact on the amount of GHGs released as seen in Figure 5.2b. Although GHG output from pyrometallurgical recycling is the highest amongst the three methods compared (mainly due to the high combustion output during smelting that releases large amounts of exhaust gas and flue dust), the total amount of GHGs released via hydrometallurgy is merely 3.3% lower. The high amount of GHGs from the materials input component is a result of large amounts of acids needed for leaching (Table 5.1). While the emissions do not come from the leaching process itself, upstream production of GHGs such as CO<sub>2</sub> and SO<sub>x</sub> during the manufacturing of sulfuric acid is the main contributor toward GHGs (Table 5.2). Conversely, direct recycling results in approximately 1/5 of the GHG emissions compared to conventional methods, due to the absence of material or energy consuming processes and non-destructive regeneration methods. However, direct recycling methods also require more delicate sorting processes based on their respective electrode chemistries such as commercially used LiCoO<sub>2</sub>, LiFePO<sub>4</sub> (LFP), Li(Ni<sub>x</sub>Mn<sub>y</sub>Co<sub>z</sub>)O<sub>2</sub> (NMC), Li(Ni<sub>x</sub>Co<sub>y</sub>Al<sub>z</sub>)O<sub>2</sub> (NCA) ( $x+y+z = 1$ ), or other cathode materials. This can be challenging to achieve for third party recyclers who may not have access to complete information on cell chemistries from the original battery manufacturers, making it difficult to both separate and select the appropriate direct regeneration conditions to recycle spent materials. Additionally, direct recycling methods reported in the literature often includes only the cathode while the other cell components

are discarded or not treated. Until more components of the cell are recovered, the recycling efficiency as a function of the entire cell will remain low.

**Table 5.1.** Materials requirements to recycle 1 kg of spent batteries via different recycling technologies.

Material (kg)	Cathode Only without Electrolyte			Full Cell with Electrolyte	
	Pyro-metallurgy	Hydro-metallurgy	Direct Recycling	Liquid Electrolyte	Solid Electrolyte
Ammonium Hydroxide	~	0.031	~	~	~
Hydrochloric Acid	0.210	0.012	~	~	~
Hydrogen Peroxide	0.060	0.366	~	~	~
Sodium Hydroxide	~	0.561	~	~	~
Limestone	0.300	~	~	~	~
Sand	0.150	~	~	~	~
Sulfuric Acid	~	1.080	~	~	~
Soda Ash	~	0.020	~	~	~
Carbon Dioxide	~	~	~	2.200	~
Lithium Hydroxide	~	~	0.014	0.014	0.014
Lithium Carbonate	~	~	0.005	0.005	0.005

**Table 5.2.** Total emissions and breakdown of greenhouse gases (GHGs) to recycle 1 kg of spent batteries via different recycling technologies.

GHG (emissions in grams)	Cathode Only, without Electrolyte			Full Cell with Electrolyte	
	Pyro-metallurgy	Hydro-metallurgy	Direct Recycling	Liquid Electrolyte	Solid Electrolyte
Organics	0.167	0.381	0.108	0.126	0.110
CO	0.550	1.176	0.386	0.467	0.372
NO <sub>x</sub>	1.213	2.440	0.886	1.155	0.907
PM10	0.138	0.211	0.091	0.131	0.107
PM2.5	0.075	0.142	0.076	0.089	0.080
SO <sub>x</sub>	1.740	23.809	0.271	0.920	0.560
Black Carbon	0.018	0.028	0.025	0.028	0.025
Organic Carbon	0.016	0.043	0.023	0.023	0.023
CH <sub>4</sub>	2.444	4.648	0.594	0.959	0.646
N <sub>2</sub> O	0.019	0.038	0.006	0.008	0.006
CO <sub>2</sub>	2,350	2,197	536.5	802.7	624.0
<b>Total GHGs</b>	<b>2,430</b>	<b>2,350</b>	<b>556.7</b>	<b>834.8</b>	<b>645.8</b>



### 5.2.2.1 Electrolyte Recycling

To address these concerns, recent studies have explored the recovery of lithium within the organic liquid electrolytes and salts using supercritical CO<sub>2</sub> extraction, allowing a greater fraction of the spent LIB to be recycled.<sup>7, 94, 242-243</sup> As electrolytes, salts and additives typically make up 10-15% (weight fraction) of the entire cell<sup>91, 244</sup>, their recovery in combination with direct recycling of cathode materials (which typically makes up 25-40% of a cell)<sup>91, 244</sup> offer a promising strategy to harvest a major fraction of the valuable components in spent LIBs and reduce waste generation at the same time. In principle, the enhanced dissolution properties between the liquid and gaseous phase of supercritical CO<sub>2</sub> allows high-yield extraction of organic substances along with any dissolved salts, enabling recovery rates up to 90% of the liquid electrolytes.<sup>242-243</sup> However, due to the additional facilities required to maintain the temperature and pressure conditions, processing energy costs will increase slightly (Figure 5.2c). Nonetheless, overall energy costs and GHG emissions from liquid electrolyte recovery and direct recycling of spent LIBs is still significantly lower than traditional pyrometallurgy and hydrometallurgy methods (Table 5.2).

In our ASSB recycling design, SSE recovery and regeneration are incorporated into the EverBatt model. To recycle Li<sub>6</sub>PS<sub>5</sub>Cl (used in our example), ethanol is employed to dissolve and precipitate the SSE from the composite electrode and separator layers as seen in Figure 5.1. Despite the need to overcome vaporization enthalpies to evaporate and recover ethanol, its high vapor pressure compared to common organic solvents (such as N-Methyl-2-pyrrolidone) significantly reduces the energy requirements needed for processing. This translates into marginal increases in the corresponding emissions compared to when only the cathode is recycled (Figure 5.2d). GHG emissions from ASSB recycling stems from mainly CO<sub>2</sub>, due to electricity use during processing (generated from fossil fuels). The amount of energy required can be further reduced if ethanol is evaporated under vacuum conditions without the use of any heat,

provided ambient temperatures are sufficiently high ( $> 20\text{ }^{\circ}\text{C}$ ) for vaporization. Although not considered in this model, condensation enthalpies can also be reclaimed in large scale industrial processes during ethanol recovery for reuse. Despite the fundamentally different cell chemistries of ASSBs vs. LIBs used in this study, the energy and environmental analysis arising from 1 kg of spent batteries shows the importance of adopting direct recycling methods to lower costs as well as GHG emissions across both types of cells. Furthermore, the incorporation of electrolyte recycling can dramatically improve recycling efficiency as a function of the entire cell, notably with only marginal increases in energy and environmental costs, making it an effective strategy to handle both spent LIBs and ASSBs at their end-of-life.

### **5.2.3 Experimental Validation of ASSB Recycling**

To demonstrate the feasibility of our ASSB recycling model, the structural and electrochemical properties of the SSE and cathode at both the pristine and fully recycled states were experimentally evaluated. As ASSBs are not currently commercially available, pristine ASSBs were fabricated and subsequently recycled after a certain number of defined cell cycles. For this study,  $\text{Li} \mid \text{Li}_6\text{PS}_5\text{Cl} \mid \text{LiCoO}_2$  full cells were assembled and tested at room temperature for 100 cycles before application of the direct recycling strategy. After recovery and regeneration of the SSEs and cathodes, these recovered materials will be reassembled into ASSBs (“fully recycled ASSBs”) and compared against their pristine states in order to evaluate the efficacy of the recycling design.

#### **5.2.3.1 $\text{Li}_6\text{PS}_5\text{Cl}$ SSE Recovery & Regeneration**

Fundamentally, spent bulk SSEs in both the separator layers and cathode composites do not undergo significant chemical degradation even after prolonged cell cycling, with the exception of minor decomposition at the cathode interface.<sup>24, 149</sup> As a result, most of the SSE can be directly recovered without sophisticated re-synthesis. After dissolution in ethanol and precipitation, the

recovered SSE was found to exhibit an ionic conductivity (Table 5.3) of about 1 order of magnitude lower ( $0.11 \text{ mS cm}^{-1}$ ) than its pristine state ( $1.62 \text{ mS cm}^{-1}$ ). This was reported in previous studies to be due to reduced grain sizes and a poor degree of crystallinity in recovered SSEs rather than a result of chemical degradation against the organic solvents used.<sup>97</sup> Reductions in particle size can also be observed after the dissolution process (Figure 5.3a & b). The recovered  $\text{Li}_6\text{PS}_5\text{Cl}$  was then heated under vacuum, and characterized with X-ray diffraction (XRD), Raman spectroscopy, and electrochemical impedance spectroscopy (EIS). From Figures 5.3c and d, both the bulk and local structures of recycled  $\text{Li}_6\text{PS}_5\text{Cl}$  were recovered after the direct regeneration process. An ionic conductivity of  $1.48 \text{ mS cm}^{-1}$  was measured after recycling, which is within the same order of magnitude of its pristine form (Figure 5.3e). Thus, thermal annealing was demonstrated to be effective in regaining the pure phase and the high ionic conductivity of solution processed SSEs.

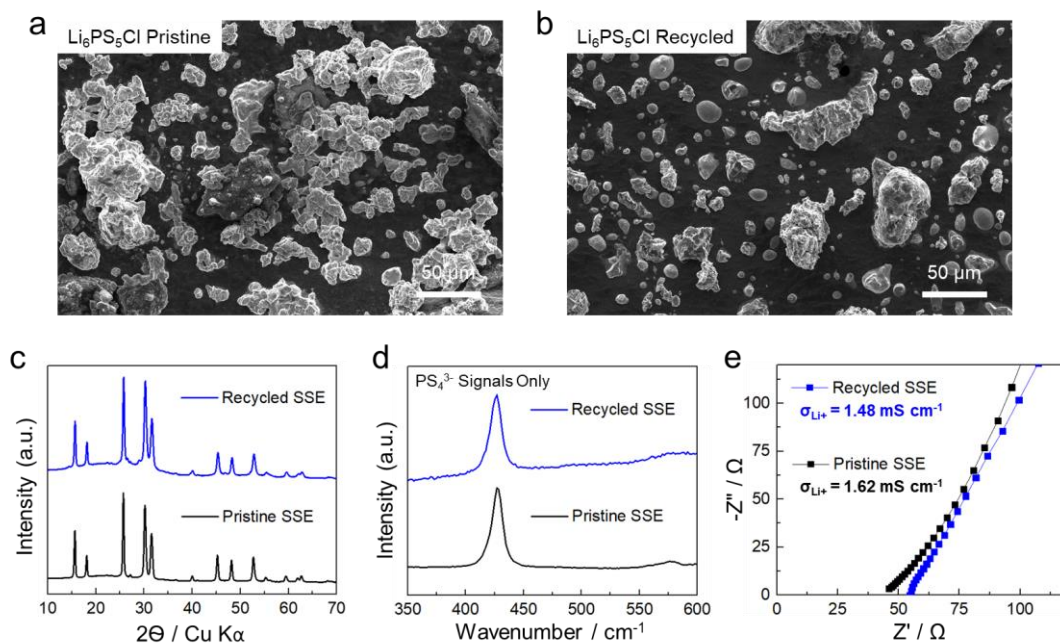


**Figure 5.3.**  $\text{Li}_6\text{PS}_5\text{Cl}$  particles at the (a) pristine state and (b) recycled state. The average particle size of  $\text{Li}_6\text{PS}_5\text{Cl}$  decreased after the solution process. Characterizing  $\text{Li}_6\text{PS}_5\text{Cl}$  solid electrolyte at the pristine and regenerated state. (c) X-ray diffraction patterns showing the retention of the bulk structure. (d) Raman spectra demonstrating the retention of local thiophosphate units. (e) Nyquist plots from impedance measurements indicate the retention of ionic conductivity.

### 5.2.3.2 LiCoO<sub>2</sub> Cathode Direct Recycling

After the phase separation steps described in Figure 5.1, spent cathodes are recovered as precipitates. Using inductively coupled plasma mass spectrometry (ICP-MS), it was found that spent LiCoO<sub>2</sub> contains depleted Li<sup>+</sup> amounts (Table 5.3) compared to the pristine cathode, which has been typically reported on cathodes harvested from cycled conventional LIBs. However, unlike liquid electrolyte-based LIBs, LiCoO<sub>2</sub> cathode particles from ASSBs would also contain cathode-electrolyte interphase (CEI) products deposited on the surface as a result of SSE oxidation during cell cycling (Figure 5.4a). This CEI layer needs to be treated and removed before direct regeneration can be applied to re-lithiate the LiCoO<sub>2</sub> particles. As previous studies have found that the oxidized products of Li<sub>6</sub>PS<sub>5</sub>Cl mainly comprise of elemental S, P<sub>2</sub>S<sub>5</sub> and LiCl<sup>24, 149</sup>, all of which are soluble in or can be physically removed with water, the recovered cathode was surface treated with water before hydrothermal regeneration. It is noted that a LiNbO<sub>3</sub> coating is typically used in cathodes for ASSBs to avoid chemical reactions with SSEs; this coating material is inert to water and is retained after the recycling process. After hydrothermal re-lithiation, ICP measurements found that LiCoO<sub>2</sub> regained its original lithium content and thus became fully regenerated. While solid-state sintering using suitable lithium sources may be equally effective to directly regenerate the cathode, such methods require accurate quantification of its state of decay and lithium source ratio in order to avoid depositing impurities onto the regenerated cathodes. This may be difficult to achieve on the commercial scale where spent batteries from different devices and sources are obtained. Thus, hydrothermal method would be a more robust method that can be applied across cathodes harvested from different cells.

**Table 5.3.** Ionic conductivity of the  $\text{Li}_6\text{PS}_5\text{Cl}$  solid electrolyte and ICP results of the  $\text{LiCoO}_2$  cathode materials at the pristine, cycled, and regenerated states. Ionic conductivity was measured via electrochemical impedance spectroscopy measurements.

State	$\text{Li}_6\text{PS}_5\text{Cl}$ – Conductivity	$\text{LiCoO}_2$ – Li Content
Pristine	$1.62 \text{ mS cm}^{-1}$	$\text{Li}_{1.05}\text{CoO}_2$
Recovered	$0.11 \text{ mS cm}^{-1}$	$\text{Li}_{1.01}\text{CoO}_2$
Regenerated	$1.48 \text{ mS cm}^{-1}$	$\text{Li}_{1.06}\text{CoO}_2$

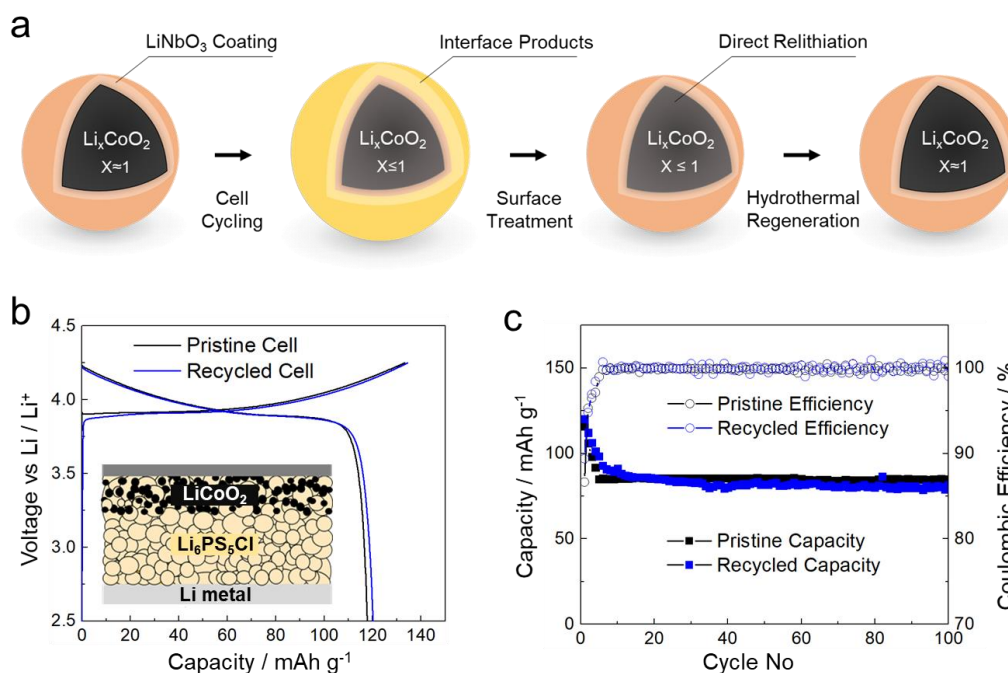


**Figure 5.4.** (a) Schematic of the  $\text{LiCoO}_2$  cathode surface treatment and regeneration process. (b) Voltage profile of the  $\text{Li} | \text{Li}_6\text{PS}_5\text{Cl} | \text{LiCoO}_2$  cell in the pristine and recycled state, with the schematic of the cell setup in inset. (c) Cycle performance of the  $\text{Li} | \text{Li}_6\text{PS}_5\text{Cl} | \text{LiCoO}_2$  cell in the pristine and recycled state. Cells were cycled at room temperature, under a stack pressure of 5 MPa, and at a rate of 0.1C. The typical active mass loading was  $10 \text{ mg cm}^{-2}$ .

### 5.2.4 Electrochemical Performance

To evaluate each recycled component, both regenerated  $\text{Li}_6\text{PS}_5\text{Cl}$  and  $\text{LiCoO}_2$  were used to fabricate new ASSBs using fresh lithium metal foil and cycled under similar conditions as the original cell. Figure 5.4b compares the 1<sup>st</sup> cycle voltage profile of the pristine and the recycled cell. Both cells display comparable 1<sup>st</sup> cycle charge and discharge capacities as well as overall cell polarization, with slight differences which can be attributed to temperature

fluctuations. Cell stack pressures of 5 MPa were used for cycling as it was previously found to enable long cycle life of lithium metal ASSBs.<sup>245</sup> Figure 5.4c shows the capacity retention as well as Coulombic efficiencies with extended cell cycles. Initial capacity fade in both cells is attributed to mechanical contact losses between the SSE and cathode, typical of ASSBs with similar cell configurations. After the initial capacity loss, both cells achieved high capacity retention and average Coulombic efficiencies of > 99.9% after the 5<sup>th</sup> cycle (Figure 5.4c). While these results demonstrate the effectiveness of recycling the spent ASSBs, this has yet to be tested in a full-cell pack with typical commercial-sized capacities (> 2Ah). Thus, it is not clear how multilayer stacked cells (that may contain carbon additives, binders, and other additional components) may influence the recycling approach. Thus, processes would need to be optimized and adjusted to suit the cell configurations of future commercialized ASSBs.

Nonetheless, the recycling principles of separation, recovery, and direct regeneration can also be applied to alternative cell chemistries. Other types of SSEs can be processed with inexpensive and relatively safe solvents such as acetonitrile, water, methanol, and other organic solvents that have high vapor pressure.<sup>246-247</sup> This allows cathode materials to be separated from the dissolved SSEs during recovery. Likewise, direct regeneration methods can be applied to alternative cathodes as well, using either solid-state sintering methods or molten eutectic salts discussed earlier, to enable direct re-lithiation of the NMC cathode (harvested from spent LIBs) under ambient pressure conditions.<sup>101, 248</sup> As spent batteries are generally defined by a 20% loss of reversible capacity, most of the materials within any spent cell should still be in usable condition and thus require only mild regeneration to regain their pristine properties. While lithium metal anodes are consumed in this model, the principles of separation, recovery and regeneration can also be applied other types of anodes such as conventional graphite or next generation silicon anodes as well. Ultimately, direct regeneration of cathodes and recovery of electrolytes are an important and promising method to reduce both

energy consumption and GHG emissions toward a long-term and sustainable battery recycling strategy.

### 5.3 Conclusion

In this study, a sustainable next-generation all solid-state battery design and recycling strategy is introduced. This approach demonstrates the recovery and regeneration of solid-state electrolytes and cathodes from spent batteries without using toxic chemicals or energy-intensive processes. Considerations for anodes are also discussed. The EverBatt model was employed to evaluate the energy consumption and environmental impact of the recycling strategy and compare it with traditional pyrometallurgical and hydrometallurgical methods. It was found that direct recycling methods significantly reduce both energy consumption and greenhouse gas emissions as a result of reduced material requirements from upstream processing as well as eliminating the need for smelting. Moreover, techniques to recover the electrolyte in spent all solid-state batteries were shown to only slightly increase the energy consumption and emissions. To validate the model, pristine Li | Li<sub>6</sub>PS<sub>5</sub>Cl | LiCoO<sub>2</sub> full cells were experimentally fabricated and regenerated. Regenerated Li<sub>6</sub>PS<sub>5</sub>Cl was found to have similar structural properties and ionic conductivity compared to pristine Li<sub>6</sub>PS<sub>5</sub>Cl and LiCoO<sub>2</sub> was able to regain the lithium content lost during cell cycling. The fully-recycled solid electrolyte and cathode materials were reassembled into a full cell and demonstrated similar electrochemical properties and capacity retention compared to the pristine cell. The results shown here demonstrate the feasibility of direct recovery and regeneration of SSEs and cathodes in next-generation ASSBs of various chemistries, offering a scalable, low cost, and sustainable pathway for handling spent batteries at their end-of-life.

Chapter 5, in full, is a reprint of the material “Sustainable design of fully recyclable all solid-state batteries” as it appears in MRS Energy & Sustainability. Tan, D. H. S.; Xu, P.; Yang, H.; Kim, M.-c.; Nguyen, H.; Wu, E. A.; Doux, J.-M.; Banerjee, A.; Meng, Y. S.; Chen, Z. The dissertation author was the first author in both papers, all authors contributed to this work.

## Chapter 6. Perspectives & Summary

Over the past century, mankind saw immense improvements in food and water sustainability. In the 21<sup>st</sup> century, we would undoubtedly see an equal if not more prevalent progress in energy sustainability, with energy storage becoming a core driver of the global economy. This is propelled by extensive advancements in new battery technologies such as ASSBs. By offering higher energy densities, improved safety factors, and environmentally friendly designs, they will play an increasing role in our lives. While batteries today power EVs and other portable devices, they may soon also be commonplace in our homes and urban communities. However, development of new battery technologies has often been criticized for being more hype than reality, with various private and public stakeholders frustrated at its relatively slow pace of commercialization. Moreover, the general public along with technology investors have become accustomed to the exponential increase in computer processing power, famously characterized by Moore's law.<sup>249</sup> On the other hand, we must also give credence to the fact that unlike consumer commodities or advancements in digital software technology, the relatively sophisticated hardware and intensive capital tooling involved in battery development would ultimately result in slower paced product development. Fundamentally, it boils down to the fact that batteries are complex systems made of numerous interdependent materials and interfaces (electrodes, electrolytes and supporting architectures) that will all affect its electrochemical performance. Improvements in this regard can only be achieved with new chemistries and careful engineering of each component of the system. As a result, exciting developments in the literature can gain notoriety from their scientific breakthroughs but still take years before being applied to commercialized products. That being said, there are still significant steps that the battery research community can take to further accelerate commercialization of new discoveries made in the laboratory. While



these may not follow the rates dictated by Moore's law, they can allow quicker turnover and more efficient allocation of resources both in academia and the industry.

### **6.1 Bringing Discoveries into the Market**

Compared to the vast number of scientific discoveries reported in the literature, there has been relatively few breakthroughs that translate into commercialized products. Without understating the monumental importance of fundamental research at the laboratory scale, the challenges in transferring know-how to industrially relevant scales, in order to suit various product configurations and target applications must also be considered. Laboratory scale research, typically lead by academic scientists, focuses on material level selection, testing, and development. These use small scale coin-type cells, or at occasion single-layer designs which may not provide sufficient data or practical validation required for industrial evaluation where throughput and defect elimination are concerned (Figure 6.1a). Industry relevant cells are typically high capacities, with multilayer configurations fabricated using automated continuous processes (Figure 6.1c). As such, universities or national laboratories often lack the material resources to utilize mass-production processes, or to extrapolate the electrochemical and physicochemical properties of market products relevant for the industry. Additionally, today's academic evaluation system provides little incentive for scientists to bridge this gap, forming a bottleneck between lab and market that is somewhat filled haphazardly by start-up companies. These companies sit in the middle of laboratory discoveries, often made by their founders, and large corporations that adopt a "wait and see" approach. Although successful discoveries in the laboratory are widely publicized in academic journals, successful start-up companies or large corporations instead tend to protect successful practices, making information availability of pilot-scale cells extremely limited. This behavior is characterized by the "free-rider" problem, where despite widespread benefits to the entire community if such crucial information is shared, the start-ups who invested heavily in its development would in fact lose out to the competition if their practices and data collected are

widely shared. Conversely, academic scientists never shy away from an opportunity to publish or publicly discuss their findings, due to inherent non-financial benefits as part of the academic evaluation system. As such, this inefficiency gap can instead be bridged at least in part, by public institutions that have non-economic or other national interests in the technology's success. This can be done by investing in mid-level pilot scale testing laboratories within universities or accessible national laboratories (Figure 6.1b), with the sole purpose of testing and evaluating promising discoveries from laboratory scale research in scales more relevant to industry but yet of scientific interest to academic researchers.

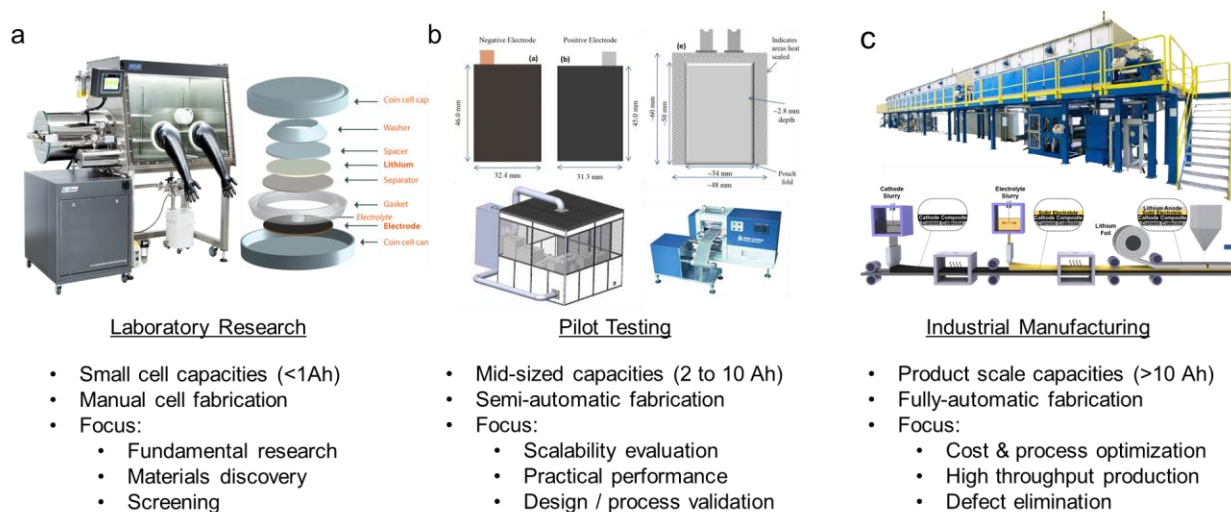


**Figure 6.1.** Illustration and descriptions of cell and manufacturing protocols used in (a) laboratory scale research typically done using gloveboxes and coin cells, (b) pilot scale testing typically done with multi-layer pouch type cells in dry rooms and (c) industrial scale manufacturing during continuous high throughput roll to roll processes.

As it is fundamentally important for knowledge and information gained in these pilot-scale research to be made public, similar to how publicly funded research is published, such pilot scale testing should thus be led and operated by the very public institutions they reside in. While similar investments have been made in existing universities and national laboratories within the United States in the past, access to them are often restricted and limited to privately paying partners or collaborators within closed-door academic communities. Unlike competitive proposal driven user-facilities, such as synchrotron beamlines openly accessible by academic researchers, access to

such pilot-scale fabrication and testing facilities tend to be highly restricted. Compared to traditional national laboratories which operate synchrotrons that cost tax-payers billions to construct and more to operate, establishing of pilot-scale testing facilities would be comparatively cost-effective and less sophisticated to operate. Additionally, this would result in job-creation for highly desired skillsets currently monopolized by the industry, diversifying potential career pathways for researchers with mixed technical backgrounds. Scientific publications that include performance and manufacturing demonstration on such scales would also raise the academic credibility of scientists who conduct the research. As an example, this was demonstrated when Samsung released a complete dataset of their pilot-scale anode-free ASSB manufactured entirely in a dry room<sup>231</sup>, which made a large enough impact on the energy storage community to quell many misconceptions about ASSBs. Such capabilities, if available and accessible, would also instill confidence within public funding agencies in evaluation of proposed concepts and ideas, raising the overall success rates of projects funded. While the discussions made in this section are described in the context of battery technology development in general, such facilities are also cross applicable and can be expanded to suit other important research topics such as solar or fuel cell development as well.

Speaking as a graduating researcher aspiring to bridge the gap between discoveries made in our laboratory to the market through a startup, availability of such discussed resources can potentially shave years off our product development efforts and bolster our ability to raise capital. It is my personal belief and hope that governmental and funding agencies recognize this bottleneck in research and development within the United States and around the world, and recognize the potential long term value in diverting or investing new resources into such infrastructure, be it for universities or national laboratories, accessible by all researchers. Like many other promising technologies, development of ASSBs is on the cusp of widespread market penetration. The past two decades have propelled major breakthroughs in fundamental

understanding, interfacial stabilization, electrode to cell level design, as well as pathways to achieve battery sustainability. Beyond this phase, focus now needs to be concentrated on scalable engineering and pilot-scale prototyping, for scalability itself a vital form of innovation. Commercialization of ASSBs is no longer a question of if, but of when, with encouraging trends for applications in new markets such as safe and long lasting grid-energy storage, potentially addressing the bottleneck in renewable energy adoption.

This dissertation attempts to cover a broad range of timely and relevant scientific breakthroughs in ASSBs, discussing fundamental studies on SSE chemical and electrochemical properties, its scalability along with cell level integration through the use of solution processing strategies, performance enhancements such as use of lithium-silicon alloys to increase critical current densities as well as establishment of a full recyclable ASSB model using sustainable processes that decrease energy costs and GHG emissions. Finally, we discussed the necessary steps to bridge such laboratory scale developments toward industrially relevant products, with discussion centered around the need for investments into pilot-scale fabrication and testing facilities. Through fundamental understanding of interfacial phenomena and materials compatibility, the work discussed in this dissertation may serve as a basis toward improved cell design and manufacturing scalability of next generation ASSBs; serving future energy devices to simultaneously improve our quality of life and enable a more sustainable future.

## References

1. Marbella, L. E.; Zekoll, S.; Kasemchainan, J.; Emge, S. P.; Bruce, P. G.; Grey, C. P., <sup>7</sup>Li NMR Chemical Shift Imaging To Detect Microstructural Growth of Lithium in All-Solid-State Batteries. *Chem. Mater.* **2019**, *31* (8), 2762-2769.
2. Henze, V. Electric Vehicle Sales to Fall 18% in 2020 but Long-term Prospects Remain Undimmed. <https://about.bnef.com/blog/electric-vehicle-sales-to-fall-18-in-2020-but-long-term-prospects-remain-undimmed/> (accessed Feb).
3. Bowman, M. EIA projects that renewables will provide nearly half of world electricity by 2050. <https://www.eia.gov/todayinenergy/detail.php?id=41533> (accessed Feb).
4. Dunn, B.; Kamath, H.; Tarascon, J.-M., Electrical Energy Storage for the Grid: A Battery of Choices. *Science* **2011**, *334*.
5. Xu, p.; Tan, D. H. S.; Chen, Z., Emerging Trends in Sustainable Battery Chemistries. *Submitted - In review* **2021**.
6. Kong, L.; Li, C.; Jiang, J.; Pecht, M., Li-Ion Battery Fire Hazards and Safety Strategies. *Energies* **2018**, *11* (9), 2191.
7. Tan, D. H. S.; Xu, P.; Chen, Z., Enabling sustainable critical materials for battery storage through efficient recycling and improved design: A perspective. *MRS Energy & Sustainability* **2020**, *7*.
8. Gil-Alana, L. A.; Monge, M., Lithium: Production and estimated consumption. Evidence of persistence. *Resour. Policy* **2019**, *60*, 198-202.
9. Chen, M.; Ma, X.; Chen, B.; Arsenault, R.; Karlson, P.; Simon, N.; Wang, Y., Recycling End-of-Life Electric Vehicle Lithium-Ion Batteries. *Joule* **2019**, *3* (11), 2622-2646.
10. Shengo, M. L.; Kime, M. B.; Mambwe, M. P.; Nyembo, T. K., A review of the beneficiation of copper-cobalt-bearing minerals in the Democratic Republic of Congo. *Journal of Sustainable Mining* **2019**, *18* (4), 226-246.
11. Campbell, G. A., The cobalt market revisited. *Mineral Economics* **2019**, *33*, 21–28
12. Tan, D. H. S.; Xu, P.; Yang, H.; Kim, M.-c.; Nguyen, H.; Wu, E. A.; Doux, J.-M.; Banerjee, A.; Meng, Y. S.; Chen, Z., Sustainable design of fully recyclable all solid-state batteries. *MRS Energy & Sustainability* **2020**, *7*.
13. Tan, D. H. S.; Banerjee, A.; Chen, Z.; Meng, Y. S., From nanoscale interface characterization to sustainable energy storage using all-solid-state batteries. *Nat Nanotechnol* **2020**, *15* (3), 170-180.
14. Yu, C.; Ganapathy, S.; Hageman, J.; van Eijck, L.; van Eck, E. R. H.; Zhang, L.; Schwietert, T.; Basak, S.; Kelder, E. M.; Wagemaker, M., Facile Synthesis toward the Optimal Structure-Conductivity Characteristics of the Argyrodite Li<sub>6</sub>PS<sub>5</sub>Cl Solid-State Electrolyte. *ACS Appl. Mater. Interfaces* **2018**, *10* (39), 33296-33306.

15. Nguyen, H.; Banerjee, A.; Wang, X.; Tan, D.; Wu, E. A.; Doux, J.-M.; Stephens, R.; Verbist, G.; Meng, Y. S., Single-step synthesis of highly conductive Na<sub>3</sub>PS<sub>4</sub> solid electrolyte for sodium all solid-state batteries. *J. Power Sources* **2019**, *435*, 126623.
16. Kato, Y.; Hori, S.; Saito, T.; Suzuki, K.; Hirayama, M.; Mitsui, A.; Yonemura, M.; Iba, H.; Kanno, R., High-power all-solid-state batteries using sulfide superionic conductors. *Nat. Energy* **2016**, *1* (4).
17. Zhu, Y.; He, X.; Mo, Y., Origin of Outstanding Stability in the Lithium Solid Electrolyte Materials: Insights from Thermodynamic Analyses Based on First-Principles Calculations. *ACS Appl. Mater. Interfaces* **2015**, *7* (42), 23685-93.
18. Zhang, H.; Li, C.; Piszcz, M.; Coya, E.; Rojo, T.; Rodriguez-Martinez, L. M.; Armand, M.; Zhou, Z., Single lithium-ion conducting solid polymer electrolytes: advances and perspectives. *Chem Soc Rev* **2017**, *46* (3), 797-815.
19. Mindemark, J.; Lacey, M. J.; Bowden, T.; Brandell, D., Beyond PEO—Alternative host materials for Li<sup>+</sup> conducting solid polymer electrolytes. *Prog. Polym. Sci.* **2018**, *81*, 114-143.
20. Yao, P.; Yu, H.; Ding, Z.; Liu, Y.; Lu, J.; Lavorgna, M.; Wu, J.; Liu, X., Review on Polymer-Based Composite Electrolytes for Lithium Batteries. *Front Chem* **2019**, *7*, 522.
21. Wang, S.; Bai, Q.; Nolan, A. M.; Liu, Y.; Gong, S.; Sun, Q.; Mo, Y., Lithium Chlorides and Bromides as Promising Solid-State Chemistries for Fast Ion Conductors with Good Electrochemical Stability. *Angew. Chem., Int. Ed. Engl.* **2019**, *58* (24), 8039-8043.
22. Asano, T.; Sakai, A.; Ouchi, S.; Sakaida, M.; Miyazaki, A.; Hasegawa, S., Solid Halide Electrolytes with High Lithium-Ion Conductivity for Application in 4 V Class Bulk-Type All-Solid-State Batteries. *Adv. Mater.* **2018**, *30* (44), e1803075.
23. Zhang, W.; Leichtweiss, T.; Culver, S. P.; Koerver, R.; Das, D.; Weber, D. A.; Zeier, W. G.; Janek, J., The Detrimental Effects of Carbon Additives in Li<sub>10</sub>GeP<sub>2</sub>S<sub>12</sub> Based Solid-State Batteries. *ACS Appl. Mater. Interfaces* **2017**, *9* (41), 35888-35896.
24. Auvergniot, J.; Cassel, A.; Ledeuil, J.-B.; Viallet, V.; Seznec, V.; Dedryvère, R., Interface Stability of Argyrodite Li<sub>6</sub>PS<sub>5</sub>Cl toward LiCoO<sub>2</sub>, LiNi<sub>1/3</sub>Co<sub>1/3</sub>Mn<sub>1/3</sub>O<sub>2</sub>, and LiMn<sub>2</sub>O<sub>4</sub> in Bulk All-Solid-State Batteries. *Chem. Mater.* **2017**, *29* (9), 3883-3890.
25. Auvergniot, J.; Cassel, A.; Foix, D.; Viallet, V.; Seznec, V.; Dedryvère, R., Redox activity of argyrodite Li<sub>6</sub>PS<sub>5</sub>Cl electrolyte in all-solid-state Li-ion battery: An XPS study. *Solid State Ionics* **2017**, *300*, 78-85.
26. Haruyama, J.; Sodeyama, K.; Han, L.; Takada, K.; Tateyama, Y., Space-Charge Layer Effect at Interface between Oxide Cathode and Sulfide Electrolyte in All-Solid-State Lithium-Ion Battery. *Chem. Mater.* **2014**, *26* (14), 4248-4255.
27. Ohta, N.; Takada, K.; Zhang, L.; Ma, R.; Osada, M.; Sasaki, T., Enhancement of the High-Rate Capability of Solid-State Lithium Batteries by Nanoscale Interfacial Modification. *Adv. Mater.* **2006**, *18* (17), 2226-2229.

28. Li, X.; Jin, L.; Song, D.; Zhang, H.; Shi, X.; Wang, Z.; Zhang, L.; Zhu, L., LiNbO<sub>3</sub>-coated LiNi<sub>0.8</sub>Co<sub>0.1</sub>Mn<sub>0.1</sub>O<sub>2</sub> cathode with high discharge capacity and rate performance for all-solid-state lithium battery. *J. Energy Chem.* **2019**, *40*, 39-45.
29. Haruyama, J.; Sodeyama, K.; Tateyama, Y., Cation Mixing Properties toward Co Diffusion at the LiCoO<sub>2</sub> Cathode/Sulfide Electrolyte Interface in a Solid-State Battery. *ACS Appl. Mater. Interfaces* **2017**, *9* (1), 286-292.
30. Sakuda, A.; Hayashi, A.; Tatsumisago, M., Interfacial Observation between LiCoO<sub>2</sub> Electrode and Li<sub>2</sub>S–P<sub>2</sub>S<sub>5</sub> Solid Electrolytes of All-Solid-State Lithium Secondary Batteries Using Transmission Electron Microscopy. *Chem. Mater.* **2010**, *22* (3), 949-956.
31. Woo, J. H.; Trevey, J. E.; Cavanagh, A. S.; Choi, Y. S.; Kim, S. C.; George, S. M.; Oh, K. H.; Lee, S.-H., Nanoscale Interface Modification of LiCoO<sub>2</sub> by Al<sub>2</sub>O<sub>3</sub> Atomic Layer Deposition for Solid-State Li Batteries. *J. Electrochem. Soc.* **2012**, *159* (7), A1120-A1124.
32. Okada, K.; Machida, N.; Naito, M.; Shigematsu, T.; Ito, S.; Fujiki, S.; Nakano, M.; Aihara, Y., Preparation and electrochemical properties of LiAlO<sub>2</sub> coated Li(Ni<sub>1/3</sub>Mn<sub>1/3</sub>Co<sub>1/3</sub>)O<sub>2</sub> for all-solid-state batteries. *Solid State Ionics* **2014**, *255*, 120-127.
33. Xiao, Y.; Miara, L. J.; Wang, Y.; Ceder, G., Computational Screening of Cathode Coatings for Solid-State Batteries. *Joule* **2019**, *3* (5), 1252-1275.
34. Koerver, R.; Aygün, I.; Leichtweiß, T.; Dietrich, C.; Zhang, W.; Binder, J. O.; Hartmann, P.; Zeier, W. G.; Janek, J., Capacity Fade in Solid-State Batteries: Interphase Formation and Chemomechanical Processes in Nickel-Rich Layered Oxide Cathodes and Lithium Thiophosphate Solid Electrolytes. *Chem. Mater.* **2017**, *29* (13), 5574-5582.
35. Wenzel, S.; Randau, S.; Leichtweiß, T.; Weber, D. A.; Sann, J.; Zeier, W. G.; Janek, J., Direct Observation of the Interfacial Instability of the Fast Ionic Conductor Li<sub>10</sub>GeP<sub>2</sub>S<sub>12</sub> at the Lithium Metal Anode. *Chem. Mater.* **2016**, *28* (7), 2400-2407.
36. Banerjee, A.; Wang, X.; Fang, C.; Wu, E. A.; Meng, Y. S., Interfaces and Interphases in All-Solid-State Batteries with Inorganic Solid Electrolytes. *Chem Rev* **2020**.
37. Han, X.; Gong, Y.; Fu, K. K.; He, X.; Hitz, G. T.; Dai, J.; Pearse, A.; Liu, B.; Wang, H.; Rubloff, G.; Mo, Y.; Thangadurai, V.; Wachsman, E. D.; Hu, L., Negating interfacial impedance in garnet-based solid-state Li metal batteries. *Nat. Mater.* **2017**, *16* (5), 572-579.
38. Yersak, T.; Salvador, J. R.; Schmidt, R. D.; Cai, M., Hot Pressed, Fiber-Reinforced (Li<sub>2</sub>S)<sub>70</sub>(P<sub>2</sub>S<sub>5</sub>)<sub>30</sub> Solid-State Electrolyte Separators for Li Metal Batteries. *ACS Appl. Energy Mater.* **2019**, *2*, 3523–3531.
39. Kim, S. H.; Kim, K.; Choi, H.; Im, D.; Heo, S.; Choi, H. S., In situ observation of lithium metal plating in a sulfur-based solid electrolyte for all-solid-state batteries. *J. Mater. Chem. A* **2019**, *7*, 13650–13657.
40. Tao, X.; Liu, Y.; Liu, W.; Zhou, G.; Zhao, J.; Lin, D.; Zu, C.; Sheng, O.; Zhang, W.; Lee, H. W.; Cui, Y., Solid-State Lithium-Sulfur Batteries Operated at 37 degrees C with Composites of Nanostructured Li<sub>7</sub>La<sub>3</sub>Zr<sub>2</sub>O<sub>12</sub>/Carbon Foam and Polymer. *Nano Lett.* **2017**, *17* (5), 2967-2972.

41. Ates, T.; Keller, M.; Kulisch, J.; Adermann, T.; Passerini, S., Development of an all-solid-state lithium battery by slurry-coating procedures using a sulfidic electrolyte. *Energy Storage Materials* **2019**, *17*, 204-210.
42. Han, F.; Yue, J.; Zhu, X.; Wang, C., Suppressing Li Dendrite Formation in  $\text{Li}_2\text{S-P}_2\text{S}_5$  Solid Electrolyte by Lil Incorporation. *Adv. Energy Mater.* **2018**, *8* (18), 1703644.
43. Li, Y.; Zhou, W.; Chen, X.; Lu, X.; Cui, Z.; Xin, S.; Xue, L.; Jia, Q.; Goodenough, J. B., Mastering the interface for advanced all-solid-state lithium rechargeable batteries. *Proc. Natl. Acad. Sci. U. S. A.* **2016**, *113* (47), 13313-13317.
44. Kerman, K.; Luntz, A.; Viswanathan, V.; Chiang, Y.-M.; Chen, Z., Review—Practical Challenges Hindering the Development of SolidState Li Ion Batteries. *J. Electrochem. Soc.* **2017**, *164* (7), A1731-A1744.
45. Aguesse, F.; Manalastas, W.; Buannic, L.; Lopez Del Amo, J. M.; Singh, G.; Llodes, A.; Kilner, J., Investigating the Dendritic Growth during Full Cell Cycling of Garnet Electrolyte in Direct Contact with Li Metal. *ACS Appl. Mater. Interfaces* **2017**, *9* (4), 3808-3816.
46. Swamy, T.; Park, R.; Sheldon, B. W.; Rettenwander, D. P., Lukas; Berendts, S.; Uecker, R.; Carter, C.; Chiang, Y.-M., Lithium Metal Penetration Induced by Electrodeposition through Solid Electrolytes: Example in Single-Crystal  $\text{Li}_6\text{La}_3\text{ZrTaO}_{12}$  Garnet. *J. Electrochem. Soc.* **2018**, *165* (16), A3648-A3655.
47. Neudecker, B. J.; Dudney, N. J.; Bates, J. B., "Lithium-Free" Thin-Film Battery with In Situ Plated Li Anode. *J. Electrochem. Soc.* **2000**, *147* (2), 517-523.
48. Li, J.; Ma, C.; Chi, M.; Liang, C.; Dudney, N. J., Solid Electrolyte: the Key for High-Voltage Lithium Batteries. *Adv. Energy Mater.* **2015**, *5* (4), 1401408.
49. Fang, C.; Li, J.; Zhang, M.; Zhang, Y.; Yang, F.; Lee, J. Z.; Lee, M. H.; Alvarado, J.; Schroeder, M. A.; Yang, Y.; Lu, B.; Williams, N.; Ceja, M.; Yang, L.; Cai, M.; Gu, J.; Xu, K.; Wang, X.; Meng, Y. S., Quantifying inactive lithium in lithium metal batteries. *Nature* **2019**, *572* (7770), 511-515.
50. Sharafi, A.; Kazyak, E.; Davis, A. L.; Yu, S.; Thompson, T.; Siegel, D. J.; Dasgupta, N. P.; Sakamoto, J., Surface Chemistry Mechanism of Ultra-Low Interfacial Resistance in the Solid-State Electrolyte  $\text{Li}_7\text{La}_3\text{Zr}_2\text{O}_{12}$ . *Chem. Mater.* **2017**, *29* (18), 7961-7968.
51. Tao, Y.; Chen, S.; Liu, D.; Peng, G.; Yao, X.; Xu, X., Lithium Superionic Conducting Oxysulfide Solid Electrolyte with Excellent Stability against Lithium Metal for All-Solid-State Cells. *J. Electrochem. Soc.* **2016**, *163* (2), A96-A101.
52. Sun, Y.; Suzuki, K.; Hara, K.; Hori, S.; Yano, T.-a.; Hara, M.; Hirayama, M.; Kanno, R., Oxygen substitution effects in  $\text{Li}_{10}\text{GeP}_2\text{S}_{12}$  solid electrolyte. *J. Power Sources* **2016**, *324*, 798-803.
53. Kamaya, N.; Homma, K.; Yamakawa, Y.; Hirayama, M.; Kanno, R.; Yonemura, M.; Kamiyama, T.; Kato, Y.; Hama, S.; Kawamoto, K.; Mitsui, A., A lithium superionic conductor. *Nat. Mater.* **2011**, *10* (9), 682-6.



54. Han, F.; Zhu, Y.; He, X.; Mo, Y.; Wang, C., Electrochemical Stability of  $\text{Li}_{10}\text{GeP}_2\text{S}_{12}$  and  $\text{Li}_7\text{La}_3\text{Zr}_2\text{O}_{12}$  Solid Electrolytes. *Adv. Energy Mater.* **2016**, 6 (8), 1501590.
55. Han, F.; Gao, T.; Zhu, Y.; Gaskell, K. J.; Wang, C., A Battery Made from a Single Material. *Adv. Mater.* **2015**, 27 (23), 3473-83.
56. Yan, X.; Li, Z.; Wen, Z.; Han, W.,  $\text{Li}/\text{Li}_7\text{La}_3\text{Zr}_2\text{O}_{12}/\text{LiFePO}_4$  All-Solid-State Battery with Ultrathin Nanoscale Solid Electrolyte. *J. Phys. Chem. C* **2017**, 121 (3), 1431-1435.
57. Shi, X.; Ma, N.; Wu, Y.; Lu, Y.; Xiao, Q.; Li, Z.; Lei, G., Fabrication and electrochemical properties of LATP/PVDF composite electrolytes for rechargeable lithium-ion battery. *Solid State Ionics* **2018**, 325, 112-119.
58. Xu, L.; Tang, S.; Cheng, Y.; Wang, K.; Liang, J.; Liu, C.; Cao, Y.-C.; Wei, F.; Mai, L., Interfaces in Solid-State Lithium Batteries. *Joule* **2018**, 2 (10), 1991-2015.
59. Lewis, J. A.; Tippens, J.; Cortes, F. J. Q.; McDowell, M. T., Chemo-Mechanical Challenges in Solid-State Batteries. *Trends in Chemistry* **2019**.
60. Manthiram, A.; Yu, X.; Wang, S., Lithium battery chemistries enabled by solid-state electrolytes. *Nat. Rev. Mater.* **2017**, 2 (4).
61. Choi, S.; Jeon, M.; Ahn, J.; Jung, W. D.; Choi, S. M.; Kim, J. S.; Lim, J.; Jang, Y. J.; Jung, H. G.; Lee, J. H.; Sang, B. I.; Kim, H., Quantitative Analysis of Microstructures and Reaction Interfaces on Composite Cathodes in All-Solid-State Batteries Using a Three-Dimensional Reconstruction Technique. *ACS Appl. Mater. Interfaces* **2018**, 10 (28), 23740-23747.
62. Wang, Z.; Santhanagopalan, D.; Zhang, W.; Wang, F.; Xin, H. L.; He, K.; Li, J.; Dudney, N.; Meng, Y. S., In Situ STEM-EELS Observation of Nanoscale Interfacial Phenomena in All-Solid-State Batteries. *Nano Lett.* **2016**, 16 (6), 3760-7.
63. Sang, L.; Haasch, R. T.; Gewirth, A. A.; Nuzzo, R. G., Evolution at the Solid Electrolyte/Gold Electrode Interface during Lithium Deposition and Stripping. *Chem. Mater.* **2017**, 29 (7), 3029-3037.
64. Ren, Y.; Shen, Y.; Lin, Y.; Nan, C.-W., Direct observation of lithium dendrites inside garnet-type lithium-ion solid electrolyte. *Electrochem. Commun.* **2015**, 57, 27-30.
65. Seitzman, N.; Guthrey, H.; Sulas, D. B.; Platt, H. A. S.; Al-Jassim, M.; Pylypenko, S., Toward All-Solid-State Lithium Batteries: Three-Dimensional Visualization of Lithium Migration in  $\beta\text{-Li}_3\text{PS}_4$  Ceramic Electrolyte. *J. Electrochem. Soc.* **2018**, 165 (16), A3732-A3737.
66. Li, T.; Kang, H.; Zhou, X.; Lim, C.; Yan, B.; De Andrade, V.; De Carlo, F.; Zhu, L., Three-Dimensional Reconstruction and Analysis of All-Solid Li-Ion Battery Electrode Using Synchrotron Transmission X-ray Microscopy Tomography. *ACS Appl. Mater. Interfaces* **2018**, 10 (20), 16927-16931.
67. Chen-Wiegart, Y.-c. K.; Liu, Z.; Faber, K. T.; Barnett, S. A.; Wang, J., 3D analysis of a  $\text{LiCoO}_2\text{-Li}(\text{Ni}_{1/3}\text{Mn}_{1/3}\text{Co}_{1/3})\text{O}_2$  Li-ion battery positive electrode using x-ray nano-tomography. *Electrochem. Commun.* **2013**, 28, 127-130.

68. Wang, C.; Gong, Y.; Dai, J.; Zhang, L.; Xie, H.; Pastel, G.; Liu, B.; Wachsman, E.; Wang, H.; Hu, L., In Situ Neutron Depth Profiling of Lithium Metal-Garnet Interfaces for Solid State Batteries. *J. Am. Chem. Soc.* **2017**, *139* (40), 14257-14264.
69. Lee, J. Z.; Wynn, T. A.; Schroeder, M. A.; Alvarado, J.; Wang, X.; Xu, K.; Meng, Y. S., Cryogenic Focused Ion Beam Characterization of Lithium Metal Anodes. *ACS Energy Lett.* **2019**, *4* (2), 489-493.
70. Santhanagopalan, D.; Qian, D.; McGilvray, T.; Wang, Z.; Wang, F.; Camino, F.; Graetz, J.; Dudney, N.; Meng, Y. S., Interface Limited Lithium Transport in Solid-State Batteries. *J Phys Chem Lett* **2014**, *5* (2), 298-303.
71. Hakari, T.; Deguchi, M.; Mitsuhara, K.; Ohta, T.; Saito, K.; Orikasa, Y.; Uchimoto, Y.; Kowada, Y.; Hayashi, A.; Tatsumisago, M., Structural and Electronic-State Changes of a Sulfide Solid Electrolyte during the Li Deinsertion–Insertion Processes. *Chem. Mater.* **2017**, *29* (11), 4768-4774.
72. Schnell, J.; Günther, T.; Knoche, T.; Vieider, C.; Köhler, L.; Just, A.; Keller, M.; Passerini, S.; Reinhart, G., All-solid-state lithium-ion and lithium metal batteries – paving the way to large-scale production. *J. Power Sources* **2018**, *382*, 160-175.
73. Zhang, X.; Liu, T.; Zhang, S.; Huang, X.; Xu, B.; Lin, Y.; Xu, B.; Li, L.; Nan, C. W.; Shen, Y., Synergistic Coupling between  $\text{Li}_{6.75}\text{La}_3\text{Zr}_{1.75}\text{Ta}_{0.25}\text{O}_{12}$  and Poly(vinylidene fluoride) Induces High Ionic Conductivity, Mechanical Strength, and Thermal Stability of Solid Composite Electrolytes. *J. Am. Chem. Soc.* **2017**, *139* (39), 13779-13785.
74. Yun-Chae Jung, a.-M. L., bJeong-Hee Choi, bSeung Soon Jang, cand Dong-Won Kim, All Solid-State Lithium Batteries Assembled with Hybrid Solid Electrolytes. *J. Electrochem. Soc.* **2015**, *162* (4), A704-A710.
75. Nam, Y. J.; Oh, D. Y.; Jung, S. H.; Jung, Y. S., Toward practical all-solid-state lithium-ion batteries with high energy density and safety: Comparative study for electrodes fabricated by dry- and slurry-mixing processes. *J. Power Sources* **2018**, *375*, 93-101.
76. Tan, D. H. S.; Banerjee, A.; Deng, Z.; Wu, E. A.; Nguyen, H.; Doux, J.-M.; Wang, X.; Cheng, J.-h.; Ong, S. P.; Meng, Y. S.; Chen, Z., Enabling Thin and Flexible Solid-State Composite Electrolytes by the Scalable Solution Process. *ACS Appl. Energy Mater.* **2019**, *2*, 6542–6550.
77. Sakuda, A.; Kuratani, K.; Yamamoto, M.; Takahashi, M.; Takeuchi, T.; Kobayashia, H., All-Solid-State Battery Electrode Sheets Prepared by a Slurry Coating Process. *J. Electrochem. Soc.* **2017**, *164* (12), A2474-A2478.
78. Hippauf, F.; Schumm, B.; Doerfler, S.; Althues, H.; Fujiki, S.; Shiratsushi, T.; Tsujimura, T.; Aihara, Y.; Kaskel, S., Overcoming binder limitations of sheet-type solid-state cathodes using a solvent-free dry-film approach. *Energy Storage Materials* **2019**, *21*, 390-398.
79. Lee, K.; Kim, S.; Park, J.; Park, S. H.; Coskun, A.; Jung, D. S.; Cho, W.; Choi, J. W., Selection of Binder and Solvent for Solution-Processed All-Solid-State Battery. *J. Electrochem. Soc.* **2017**, *164* (9), A2075-A2081.

80. Lee, K.; Lee, J.; Choi, S.; Char, K.; Choi, J. W., Thiol–Ene Click Reaction for Fine Polarity Tuning of Polymeric Binders in Solution-Processed All-Solid-State Batteries. *ACS Energy Lett.* **2018**, *4* (1), 94-101.
81. Hayashi, A.; Muramatsu, H.; Ohtomo, T.; Hama, S.; Tatsumisago, M., Improvement of chemical stability of  $\text{Li}_3\text{PS}_4$  glass electrolytes by adding  $\text{MxO}_y$  (M = Fe, Zn, and Bi) nanoparticles. *J. Mater. Chem. A* **2013**, *1* (21), 6320.
82. Oh, D. Y.; Nam, Y. J.; Park, K. H.; Jung, S. H.; Kim, K. T.; Ha, A. R.; Jung, Y. S., Slurry-Fabricable  $\text{Li}^+$  Conductive Polymeric Binders for Practical All-Solid-State Lithium-Ion Batteries Enabled by Solvate Ionic Liquids. *Adv. Energy Mater.* **2019**, *9* (16), 1802927.
83. Yamamoto, M.; Terauchi, Y.; Sakuda, A.; Takahashi, M., Binder-free sheet-type all-solid-state batteries with enhanced rate capabilities and high energy densities. *Sci Rep* **2018**, *8* (1), 1212.
84. Liang, X.; Han, D.; Wang, Y.; Lan, L.; Mao, J., Preparation and performance study of a PVDF–LATP ceramic composite polymer electrolyte membrane for solid-state batteries. *RSC Adv.* **2018**, *8* (71), 40498-40504.
85. Oh, D. Y.; Nam, Y. J.; Park, K. H.; Jung, S. H.; Cho, S.-J.; Kim, Y. K.; Lee, Y.-G.; Lee, S.-Y.; Jung, Y. S., Excellent Compatibility of Solvate Ionic Liquids with Sulfide Solid Electrolytes: Toward Favorable Ionic Contacts in Bulk-Type All-Solid-State Lithium-Ion Batteries. *Adv. Energy Mater.* **2015**, *5* (22), 1500865.
86. Zeng, X.; Li, J.; Ren, Y., Prediction of Various Discarded Lithium Batteries in China. *IEEE International Symposium on Sustainable Systems and Technology (ISSST)* **2012**.
87. Xu, J.; Thomas, H. R.; Francis, R. W.; Lum, K. R.; Wang, J.; Liang, B., A review of processes and technologies for the recycling of lithium-ion secondary batteries. *J. Power Sources* **2008**, *177* (2), 512-527.
88. Kunz, T., DOE launches its first lithium-ion battery recycling R&D center: ReCell. Argonne National Laboratory, 2019.
89. May, G. J.; Davidson, A.; Monahov, B., Lead batteries for utility energy storage: A review. *Journal of Energy Storage* **2018**, *15*, 145-157.
90. Zhang, X.; Li, L.; Fan, E.; Xue, Q.; Bian, Y.; Wu, F.; Chen, R., Toward sustainable and systematic recycling of spent rechargeable batteries. *Chem. Soc. Rev.* **2018**, *47* (19), 7239-7302.
91. Li, L.; Zhang, X.; Li, M.; Chen, R.; Wu, F.; Amine, K.; Lu, J., The Recycling of Spent Lithium-Ion Batteries: a Review of Current Processes and Technologies. *Electrochem. Energy Rev.* **2018**, *1* (4), 461-482.
92. Liu, T.; Zhang, Y.; Chen, C.; Lin, Z.; Zhang, S.; Lu, J., Sustainability-inspired cell design for a fully recyclable sodium ion battery. *Nat. Commun.* **2019**, *10* (1), 1965.

93. Zheng, X.; Zhu, Z.; Lin, X.; Zhang, Y.; He, Y.; Cao, H.; Sun, Z., A Mini-Review on Metal Recycling from Spent Lithium Ion Batteries. *Engineering* **2018**, *4* (3), 361-370.
94. Nowak, S.; Winter, M., The Role of Sub- and Supercritical CO<sub>2</sub> as "Processing Solvent" for the Recycling and Sample Preparation of Lithium Ion Battery Electrolytes. *Molecules* **2017**, *22* (3).
95. Miura, A.; Rosero-Navarro, N. C.; Sakuda, A.; Tadanaga, K.; Phuc, N. H. H.; Matsuda, A.; Machida, N.; Hayashi, A.; Tatsumisago, M., Liquid-phase syntheses of sulfide electrolytes for all-solid-state lithium battery. *Nat. Rev. Chem.* **2019**, *3* (3), 189-198.
96. Wang, Y.; Lu, D.; Bowden, M.; El Khoury, P. Z.; Han, K. S.; Deng, Z. D.; Xiao, J.; Zhang, J.-G.; Liu, J., Mechanism of Formation of Li<sub>7</sub>P<sub>3</sub>S<sub>11</sub> Solid Electrolytes through Liquid Phase Synthesis. *Chem. Mater.* **2018**, *30* (3), 990-997.
97. Kim, D. H.; Oh, D. Y.; Park, K. H.; Choi, Y. E.; Nam, Y. J.; Lee, H. A.; Lee, S. M.; Jung, Y. S., Infiltration of Solution-Processable Solid Electrolytes into Conventional Li-Ion-Battery Electrodes for All-Solid-State Li-Ion Batteries. *Nano Lett* **2017**, *17* (5), 3013-3020.
98. Calpa, M. R.-N., Nataly Carolina Miura, Akira Tadanaga, Kiyoharu, Instantaneous preparation of high lithium-ion conducting sulfide solid electrolyte Li<sub>7</sub>P<sub>3</sub>S<sub>11</sub> by a liquid phase process. *RSC Adv.* **2017**, *7* (73), 46499-46504.
99. Jung, S.-K.; Gwon, H.; Hong, J.; Park, K.-Y.; Seo, D.-H.; Kim, H.; Hyun, J.; Yang, W.; Kang, K., Understanding the Degradation Mechanisms of LiNi<sub>0.5</sub>Co<sub>0.2</sub>Mn<sub>0.3</sub>O<sub>2</sub> Cathode Material in Lithium Ion Batteries. *Adv. Energy Mater.* **2014**, *4* (1), 1300787.
100. Zhang, X.; Xue, Q.; Li, L.; Fan, E.; Wu, F.; Chen, R., Sustainable Recycling and Regeneration of Cathode Scraps from Industrial Production of Lithium-Ion Batteries. *ACS Sustainable Chem. Eng.* **2016**, *4* (12), 7041-7049.
101. Shi, Y.; Zhang, M.; Meng, Y. S.; Chen, Z., Ambient-Pressure Relithiation of Degraded Li<sub>x</sub>Ni<sub>0.5</sub>Co<sub>0.2</sub>Mn<sub>0.3</sub>O<sub>2</sub> (0 < x < 1) via Eutectic Solutions for Direct Regeneration of Lithium-Ion Battery Cathodes. *Adv. Energy Mater.* **2019**, *9* (20), 1900454.
102. Jung, Y. S.; Oh, D. Y.; Nam, Y. J.; Park, K. H., Issues and Challenges for Bulk-Type All-Solid-State Rechargeable Lithium Batteries using Sulfide Solid Electrolytes. *Israel Journal of Chemistry* **2015**, *55* (5), 472-485.
103. Kerman, K.; Luntz, A.; Viswanathan, V.; Chiang, Y.-M.; Chen, Z., Review—Practical Challenges Hindering the Development of Solid State Li Ion Batteries. *Journal of The Electrochemical Society* **2017**, *164* (7), A1731-A1744.
104. Chuang Yu, L. v. E., Swapna Ganapathy, Marnix Wagemaker\*, Synthesis, structure and electrochemical performance of the argyrodite Li<sub>6</sub>PS<sub>5</sub>Cl solid electrolyte for Li-ion solid state batteries. *Electrochimica Acta* **2016**, *215*, 93-99.
105. Jérémie Auvergniot, A. C., Jean-Bernard Ledeuil, Virginie Viallet, Vincent Seznec, and Rémi Dedryvère, Interface Stability of Argyrodite Li<sub>6</sub>PS<sub>5</sub>Cl toward LiCoO<sub>2</sub>, LiNi<sub>1/3</sub>Co<sub>1/3</sub>Mn<sub>1/3</sub>O<sub>2</sub>, and LiMn<sub>2</sub>O<sub>4</sub> in Bulk All-Solid-State Batteries. *Chemistry of Materials* **2017**, *29*, 3883-3890.

106. Wang, S.; Zhang, Y.; Zhang, X.; Liu, T.; Lin, Y. H.; Shen, Y.; Li, L.; Nan, C. W., High-Conductivity Argyrodite  $\text{Li}_6\text{PS}_5\text{Cl}$  Solid Electrolytes Prepared via Optimized Sintering Processes for All-Solid-State Lithium-Sulfur Batteries. *ACS applied materials & interfaces* **2018**.
107. Wenzel, S.; Weber, D. A.; Leichtweiss, T.; Busche, M. R.; Sann, J.; Janek, J., Interphase formation and degradation of charge transfer kinetics between a lithium metal anode and highly crystalline  $\text{Li}_7\text{P}_3\text{S}_{11}$  solid electrolyte. *Solid State Ionics* **2016**, *286*, 24-33.
108. Sebastian Wenzel, S. R., Thomas Leichtweiß, Dominik A. Weber, Joachim Sann, Wolfgang G. Zeier,\* and Jürgen Janek\*, Direct Observation of the Interfacial Instability of the Fast Ionic Conductor  $\text{Li}_{10}\text{GeP}_2\text{S}_{12}$  at the Lithium Metal Anode. *Chemistry of Materials* **2016**, *28*, 2400–2407.
109. Sakuda, A.; Hayashi, A.; Tatsumisago, M., Interfacial Observation between  $\text{LiCoO}_2$  Electrode and  $\text{Li}_2\text{S}$ – $\text{P}_2\text{S}_5$  Solid Electrolytes of All-Solid-State Lithium Secondary Batteries Using Transmission Electron Microscopy†. *Chemistry of Materials* **2010**, *22* (3), 949-956.
110. Hakari, T.; Deguchi, M.; Mitsuhashi, K.; Ohta, T.; Saito, K.; Orikasa, Y.; Uchimoto, Y.; Kowada, Y.; Hayashi, A.; Tatsumisago, M., Structural and Electronic-State Changes of a Sulfide Solid Electrolyte during the Li Deinsertion–Insertion Processes. *Chemistry of Materials* **2017**, *29* (11), 4768-4774.
111. Swamy, T.; Chen, X.; Chiang, Y.-M., Electrochemical Redox Behavior of Li Ion Conducting Sulfide Solid Electrolytes. *Chemistry of Materials* **2019**, *31* (3), 707-713.
112. Richards, W. D.; Miara, L. J.; Wang, Y.; Kim, J. C.; Ceder, G., Interface Stability in Solid-State Batteries. *Chemistry of Materials* **2015**, *28* (1), 266-273.
113. Zhang, W.; Leichtweiss, T.; Culver, S. P.; Koerver, R.; Das, D.; Weber, D. A.; Zeier, W. G.; Janek, J., The Detrimental Effects of Carbon Additives in  $\text{Li}_{10}\text{GeP}_2\text{S}_{12}$ -Based Solid-State Batteries. *ACS applied materials & interfaces* **2017**, *9* (41), 35888-35896.
114. Raimund Koerver, I. A. n., Thomas Leichtweiß, Christian Dietrich, Wenbo Zhang, Jan O. Binder, Pascal Hartmann, Wolfgang G. Zeier, and Jürgen Janek, Capacity Fade in Solid-State Batteries: Interphase Formation and Chemomechanical Processes in Nickel-Rich Layered Oxide Cathodes and Lithium Thiophosphate Solid Electrolytes. *Chemistry of Materials* **2017**, ( *29*, *13*, 5574-5582).
115. Jérémie Auvergniot a, b., Alice Cassel b, Dominique Foix a,c, Virgine Viallet b,c, Vincent Seznec b,c,\*, Rémi Dedryvère a,c,\*, Redox activity of argyrodite  $\text{Li}_6\text{PS}_5\text{Cl}$  electrolyte in all-solid-state Li-ion battery: An XPS study. *Solid State Ionics* *300* (2017) 78–85.
116. Suzuki, K.; Mashimo, N.; Ikeda, Y.; Yokoi, T.; Hirayama, M.; Kanno, R., High Cycle Capability of All-Solid-State Lithium–Sulfur Batteries Using Composite Electrodes by Liquid-Phase and Mechanical Mixing. *ACS Applied Energy Materials* **2018**, *1* (6), 2373-2377.
117. Yamada, T.; Ito, S.; Omoda, R.; Watanabe, T.; Aihara, Y.; Agostini, M.; Ulissi, U.; Hassoun, J.; Scrosati, B., All Solid-State Lithium–Sulfur Battery Using a Glass-Type  $\text{P}_2\text{S}_5$ – $\text{Li}_2\text{S}$  Electrolyte: Benefits on Anode Kinetics. *Journal of The Electrochemical Society* **2015**, *162* (4), A646-A651.

118. Kobayashi, T.; Imade, Y.; Shishihara, D.; Homma, K.; Nagao, M.; Watanabe, R.; Yokoi, T.; Yamada, A.; Kanno, R.; Tatsumi, T., All solid-state battery with sulfur electrode and thio-LISICON electrolyte. *Journal of Power Sources* **2008**, *182* (2), 621-625.
119. Kinoshita, S.; Okuda, K.; Machida, N.; Naito, M.; Sigematsu, T., All-solid-state lithium battery with sulfur/carbon composites as positive electrode materials. *Solid State Ionics* **2014**, *256*, 97-102.
120. Machida, N., Electrochemical properties of sulfur as cathode materials in a solid-state lithium battery with inorganic solid electrolytes. *Solid State Ionics* **2004**, *175* (1-4), 247-250.
121. Nagao, M.; Hayashi, A.; Tatsumisago, M., High-capacity Li<sub>2</sub>S–nanocarbon composite electrode for all-solid-state rechargeable lithium batteries. *Journal of Materials Chemistry* **2012**, *22* (19), 10015.
122. Lin, Z.; Liu, Z.; Fu, W.; Dudney, N. J.; Liang, C., Lithium polysulfidophosphates: a family of lithium-conducting sulfur-rich compounds for lithium-sulfur batteries. *Angewandte Chemie* **2013**, *52* (29), 7460-3.
123. Hayashi, A.; Ohtsubo, R.; Ohtomo, T.; Mizuno, F.; Tatsumisago, M., All-solid-state rechargeable lithium batteries with Li<sub>2</sub>S as a positive electrode material. *Journal of Power Sources* **2008**, *183* (1), 422-426.
124. Hayashi, A.; Ohtomo, T.; Mizuno, F.; Tadanaga, K.; Tatsumisago, M., Rechargeable lithium batteries, using sulfur-based cathode materials and Li<sub>2</sub>S–P<sub>2</sub>S<sub>5</sub> glass-ceramic electrolytes. *Electrochimica Acta* **2004**, *50* (2-3), 893-897.
125. Nagao, M.; Hayashi, A.; Tatsumisago, M., Sulfur–carbon composite electrode for all-solid-state Li/S battery with Li<sub>2</sub>S–P<sub>2</sub>S<sub>5</sub> solid electrolyte. *Electrochimica Acta* **2011**, *56* (17), 6055-6059.
126. Nagao, M.; Hayashi, A.; Tatsumisago, M., Fabrication of favorable interface between sulfide solid electrolyte and Li metal electrode for bulk-type solid-state Li/S battery. *Electrochemistry Communications* **2012**, *22*, 177-180.
127. Nagata, H.; Chikusa, Y., Activation of sulfur active material in an all-solid-state lithium–sulfur battery. *Journal of Power Sources* **2014**, *263*, 141-144.
128. Zhan Lin†, Z. L., Nancy J. Dudney†, and Chengdu Liang‡\*, Lithium Superionic Sulfide Cathode for All-Solid Lithium–Sulfur Batteries. *ACS Nano* **7** (3), pp 2829–2833.
129. Agostini, M.; Aihara, Y.; Yamada, T.; Scrosati, B.; Hassoun, J., A lithium–sulfur battery using a solid, glass-type P<sub>2</sub>S<sub>5</sub>–Li<sub>2</sub>S electrolyte. *Solid State Ionics* **2013**, *244*, 48-51.
130. Nagao, M.; Hayashi, A.; Tatsumisago, M.; Ichinose, T.; Ozaki, T.; Togawa, Y.; Mori, S., Li<sub>2</sub>S nanocomposites underlying high-capacity and cycling stability in all-solid-state lithium–sulfur batteries. *Journal of Power Sources* **2015**, *274*, 471-476.
131. Nagao, M.; Imade, Y.; Narisawa, H.; Kobayashi, T.; Watanabe, R.; Yokoi, T.; Tatsumi, T.; Kanno, R., All-solid-state Li–sulfur batteries with mesoporous electrode and thio-LISICON solid electrolyte. *Journal of Power Sources* **2013**, *222*, 237-242.

132. Choi, H. U.; Jin, J. S.; Park, J.-Y.; Lim, H.-T., Performance improvement of all-solid-state Li-S batteries with optimizing morphology and structure of sulfur composite electrode. *Journal of Alloys and Compounds* **2017**, *723*, 787-794.
133. Hayashi, A.; Ohtomo, T.; Mizuno, F.; Tadanaga, K.; Tatsumisago, M., All-solid-state Li/S batteries with highly conductive glass–ceramic electrolytes. *Electrochemistry Communications* **2003**, *5* (8), 701-705.
134. Hayashi, A.; Ohtsubo, R.; Tatsumisago, M., Electrochemical performance of all-solid-state lithium batteries with mechanochemically activated Li<sub>2</sub>S–Cu composite electrodes. *Solid State Ionics* **2008**, *179* (27-32), 1702-1705.
135. Nagata, H.; Chikusa, Y., A lithium sulfur battery with high power density. *Journal of Power Sources* **2014**, *264*, 206-210.
136. Trevey, J. E.; Gilsdorf, J. R.; Stoldt, C. R.; Lee, S. H.; Liu, P., Electrochemical Investigation of All-Solid-State Lithium Batteries with a High Capacity Sulfur-Based Electrode. *Journal of the Electrochemical Society* **2012**, *159* (7), A1019-A1022.
137. Zhang, Y.; Liu, T.; Zhang, Q.; Zhang, X.; Wang, S.; Wang, X.; Li, L.; Fan, L.-Z.; Nan, C.-W.; Shen, Y., High-performance all-solid-state lithium–sulfur batteries with sulfur/carbon nano-hybrids in a composite cathode. *Journal of Materials Chemistry A* **2018**, *6* (46), 23345-23356.
138. Wang, S.; Xu, X.; Zhang, X.; Xin, C.; Xu, B.; Li, L.; Lin, Y.-H.; Shen, Y.; Li, B.; Nan, C.-W., High-performance Li<sub>6</sub>PS<sub>5</sub>Cl-based all-solid-state lithium-ion batteries. *Journal of Materials Chemistry A* **2019**, *7* (31), 18612-18618.
139. Xu, R.; Yue, J.; Liu, S.; Tu, J.; Han, F.; Liu, P.; Wang, C., Cathode-Supported All-Solid-State Lithium–Sulfur Batteries with High Cell-Level Energy Density. *ACS Energy Letters* **2019**, 1073-1079.
140. Han, F.; Yue, J.; Fan, X.; Gao, T.; Luo, C.; Ma, Z.; Suo, L.; Wang, C., High-Performance All-Solid-State Lithium-Sulfur Battery Enabled by a Mixed-Conductive Li<sub>2</sub>S Nanocomposite. *Nano letters* **2016**, *16* (7), 4521-7.
141. Takeuchi, T.; Kageyama, H.; Nakanishi, K.; Tabuchi, M.; Sakaebe, H.; Ohta, T.; Senoh, H.; Sakai, T.; Tatsumi, K., All-Solid-State Lithium Secondary Battery with Li<sub>2</sub>S–C Composite Positive Electrode Prepared by Spark-Plasma-Sintering Process. *Journal of The Electrochemical Society* **2010**, *157* (11), A1196.
142. Hakari, T.; Nagao, M.; Hayashi, A.; Tatsumisago, M., All-solid-state lithium batteries with Li<sub>3</sub>PS<sub>4</sub> glass as active material. *Journal of Power Sources* **2015**, *293*, 721-725.
143. Hanghofer, I.; Gadermaier, B.; Wilkening, H. M. R., Fast Rotational Dynamics in Argyrodite-Type Li<sub>6</sub>PS<sub>5</sub>X (X: Cl, Br, I) as Seen by <sup>31</sup>P Nuclear Magnetic Relaxation—On Cation–Anion Coupled Transport in Thiophosphates. *Chemistry of Materials* **2019**, *31* (12), 4591-4597.
144. Deiseroth, H. J.; Kong, S. T.; Eckert, H.; Vannahme, J.; Reiner, C.; Zaiss, T.; Schlosser, M., Li<sub>6</sub>PS<sub>5</sub>X: a class of crystalline Li-rich solids with an unusually high Li<sup>+</sup> mobility. *Angew Chem Int Ed Engl* **2008**, *47* (4), 755-8.

145. Gobet, M.; Greenbaum, S.; Sahu, G.; Liang, C., Structural Evolution and Li Dynamics in Nanophase  $\text{Li}_3\text{PS}_4$  by Solid-State and Pulsed-Field Gradient NMR. *Chemistry of Materials* **2014**, 26 (11), 3558-3564.
146. Eckert, H.; Zhang, Z.; Kennedy, J. H., Structural Transformation of Non-Oxide Chalcogenide Glasses. The Short-Range Order of  $\text{Li}_2\text{S}-\text{P}_2\text{S}_5$  Glasses Studied by Quantitative  $^{31}\text{P}$  and  $^{6,7}\text{Li}$  High-Resolution Solid-State NMR. *Chemistry of Materials* **1990**, 2, 273-279.
147. Stöffler, H.; Zinkevich, T.; Yavuz, M.; Hansen, A.-L.; Knapp, M.; Bednarčík, J.; Randau, S.; Richter, F. H.; Janek, J.; Ehrenberg, H.; Indris, S., Amorphous versus Crystalline  $\text{Li}_3\text{PS}_4$ : Local Structural Changes during Synthesis and Li Ion Mobility. *The Journal of Physical Chemistry C* **2019**, 123 (16), 10280-10290.
148. Seino, Y.; Nakagawa, M.; Senga, M.; Higuchi, H.; Takada, K.; Sasaki, T., Analysis of the structure and degree of crystallisation of  $70\text{Li}_2\text{S}-30\text{P}_2\text{S}_5$  glass ceramic. *Journal of Materials Chemistry A* **2015**, 3 (6), 2756-2761.
149. Tan, D. H. S.; Wu, E. A.; Nguyen, H.; Chen, Z.; Marple, M. A. T.; Doux, J.-M.; Wang, X.; Yang, H.; Banerjee, A.; Meng, Y. S., Elucidating Reversible Electrochemical Redox of  $\text{Li}_6\text{PS}_5\text{Cl}$  Solid Electrolyte. *ACS Energy Lett.* **2019**, 2418-2427.
150. Huff, L. A.; Rapp, J. L.; Baughman, J. A.; Rinaldi, P. L.; Gewirth, A. A., Identification of lithium-sulfur battery discharge products through  $6\text{Li}$  and  $33\text{S}$  solid-state MAS and  $7\text{Li}$  solution NMR spectroscopy. *Surface Science* **2015**, 631, 295-300.
151. Lin, L.; Liang, F.; Zhang, K.; Mao, H.; Yang, J.; Qian, Y., Lithium phosphide/lithium chloride coating on lithium for advanced lithium metal anode. *Journal of Materials Chemistry A* **2018**, 6 (32), 15859-15867.
152. Nazri, G., Preparation, Structure and Ionic Conductivity of Lithium Phosphide. *Solid State Ionics* **1989**, 34, 97-102.
153. Deng, Z.; Zhang, Z.; Lai, Y.; Liu, J.; Li, J.; Liu, Y., Electrochemical Impedance Spectroscopy Study of a Lithium/Sulfur Battery: Modeling and Analysis of Capacity Fading. *Journal of The Electrochemical Society* **2013**, 160 (4) A553-A558
154. Park, K. H.; Bai, Q.; Kim, D. H.; Oh, D. Y.; Zhu, Y.; Mo, Y.; Jung, Y. S., Design Strategies, Practical Considerations, and New Solution Processes of Sulfide Solid Electrolytes for All-Solid-State Batteries. *Advanced Energy Materials* **2018**, 8 (18), 1800035.
155. Sakuda, A.; Hayashi, A.; Takigawa, Y.; Higashi, K.; Tatsumisago, M., Evaluation of elastic modulus of  $\text{Li}_2\text{S}-\text{P}_2\text{S}_5$  glassy solid electrolyte by ultrasonic sound velocity measurement and compression test. *Journal of the Ceramic Society of Japan* **2013**, 121 (1419), 946-949.
156. Sakuda, A.; Hayashi, A.; Tatsumisago, M., Sulfide solid electrolyte with favorable mechanical property for all-solid-state lithium battery. *Sci Rep* **2013**, 3, 2261.
157. Kato, Y.; Shiotani, S.; Morita, K.; Suzuki, K.; Hirayama, M.; Kanno, R., All-Solid-State Batteries with Thick Electrode Configurations. *J Phys Chem Lett* **2018**, 9 (3), 607-613.



158. Busche, M. R. W., Dominik A. Schneider, Yannik Dietrich, Christian Wenzel, Sebastian Leichtweiss, Thomas Schröder, Daniel Zhang, Wenbo Weigand, Harald; Walter, D. S., Stefan J. Houtarde, Diane Nazar, Linda F. Janek, Jürgen, In Situ Monitoring of Fast Li-Ion Conductor  $\text{Li}_7\text{P}_3\text{S}_{11}$  Crystallization Inside a Hot-Press Setup. *Chemistry of Materials* **2016**, 28 (17), 6152-6165.
159. Cheng, L.; Crumlin, E. J.; Chen, W.; Qiao, R.; Hou, H.; Franz Lux, S.; Zorba, V.; Russo, R.; Kostecki, R.; Liu, Z.; Persson, K.; Yang, W.; Cabana, J.; Richardson, T.; Chen, G.; Doeff, M., The origin of high electrolyte-electrode interfacial resistances in lithium cells containing garnet type solid electrolytes. *Physical chemistry chemical physics : PCCP* **2014**, 16 (34), 18294-300.
160. Sakuda, A.; Hayashi, A.; Hama, S.; Tatsumisago, M., Preparation of Highly Lithium-Ion Conductive 80Li<sub>2</sub>S·20P<sub>2</sub>S<sub>5</sub>Thin-Film Electrolytes Using Pulsed Laser Deposition. *Journal of the American Ceramic Society* **2010**, 93 (3), 765-768.
161. Zheng, J.; Tang, M.; Hu, Y. Y., Lithium Ion Pathway within  $\text{Li}_7\text{La}_3\text{Zr}_2\text{O}_{12}$  - Polyethylene Oxide Composite Electrolytes. *Angewandte Chemie* **2016**, 55 (40), 12538-42.
162. Guo, Q.; Han, Y.; Wang, H.; Xiong, S.; Li, Y.; Liu, S.; Xie, K., New Class of LAGP-Based Solid Polymer Composite Electrolyte for Efficient and Safe Solid-State Lithium Batteries. *ACS applied materials & interfaces* **2017**, 9 (48), 41837-41844.
163. Choi, J.-H.; Lee, C.-H.; Yu, J.-H.; Doh, C.-H.; Lee, S.-M., Enhancement of ionic conductivity of composite membranes for all-solid-state lithium rechargeable batteries incorporating tetragonal  $\text{Li}_7\text{La}_3\text{Zr}_2\text{O}_{12}$  into a polyethylene oxide matrix. *Journal of Power Sources* **2015**, 274, 458-463.
164. Zhang, X.; Liu, T.; Zhang, S.; Huang, X.; Xu, B.; Lin, Y.; Xu, B.; Li, L.; Nan, C. W.; Shen, Y., Synergistic Coupling between  $\text{Li}_{6.75}\text{La}_3\text{Zr}_{1.75}\text{Ta}_{0.25}\text{O}_{12}$  and Poly(vinylidene fluoride) Induces High Ionic Conductivity, Mechanical Strength, and Thermal Stability of Solid Composite Electrolytes. *Journal of the American Chemical Society* **2017**, 139 (39), 13779-13785.
165. Lee, K.; Kim, S.; Park, J.; Park, S. H.; Coskun, A.; Jung, D. S.; Cho, W.; Choi, J. W., Selection of Binder and Solvent for Solution-Processed All-Solid-State Battery. *Journal of The Electrochemical Society* **2017**, 164 (9), A2075-A2081.
166. Shao, C.; Liu, H.; Yu, Z.; Zheng, Z.; Sun, N.; Diao, C., Structure and ionic conductivity of cubic  $\text{Li}_7\text{La}_3\text{Zr}_2\text{O}_{12}$  solid electrolyte prepared by chemical co-precipitation method. *Solid State Ionics* **2016**, 287, 13-16.
167. Chu, I. H.; Nguyen, H.; Hy, S.; Lin, Y. C.; Wang, Z.; Xu, Z.; Deng, Z.; Meng, Y. S.; Ong, S. P., Insights into the Performance Limits of the  $\text{Li}_7\text{P}_3\text{S}_{11}$  Superionic Conductor: A Combined First-Principles and Experimental Study. *ACS applied materials & interfaces* **2016**, 8 (12), 7843-53.
168. M. J. Frisch, G. W. T., H. B. Schlegel, G. E. Scuseria,; M. A. Robb, J. R. C., G. Scalmani, V. Barone, B. Mennucci, G. A. Petersson, H. Nakatsuji, M. Caricato, X. Li, H. P. Hratchian, A. F. Izmaylov, J. Bloino, G. Zheng, J. L. Sonnenberg, M. Hada, M. Ehara, K. Toyota, R. Fukuda, J. Hasegawa, M. Ishida, T. Nakajima, Y. Honda, O. Kitao, H. Nakai, T. Vreven, J. A. Montgomery, Jr., J. E. Peralta, F. Ogliaro, M. Bearpark, J. J. Heyd, E. Brothers, K. N. Kudin, V. N. Staroverov, T. Keith, R. Kobayashi, J. Normand, K. Raghavachari, A. Rendell, J. C. Burant,

S. S. Iyengar, J. Tomasi, M. Cossi, N. Rega, J. M. Millam, M. Klene, J. E. Knox, J. B. Cross, V. Bakken, C. Adamo, J. Jaramillo, R. Gomperts, R. E. Stratmann, O. Yazyev, A. J. Austin, R. Cammi, C. Pomelli, J. W. Ochterski, R. L. Martin, K. Morokuma, V. G. Zakrzewski, G. A. Voth, P. Salvador, J. J. Dannenberg, S. Dapprich, A. D. Daniels, O. Farkas, J. B. Foresman, J. V. Ortiz, J. Cioslowski, and D. J. Fox, Gaussian, Inc., Wallingford CT, 2013. *Gaussian 09, Revision A.02*.

169. Becke, A. D., Density-functional thermochemistry. III. The role of exact exchange. *The Journal of Chemical Physics* **1993**, *98* (7), 5648-5652.

170. Lee, C.; Yang, W.; Parr, R. G., Development of the Colle-Salvetti correlation-energy formula into a functional of the electron density. *Physical Review B* **1988**, *37* (2), 785-789.

171. Marenich, A. V.; Cramer, C. J.; Truhlar, D. G., Universal Solvation Model Based on Solute Electron Density and on a Continuum Model of the Solvent Defined by the Bulk Dielectric Constant and Atomic Surface Tensions. *The Journal of Physical Chemistry B* **2009**, *113* (18), 6378-6396.

172. McCloskey, B. D., Attainable gravimetric and volumetric energy density of Li-S and li ion battery cells with solid separator-protected Li metal anodes. *The journal of physical chemistry letters* **2015**, *6* (22), 4581-8.

173. Agrawal, R. C., Pandey, G. P., Solid polymer electrolytes: materials designing and all-solid-state battery applications: an overview. *Journal of Physics D: Applied Physics* **2008**, *41* (22), 223001.

174. Yao, X.; Liu, D.; Wang, C.; Long, P.; Peng, G.; Hu, Y. S.; Li, H.; Chen, L.; Xu, X., High-Energy All-Solid-State Lithium Batteries with Ultralong Cycle Life. *Nano letters* **2016**, *16* (11), 7148-7154.

175. Jeschull, F.; Maibach, J.; Edström, K.; Brandell, D., On the Electrochemical Properties and Interphase Composition of Graphite: PVdF-HFP Electrodes in Dependence of Binder Content. *Journal of The Electrochemical Society* **2017**, *164* (7), A1765-A1772.

176. Peled, E.; Goor, M.; Schektman, I.; Mukra, T.; Shoval, Y.; Golodnitsky, D., The Effect of Binders on the Performance and Degradation of the Lithium/Sulfur Battery Assembled in the Discharged State. *Journal of The Electrochemical Society* **2016**, *164* (1), A5001-A5007.

177. Le, A. V.; Wang, M.; Noelle, D. J.; Shi, Y.; Shirley Meng, Y.; Wu, D.; Fan, J.; Qiao, Y., Using high-HFP-content cathode binder for mitigation of heat generation of lithium-ion battery. *International Journal of Energy Research* **2017**, *41* (14), 2430-2438.

178. Lacey, M. J.; Jeschull, F.; Edstrom, K.; Brandell, D., Why PEO as a binder or polymer coating increases capacity in the Li-S system. *Chemical communications* **2013**, *49* (76), 8531-3.

179. Yamane, H.; Shibata, M.; Shimane, Y.; Junke, T.; Seino, Y.; Adams, S.; Minami, K.; Hayashi, A.; Tatsumisago, M., Crystal structure of a superionic conductor, Li<sub>7</sub>P<sub>3</sub>S<sub>11</sub>. *Solid State Ionics* **2007**, *178* (15-18), 1163-1167.

180. Xu, R. C.; Xia, X. H.; Yao, Z. J.; Wang, X. L.; Gu, C. D.; Tu, J. P., Preparation of Li<sub>7</sub>P<sub>3</sub>S<sub>11</sub> glass-ceramic electrolyte by dissolution-evaporation method for all-solid-state lithium ion batteries. *Electrochimica Acta* **2016**, *219*, 235-240.

181. Lim, H.-D.; Lim, H.-K.; Xing, X.; Lee, B.-S.; Liu, H.; Coaty, C.; Kim, H.; Liu, P., Solid Electrolyte Layers by Solution Deposition. *Advanced Materials Interfaces* **2018**, *5* (8), 1701328.
182. Jin, Y.; Zhu, B.; Lu, Z.; Liu, N.; Zhu, J., Challenges and Recent Progress in the Development of Si Anodes for Lithium-Ion Battery. *Advanced Energy Materials* **2017**, *7* (23), 1700715.
183. Franco Gonzalez, A.; Yang, N.-H.; Liu, R.-S., Silicon Anode Design for Lithium-Ion Batteries: Progress and Perspectives. *The Journal of Physical Chemistry C* **2017**, *121* (50), 27775-27787.
184. Yang, Y.; Yuan, W.; Kang, W.; Ye, Y.; Pan, Q.; Zhang, X.; Ke, Y.; Wang, C.; Qiu, Z.; Tang, Y., A review on silicon nanowire-based anodes for next-generation high-performance lithium-ion batteries from a material-based perspective. *Sustainable Energy & Fuels* **2020**.
185. Wang, C.; Wu, H.; Chen, Z.; McDowell, M. T.; Cui, Y.; Bao, Z., Self-healing chemistry enables the stable operation of silicon microparticle anodes for high-energy lithium-ion batteries. *Nat Chem* **2013**, *5* (12), 1042-8.
186. Chen, J.; Fan, X.; Li, Q.; Yang, H.; Khoshi, M. R.; Xu, Y.; Hwang, S.; Chen, L.; Ji, X.; Yang, C.; He, H.; Wang, C.; Garfunkel, E.; Su, D.; Borodin, O.; Wang, C., Electrolyte design for LiF-rich solid–electrolyte interfaces to enable high-performance micro-sized alloy anodes for batteries. *Nature Energy* **2020**, *5* (5), 386-397.
187. Parikh, P.; Sina, M.; Banerjee, A.; Wang, X.; D'Souza, M. S.; Doux, J.-M.; Wu, E. A.; Trieu, O. Y.; Gong, Y.; Zhou, Q.; Snyder, K.; Meng, Y. S., Role of Polyacrylic Acid (PAA) Binder on the Solid Electrolyte Interphase in Silicon Anodes. *Chemistry of Materials* **2019**, *31* (7), 2535-2544.
188. Shobukawa, H.; Shin, J.; Alvarado, J.; Rustomji, C. S.; Meng, Y. S., Electrochemical reaction and surface chemistry for performance enhancement of a Si composite anode using a bis(fluorosulfonyl)imide-based ionic liquid. *Journal of Materials Chemistry A* **2016**, *4* (39), 15117-15125.
189. Li, L.; Zuo, Z.; Shang, H.; Wang, F.; Li, Y., In-situ constructing 3D graphdiyne as all-carbon binder for high-performance silicon anode. *Nano Energy* **2018**, *53*, 135-143.
190. Jung, C.-H.; Choi, J.; Kim, W.-S.; Hong, S.-H., A nanopore-embedded graphitic carbon shell on silicon anode for high performance lithium ion batteries. *Journal of Materials Chemistry A* **2018**, *6* (17), 8013-8020.
191. Hwang, C.; Lee, K.; Um, H.-D.; Lee, Y.; Seo, K.; Songz, H.-K., Conductive and Porous Silicon Nanowire Anodes for Lithium Ion Batteries. *Journal of The Electrochemical Society* **2017**, *164* (7), A1564-A1568
192. Kwon, H. J.; Hwang, J. Y.; Shin, H. J.; Jeong, M. G.; Chung, K. Y.; Sun, Y. K.; Jung, H. G., Nano/Microstructured Silicon-Carbon Hybrid Composite Particles Fabricated with Corn Starch Biowaste as Anode Materials for Li-Ion Batteries. *Nano Lett* **2020**, *20* (1), 625-635.

193. Ma, Q.; Xie, H.; Qu, J.; Zhao, Z.; Zhang, B.; Song, Q.; Xing, P.; Yin, H., Tailoring the Polymer-Derived Carbon Encapsulated Silicon Nanoparticles for High-Performance Lithium-Ion Battery Anodes. *ACS Applied Energy Materials* **2019**, 3 (1), 268-278.
194. Baasner, A.; Reuter, F.; Seidel, M.; Krause, A.; Pflug, E.; Härtel, P.; Dörfler, S.; Abendroth, T.; Althues, H.; Kaskel, S., The Role of Balancing Nanostructured Silicon Anodes and NMC Cathodes in Lithium-Ion Full-Cells with High Volumetric Energy Density. *Journal of The Electrochemical Society* **2020**, 167 (2), 020516.
195. Cangaz, S.; Hippauf, F.; Reuter, F. S.; Doerfler, S.; Abendroth, T.; Althues, H.; Kaskel, S., Enabling High-Energy Solid-State Batteries with Stable Anode Interphase by the Use of Columnar Silicon Anodes. *Advanced Energy Materials* **2020**, 10 (34), 2001320.
196. Huang, G.; Han, J.; Lu, Z.; Wei, D.; Kashani, H.; Watanabe, K.; Chen, M., Ultrastable Silicon Anode by Three-Dimensional Nanoarchitecture Design. *ACS Nano* **2020**, 14 (4), 4374-4382.
197. Wang, Y.; Satoh, M.; Arao, M.; Matsumoto, M.; Imai, H.; Nishihara, H., High-energy, Long-cycle-life Secondary Battery with Electrochemically Pre-doped Silicon Anode. *Sci Rep* **2020**, 10 (1), 3208.
198. An, W.; Gao, B.; Mei, S.; Xiang, B.; Fu, J.; Wang, L.; Zhang, Q.; Chu, P. K.; Huo, K., Scalable synthesis of ant-nest-like bulk porous silicon for high-performance lithium-ion battery anodes. *Nat Commun* **2019**, 10 (1), 1447.
199. Li, Y.; Yan, K.; Lee, H.-W.; Lu, Z.; Liu, N.; Cui, Y., Growth of conformal graphene cages on micrometre-sized silicon particles as stable battery anodes. *Nature Energy* **2016**, 1 (2).
200. Choi, S.; Kwon, T.-w.; Coskun, A.; Choi, J. W., Highly elastic binders integrating polyrotaxanes for silicon microparticle anodes in lithium ion batteries. *Science* **2017**, 357, 279–283.
201. Xu, Z.; Yang, J.; Zhang, T.; Nuli, Y.; Wang, J.; Hirano, S.-i., Silicon Microparticle Anodes with Self-Healing Multiple Network Binder. *Joule* **2018**, 2 (5), 950-961.
202. Gao, X.; Wang, F. G., Sam; Yuan, C., Micro Silicon–Graphene–Carbon Nanotube Anode for Full Cell Lithium-ion Battery. *Journal of Electrochemical Energy Conversion and Storage* **2019**, 16, 011009-1.
203. Sun, W.; Hu, R.; Liu, H.; Zeng, M.; Yang, L.; Wang, H.; Zhu, M., Embedding nano-silicon in graphene nanosheets by plasma assisted milling for high capacity anode materials in lithium ion batteries. *Journal of Power Sources* **2014**, 268, 610-618.
204. Ren, J.-G.; Wu, Q.-H.; Hong, G.; Zhang, W.-J.; Wu, H.; Amine, K.; Yang, J.; Lee, S.-T., Silicon-Graphene Composite Anodes for High-Energy Lithium Batteries. *Energy Technology* **2013**, 1 (1), 77-84.
205. Kim, J.-K.; Cho, G.-B.; Ryu, H.-S.; Ahn, H.-J.; Cho, K.-K.; Kim, K.-W.; Matic, A.; Jacobsson, P.; Ahn, J.-H., Electrochemical properties of a full cell of lithium iron phosphate cathode using thin amorphous silicon anode. *Solid State Ionics* **2014**, 268, 256-260.

206. Burkhardt, S.; Friedrich, M. S.; Eckhardt, J. K.; Wagner, A. C.; Bohn, N.; Binder, J. R.; Chen, L.; Elm, M. T.; Janek, J.; Klar, P. J., Charge Transport in Single NCM Cathode Active Material Particles for Lithium-Ion Batteries Studied under Well-Defined Contact Conditions. *ACS Energy Letters* **2019**, *4* (9), 2117-2123.
207. Qiu, X. Y.; Zhuang, Q. C.; Zhang, Q. Q.; Cao, R.; Ying, P. Z.; Qiang, Y. H.; Sun, S. G., Electrochemical and electronic properties of LiCoO<sub>2</sub> cathode investigated by galvanostatic cycling and EIS. *Phys Chem Chem Phys* **2012**, *14* (8), 2617-30.
208. Schwietert, T. K. A.; Violetta, A.; Wang, C. Y.; Chuang, Y.; Vasileiadis, A.; Klerk, N. J. J. d.; Hageman, J.; Hupfer, T.; Kerkamm, I.; Xu, Y.; Maas, E. v. d.; Kelder, E. M.; Ganapathy, S.; Wagemaker, M., Clarifying the relationship between redox activity and electrochemical stability in solid electrolytes. *Nature Materials* **2020**, *19*, 428-435.
209. Randau, S.; Weber, D. A.; Kötz, O.; Koerver, R.; Braun, P.; Weber, A.; Ivers-Tiffée, E.; Adermann, T.; Kulisch, J.; Zeier, W. G.; Richter, F. H.; Janek, J., Benchmarking the performance of all-solid-state lithium batteries. *Nature Energy* **2020**, *5* (3), 259-270.
210. Kasemchainan, J.; Zekoll, S.; Spencer Jolly, D.; Ning, Z.; Hartley, G. O.; Marrow, J.; Bruce, P. G., Critical stripping current leads to dendrite formation on plating in lithium anode solid electrolyte cells. *Nat Mater* **2019**, *18* (10), 1105-1111.
211. Sakabe, J.; Ohta, N.; Ohnishi, T.; Mitsuishi, K.; Takada, K., Porous amorphous silicon film anodes for high-capacity and stable all-solid-state lithium batteries. *Communications Chemistry* **2018**, *1* (1).
212. Hertzberg, B.; Benson, J.; Yushin, G., Ex-situ depth-sensing indentation measurements of electrochemically produced Si–Li alloy films. *Electrochemistry Communications* **2011**, *13* (8), 818-821.
213. Masias, A.; Felten, N.; Garcia-Mendez, R.; Wolfenstine, J.; Sakamoto, J., Elastic, plastic, and creep mechanical properties of lithium metal. *Journal of Materials Science* **2018**, *54* (3), 2585-2600.
214. Berla, L. A.; Lee, S. W.; Cui, Y.; Nix, W. D., Mechanical behavior of electrochemically lithiated silicon. *Journal of Power Sources* **2015**, *273*, 41-51.
215. Kim, H.; Chou, C.-Y.; Ekerdt, J. G.; Hwang, G. S., Structure and Properties of Li–Si Alloys: A First-Principles Study. *The Journal of Physical Chemistry C* **2011**, *115* (5), 2514-2521.
216. Doux, J. M.; Nguyen, H.; Tan, D. H. S.; Banerjee, A.; Wang, X.; Wu, E. A.; Jo, C.; Yang, H.; Meng, Y. S., Stack Pressure Considerations for Room-Temperature All-Solid-State Lithium Metal Batteries. *Advanced Energy Materials* **2019**, *10* (1), 1903253.
217. Lee, Y.-G.; Fujiki, S.; Jung, C.; Suzuki, N.; Yashiro, N.; Omoda, R.; Ko, D.-S.; Shiratsuchi, T.; Sugimoto, T.; Ryu, S.; Ku, J. H.; Watanabe, T.; Park, Y.; Aihara, Y.; Im, D.; Han, I. T., High-energy long-cycling all-solid-state lithium metal batteries enabled by silver–carbon composite anodes. *Nature Energy* **2020**, *5* (4), 299-308.
218. Wei, W.-Q.; Liu, B.-Q.; Gan, Y.-Q.; Ma, H.-J.; Cui, D.-W., Protecting lithium metal anode in all-solid-state batteries with a composite electrolyte. *Rare Metals* **2020**.

219. Ke, X.; Wang, Y.; Dai, L.; Yuan, C., Cell failures of all-solid-state lithium metal batteries with inorganic solid electrolytes: Lithium dendrites. *Energy Storage Materials* **2020**, *33*, 309-328.
220. Wang, B.; Ryu, J.; Choi, S.; Zhang, X.; Pribat, D.; Li, X.; Zhi, L.; Park, S.; Ruoff, R. S., Ultrafast-Charging Silicon-Based Coral-Like Network Anodes for Lithium-Ion Batteries with High Energy and Power Densities. *ACS Nano* **2019**, *13* (2), 2307-2315.
221. Pan, K.; Zou, F.; Canova, M.; Zhu, Y.; Kim, J.-H., Systematic electrochemical characterizations of Si and SiO anodes for high-capacity Li-Ion batteries. *Journal of Power Sources* **2019**, *413*, 20-28.
222. Banerjee, A.; Tang, H.; Wang, X.; Cheng, J. H.; Nguyen, H.; Zhang, M.; Tan, D. H. S.; Wynn, T. A.; Wu, E. A.; Doux, J. M.; Wu, T.; Ma, L.; Sterbinsky, G. E.; D'Souza, M. S.; Ong, S. P.; Meng, Y. S., Revealing Nanoscale Solid-Solid Interfacial Phenomena for Long-Life and High-Energy All-Solid-State Batteries. *ACS Appl Mater Interfaces* **2019**, *11* (46), 43138-43145.
223. Auvergniot, J.; Cassel, A.; Ledeuil, J.-B.; Viallet, V.; Seznec, V.; Dedryvère, R., Interface Stability of Argyrodite  $\text{Li}_6\text{PS}_5\text{Cl}$  toward  $\text{LiCoO}_2$ ,  $\text{LiNi}_{1/3}\text{Co}_{1/3}\text{Mn}_{1/3}\text{O}_2$ , and  $\text{LiMn}_2\text{O}_4$  in Bulk All-Solid-State Batteries. *Chemistry of Materials* **2017**, *29* (9), 3883-3890.
224. Diouf, B.; Podge, R., Potential of lithium-ion batteries in renewable energy. *Renewable Energy* **2015**, *76*, 375-380.
225. Qiao, Q.; Zhao, F.; Liu, Z.; Hao, H., Electric vehicle recycling in China: Economic and environmental benefits. *Resour., Conserv. Recycl.* **2019**, *140*, 45-53.
226. Harper, G.; Sommerville, R.; Kendrick, E.; Driscoll, L.; Slater, P.; Stolkin, R.; Walton, A.; Christensen, P.; Heidrich, O.; Lambert, S.; Abbott, A.; Ryder, K.; Gaines, L.; Anderson, P., Recycling lithium-ion batteries from electric vehicles. *Nature* **2019**, *575* (7781), 75-86.
227. Wang, X.; Gaustad, G.; Babbitt, C. W.; Richa, K., Economies of scale for future lithium-ion battery recycling infrastructure. *Resour., Conserv. Recycl.* **2014**, *83*, 53-62.
228. Yun, L.; Linh, D.; Shui, L.; Peng, X.; Garg, A.; Le, M. L. P.; Asghari, S.; Sandoval, J., Metallurgical and mechanical methods for recycling of lithium-ion battery pack for electric vehicles. *Resour., Conserv. Recycl.* **2018**, *136*, 198-208.
229. Lv, W.; Wang, Z.; Cao, H.; Sun, Y.; Zhang, Y.; Sun, Z., A Critical Review and Analysis on the Recycling of Spent Lithium-Ion Batteries. *ACS Sustainable Chem. Eng.* **2018**, *6* (2), 1504-1521.
230. Spangenberg, J. Novel Processing and Design Technologies Will Make Battery Recycling Profitable. Available at: [https://www.anl.gov/sites/www/files/2019-02/ReCell\\_FS.pdf](https://www.anl.gov/sites/www/files/2019-02/ReCell_FS.pdf) (accessed 21 Jun 2020).
231. Lee, Y.-G.; Fujiki, S.; Jung, C.; Suzuki, N.; Yashiro, N.; Omoda, R.; Ko, D.-S.; Shiratsuchi, T.; Sugimoto, T.; Ryu, S.; Ku, J. H.; Watanabe, T.; Park, Y.; Aihara, Y.; Im, D.; Han, I. T., High-energy long-cycling all-solid-state lithium metal batteries enabled by silver-carbon composite anodes. *Nat. Energy* **2020**.

232. Xu, R. C.; Xia, X. H.; Yao, Z. J.; Wang, X. L.; Gu, C. D.; Tu, J. P., Preparation of  $\text{Li}_7\text{P}_3\text{S}_{11}$  glass-ceramic electrolyte by dissolution-evaporation method for all-solid-state lithium ion batteries. *Electrochim. Acta* **2016**, *219*, 235-240.
233. Calpa, M.; Rosero-Navarro, N. C.; Miura, A.; Tadanaga, K., Instantaneous preparation of high lithium-ion conducting sulfide solid electrolyte  $\text{Li}_7\text{P}_3\text{S}_{11}$  by a liquid phase process. *RSC Adv.* **2017**, *7* (73), 46499-46504.
234. Han, F.; Westover, A. S.; Yue, J.; Fan, X.; Wang, F.; Chi, M.; Leonard, D. N.; Dudney, N. J.; Wang, H.; Wang, C., High electronic conductivity as the origin of lithium dendrite formation within solid electrolytes. *Nat. Energy* **2019**, *4* (3), 187-196.
235. Zhou, Y.; Doerrler, C.; Kasemchainan, J.; Bruce, P. G.; Pasta, M.; Hardwick, L., Observation of Interfacial Degradation of  $\text{Li}_6\text{PS}_5\text{Cl}$  against Lithium Metal and  $\text{LiCoO}_2$  via In Situ Electrochemical Raman Microscopy. *Batteries & Supercaps* **2020**.
236. Gao, B.; Jalem, R.; Ma, Y.; Tateyama, Y.,  $\text{Li}^+$  Transport Mechanism at the Heterogeneous Cathode/Solid Electrolyte Interface in an All-Solid-State Battery via the First-Principles Structure Prediction Scheme. *Chem. Mater.* **2019**, *32* (1), 85-96.
237. Wan, M.; Kang, S.; Wang, L.; Lee, H. W.; Zheng, G. W.; Cui, Y.; Sun, Y., Mechanical rolling formation of interpenetrated lithium metal/lithium tin alloy foil for ultrahigh-rate battery anode. *Nat Commun* **2020**, *11* (1), 829.
238. Nam, Y. J.; Oh, D. Y.; Jung, S. H.; Jung, Y. S., Toward practical all-solid-state lithium-ion batteries with high energy density and safety: Comparative study for electrodes fabricated by dry- and slurry-mixing processes. *Journal of Power Sources* **2018**, *375*, 93-101.
239. Lee, Y.-G.; Fujiki, S.; Jung, C.; Suzuki, N.; Yashiro, N.; Omoda, R.; Ko, D.-S.; Shiratsuchi, T.; Sugimoto, T.; Ryu, S.; Ku, J. H.; Watanabe, T.; Park, Y.; Aihara, Y.; Im, D.; Han, I. T., High-energy long-cycling all-solid-state lithium metal batteries enabled by silver-carbon composite anodes. *Nat. Energy* **2020**, *5* (4), 299-308.
240. EverBatt - Argonne's closed-loop battery life-cycle model. <https://www.anl.gov/egs/everbatt> (accessed 21 Jun 2020).
241. Shi, Y.; Chen, G.; Chen, Z., Effective regeneration of  $\text{LiCoO}_2$  from spent lithium-ion batteries: a direct approach towards high-performance active particles. *Green Chem.* **2018**, *20* (4), 851-862.
242. Liu, Y.; Mu, D.; Zheng, R.; Dai, C., Supercritical  $\text{CO}_2$  extraction of organic carbonate-based electrolytes of lithium-ion batteries. *RSC Adv.* **2014**, *4* (97), 54525-54531.
243. Grützke, M.; Mönnighoff, X.; Horsthemke, F.; Kraft, V.; Winter, M.; Nowak, S., Extraction of lithium-ion battery electrolytes with liquid and supercritical carbon dioxide and additional solvents. *RSC Adv.* **2015**, *5* (54), 43209-43217.
244. Golubkov, A. W.; Fuchs, D.; Wagner, J.; Wiltzsche, H.; Stangl, C.; Fauler, G.; Voitic, G.; Thaler, A.; Hacker, V., Thermal-runaway experiments on consumer Li-ion batteries with metal-oxide and olivin-type cathodes. *RSC Adv.* **2014**, *4* (7), 3633-3642.

245. Doux, J. M.; Nguyen, H.; Tan, D. H. S.; Banerjee, A.; Wang, X.; Wu, E. A.; Jo, C.; Yang, H.; Meng, Y. S., Stack Pressure Considerations for Room-Temperature All-Solid-State Lithium Metal Batteries. *Adv. Energy Mater.* **2019**, 1903253.
246. Banerjee, A.; Park, K. H.; Heo, J. W.; Nam, Y. J.; Moon, C. K.; Oh, S. M.; Hong, S. T.; Jung, Y. S., Na<sub>3</sub>SbS<sub>4</sub> : A Solution Processable Sodium Superionic Conductor for All-Solid-State Sodium-Ion Batteries. *Angew Chem Int Ed Engl* **2016**, 55 (33), 9634-8.
247. Li, X.; Liang, J.; Chen, N.; Luo, J.; Adair, K. R.; Wang, C.; Banis, M. N.; Sham, T. K.; Zhang, L.; Zhao, S.; Lu, S.; Huang, H.; Li, R.; Sun, X., Water-Mediated Synthesis of a Superionic Halide Solid Electrolyte. *Angew Chem Int Ed Engl* **2019**, 58 (46), 16427-16432.
248. Song, X.; Hu, T.; Liang, C.; Long, H. L.; Zhou, L.; Song, W.; You, L.; Wu, Z. S.; Liu, J. W., Direct regeneration of cathode materials from spent lithium iron phosphate batteries using a solid phase sintering method. *RSC Adv.* **2017**, 7 (8), 4783-4790.
249. Schlachter, F., No Moore's Law for batteries. *Proceedings of the National Academy of Sciences* **2013**, 110 (14), 5273-5273.